

**BIOSPHERE-ATMOSPHERE INTERACTION OVER THE CONGO BASIN AND
ITS INFLUENCE ON THE REGIONAL HYDROLOGICAL CYCLE**

A Dissertation
Presented to
The Academic Faculty by

By

Willis Otieno Shem

In Partial Fulfillment
Of the Requirements for the Degree
Doctor of Philosophy in the
School Of Earth and Atmospheric Sciences

Georgia Institute of Technology

August, 2006

BIOSPHERE-ATMOSPHERE INTERACTION OVER THE CONGO BASIN AND ITS
INFLUENCE ON THE REGIONAL HYDROLOGICAL CYCLE

Approved by:

Dr. Robert Dickinson
School of Earth and Atmospheric Sciences
Georgia Institute of Technology

Dr. Judith Curry
School of Earth and Atmospheric Sciences
Georgia Institute of Technology

Dr. Rodney Weber
School of Earth and atmospheric Sciences
Georgia Institute of Technology

Dr. Ellery Ingall
School of Earth and Atmospheric Sciences
Georgia Institute of Technology

Dr. Peter Webster
School of Civil and Environmental
Engineering
Georgia Institute of Technology

Date Approved: June 27, 2006

To my children Esther and Victor for their support on this journey

ACKNOWLEDGEMENTS

I would like to express sincere thanks to my advisor Professor Robert Dickinson for his insightful guidance, a listening ear and patience throughout my endeavor to get this job done. Much thanks also to my thesis reading committee members and my final doctoral exam committee members, comprising Professor's Judy Curry, Peter Webster, Ellery Ingall and Rodney Weber, for taking their time to serve in these positions. I thank Narcisse Ndri for helpful discussions along the way, Shaikh Muhammad for his assistance in exploiting the Linux working environment and Keith Oleson of NCAR for provision of NCEP data.

I would also like to appreciate my colleagues, Jiangfeng Wei for fruitful discussions on statistical analysis aspects, Yangping He for wide range discussions on Atmospheric Science, Haishan Chen for his comments on the community land model and the others for their good gestures. I thank the administrative team at the EAS, Judith Curry, Rita Bryan, Kathy Plummer, Susan Ryan and Laura Cederquist for their help whenever I needed it. Thank you Judy and Rita for all the kindness you showed to me. I would like to thank Janet MacGraw for her secretarial support.

Special thanks go to my dear friend Olive Awino for standing with me, Kendra Taylor for her prayers and Bryan Shaw for his moral support. Above all I thank God for the blessing of my two children who were patient and loving throughout the journey- deepest thanks to you Esther and Victor.

My graduate studies and funding for this dissertation were supported by the National Science Foundation

TABLE OF CONTENTS

Acknowledgements	iv
List of Tables	vii
List of Figures	viii
List of Nomenclature	xiii
Summary	xiv
Chapter 1 Introduction	1
1.1 Literature Review	2
1.2 The Congo Basin	6
1.3 Global perspectives on deforestation	6
Chapter 2 Model description and validation	9
2.1 Coupled Land/Atmosphere Model	9
2.1.1 Cam3	9
2.1.2 Clm3	11
2.1.3 Model data needs	14
2.2 Model Validation	15
2.2.1 Simulated versus observed precipitation	15
2.2.2 Simulated versus TRMM precipitation data	16
2.2.3 Simulation of the Inter-tropical Convergence Zone	21
2.2.4 Simulation of Soil Water	23
2.3 Temporal and Spatial Variability of Precipitation (EOF Analysis)	26
2.4 EOF Analysis of Channel Runoff	29
Chapter 3 Experiments	32
3.1 Design	32
3.1.1 Experiment 1 (High Deforestation)	33
3.1.2 Experiment 2 (Medium Deforestation)	34
3.1.3 Experiment 3 (Low Deforestation)	34
3.1.4 Experiment 4 (Reforestation)	35
3.2 Results and Discussions	42
3.2.1 Precipitation	42
3.2.2 Evapotranspiration	47
3.2.3 River Runoff	56
3.2.4 Temperature	57
3.2.5 Sensible heat flux	59
3.2.6 Latent heat flux	61

3.2.7 Soil Water Content	62
3.2.7.1 Correlation between Soil Moisture and Precipitation	66
3.3 Conclusions	72
Chapter 4 Simulation of the River Congo Runoff	74
4.1 Water balance for the Congo Basin	74
4.2 Runoff generation in CLM3	77
4.3 Congo River Runoff using NCEP Re-analysis data	82
4.4 Impact of top soil layers and deforestation on runoff simulation	85
4.5 Impact of saturated hydraulic conductivity ‘KD’ on Runoff simulation	88
4.6 Improved runoff simulation scheme	90
Chapter 5 Atmospheric Component of the Hydrological Cycle	92
5.1 Water vapor Transport	92
5.2 Zonal and Meridional Wind patterns over the Congo Basin	
5.3 Monsoon type of circulation over the Congo Basin	100
Chapter 6 Dynamical theory of Monsoonal Circulations in the tropics	105
6.1 Dynamical Theory	105
6.2 Factors that Influence Boundary Layer Entropy	110
6.3 Correlation of precipitation with meridional wind	112
6.4 Discussions	118
Chapter 7 Summary and Conclusions	119
7.1 Comments on effects of perturbing vegetation cover	119
7.2 Conclusions	121
Appendix A IGBP Land Cover Types	123
Appendix B Paired-Sample Students-‘t’ distribution	130
B.1 Tests for differences between control run and experimental cases.	130
References	137
Vita	141

LIST OF TABLES

Table 2.1 Congo Basin boundaries, soil texture profile and plant functional types	13
Table 3.1 I GBP Plant functional types in CLM3	33
Table 3.2 Dry and wet soil albedo	59
Table 3.3 Ranking of the key variables and precipitation from the various experiments.	73
Table 4.1 The values of exponential decay factor, f , of the saturated hydraulic Conductivity	79
Table A.1 IGBP Land Cover Types Definition	124
Table A.2 Plant function type optical properties	126
Table A.3 Plant functional type root distribution parameters	127
Table A.4 Plant functional type photosynthetic parameters	128
Table A.5 Water balance for the Congo Basin (1979-1983)	129
Table B.1 Monthly precipitation for Congo Basin, 1979-1983 (mm/day) Control case and High Deforestation (experiment 1)	132
Table B.2 Atmospheric input to land model	134
Table B.3 Land model output to atmospheric model	135
Table B.4 Model and empirical saturated hydraulic conductivity values	136

LIST OF FIGURES

Figure 1.1 Global Distribution of Original and Remaining Forest by the year 2000	8
Figure 2.1 Average monthly rainfall in the Congo Basin (model versus observation)	15
Figure 2.2 Net Solar Flux (surface), Clear Sky Net Solar Flux and Precipitation	17
Figure 2.3 MAM, (a) TRMM and (b) CAM3 (control) simulated rainfall- Congo Basin	18
Figure 2.4 JJA, (a) TRMM and (b) CAM3 (control) simulated rainfall- Congo Basin	19
Figure 2.5 Figure 2.5 OND, (a) TRMM and (b) CAM3 (control) simulated rainfall- Congo Basin	20
Figure 2.6 Zonal Averages - (a) MAM PPT and (b) JJA PPT. The box on the extreme right shows the range and zonal average values of precipitation	22
Figure 2.7 Zonal Averages -OND PPT. The box on the extreme right shows the range and zonal average values of precipitation.	23
Figure 2.8 CAM3/CLM3 simulated average soil water content at the surface layer (1980-1983)	24
Figure 2.9 Source: Soil map and soil climate map, USDA-NRCS, Soil Survey Division, World Soil Resources, Washington D.C.	25
Figure 2.10 EOF mode 1 spatial pattern of precipitation	26
Figure 2.11 Mode 1 - temporal pattern of precipitation	27
Figure 2.12 Mode 2 – Spatial pattern of precipitation	27
Figure 2.13 Mode 2 – temporal pattern of precipitation	28
Figure 2.14 Mode 1- temporal variability of runoff at the Kinshasa gauging station	30
Figure 2.15 Mode 2 –temporal variability of runoff at the Kinshasa gauging station	30

Figure 2.16 Reconstructed plot from the EOF analysis of the Congo River runoff	31
Figure 3.1 Land-cover types for the control simulation	36
Figure 3.2 Land-cover percentages for control simulation	37
Figure 3.3 Land-cover types for experiment 1 -high deforestation	38
Figure 3.4 Land-cover percentages for experiment 1 –high deforestation	39
Figure 3.5 Land-cover types for experiment 2 – medium deforestation	40
Figure 3.6 Land-cover percentages for experiment 2 – medium deforestation	41
Figure 3.7 The impact of different levels of deforestation on rainfall	42
Figure 3.8 Change in precipitation after high deforestation-MAM	44
Figure 3.9 Change in precipitation after high deforestation-JJA	44
Figure 3.10 Change in precipitation after high deforestation-OND	45
Figure 3.11 Change in precipitation after low deforestation –MAM	45
Figure 3.12 Change in precipitation after low deforestation-JJA	46
Figure 3.13 Change in precipitation after low deforestation –OND	46
Figure 3.14 The impact of different levels of deforestation on Evapotranspiration	47
Figure 3.15 Contrasting the impact of deforestation and reforestation on Evapotranspiration	48
Figure 3.16 Spatial distribution of control evapotranspiration- MAM	49
Figure 3.17 Spatial distribution of Experiment 1 evapotranspiration- MAM	49
Figure 3.18 Change in evapotranspiration after high deforestation (a) MAM and (b) JJA	50
Figure 3.19 Change in evapotranspiration after high deforestation –OND	51
Figure 3.20 Change in evapotranspiration after medium deforestation (a) MAM and (b) JJA	52
Figure 3.21 Change in evapotranspiration after medium deforestation –OND	53

Figure 3.22 Change in evapotranspiration after low deforestation (a) MAM and (b) JJA	54
Figure 3.23 Change in evapotranspiration after low deforestation-OND	55
Figure 3.24 Congo River runoff; Observed (IRI); Cam3/Clm3 simulation (control and experiment 1); Clm3 (offline) simulation using NCEP rainfall data and Nasa/Giss simulation	56
Figure 3.25 The impact of different levels of deforestation on temperature	57
Figure 3.26 The impact of different levels of deforestation on Sensible Heat Flux	60
Figure 3.27 The impact of different levels of deforestation on Latent Heat Flux	61
Figure 3.28 discretization of soil column in CLM: Z is the node depth for soil layer j (Wu and Dickinson 2004)	63
Figure 3.29 Volumetric soil water content for various soil layers after the control and high deforestation experiments.	64
Figure 3.30 Volumetric soil water content for various soil layers after the control, high and low deforestation experiments	65
Figure 3.31 Monthly time series of precipitation versus soil liquid in layer 1 - control case –after removing the seasonal cycle.	66
Figure 3.32 Monthly time series of precipitation versus soil liquid in layer 1 –high deforestation case–after removing the seasonal cycle.	67
Figure 3.33 Coherency and cross-wavelet between precipitation and soil liquid in layer 1 -control case	68
Figure 3.34 Coherency and cross-wavelet between precipitation and soil liquid in layer 1 –high deforestation case	69
Figure 3.35 Monthly time series of precipitation versus soil liquid in layer 7 – high deforestation case- after removal of the seasonal cycle	70
Figure 3.36 Coherency and cross-wavelet between precipitation and soil liquid in layer 7 –high deforestation case	71
Figure 4.1 Congo River- gauging station located at Kinshasa (4.3 ⁰ S, 15 ⁰ E)- from Global Runoff Data Center	75

Figure 4.2 River Congo Runoff (observed) at the entry to the Atlantic Ocean –obtained from the International Research Institute (IRI) database	76
Figure 4.3 Community Land Model Water Balance obtained from http://www.cgd.ucar.edu/tss/clm/rtm/waterbalance.gif	77
Figure 4.4 The difference between the actual hydraulic conductivity (Ks) profile based on soil texture and the exponential decay profile based on the TOPMODEL	78
Figure 4.5 Monthly hydrograph for the Amazon River, 1980; observed versus Simulated	83
Figure 4.6 Comparison of NCEP-reanalysis rainfall data, observed and CAM3 (model) simulated rainfall.	84
Figure 4.7 Congo River Runoff after various changes in soil hydraulic properties -1979	85
Figure 4.8 Congo River Runoff after various changes in soil hydraulic properties -1980	86
Figure 4.9 Congo River Runoff after various changes in soil hydraulic properties -1981	86
Figure 4.10 Congo River Runoff after various changes in soil hydraulic properties -1982	87
Figure 4.11 Congo River Runoff after various changes in soil hydraulic properties -1983	87
Figure 4.12 Impact of saturated hydraulic conductivity on Congo River runoff.	89
Figure 4.13 ‘KD’ sensitivity on a monthly basis	89
Figure 4.14 Improved runoff simulation based on the new scheme.	91
Figure 5.1 Evapotranspiration (from forest canopy) and total evaporation (forest canopy plus ground evaporation) shown as a percentage of total precipitation in both control and modified CAM2 simulations	93
Figure 5.2 Comparison of Precipitation and Canopy evapotranspiration	93

Figure 5.3 Zonal water vapor transport JJA (unit m/sg/kg)	94
Figure 5.4 Zonal water vapor transport OND ((unit m/sg/kg)	95
Figure 5.5 Meridional water vapor transport for (a) OND and (b) JJA	96
Figure 5.6 Rainfall in mm/day for the MAM period overlain with surface winds	101
Figure 5.7 Rainfall in mm/day for the JJA period overlain with surface winds	102
Figure 5.8 Rainfall in mm/day for the OND period overlain with surface winds	103
Figure 5.9 The hydrological cycle depicting the continuity provided by the terrestrial and atmospheric branches, (Peixoto and Oort Physics of Climate	104
Figure 6.1 Average wind velocity (m/s) for OND at the 20 ⁰ E meridional cross-section (a) zonal velocity for 1980, (b) meridional velocity for 1980, (c) zonal velocity for 1981 and (d) meridional velocity for 1981	109
Figure 6.2 Schematic of the proposed land –atmosphere –ocean interaction over West Africa (Eltahir and Gong-1996)	111
Figure 6.3 Monthly time series of precipitation versus meridional wind (200 mb-level) –high deforestation case–after removing the seasonal cycle.	112
Figure 6.4 Monthly time series of precipitation versus meridional wind (200 mb level) –control case–after removing the seasonal cycle.	113
Figure 6.5 Coherency and cross-wavelet between precipitation and meridional wind (200 mb level) –high deforestation case	114
Figure 6.6 Coherency and cross-wavelet between precipitation and meridional wind (200 mb level) soil liquid –high deforestation case	115
Figure 6.7 Relative strength of the amplitudes of precipitation and meridional wind wavelets at various frequencies (periods)- high deforestation	116
Figure 6.8 Relative strengths of the amplitudes of precipitation and meridional Wind wavelets at various frequencies (periods)- control case	117

LIST OF NOMENCLATURE

ABBREVIATION

CAM	Community Atmospheric Model
CCSM	Community Climate System of Models
CEA	Central Equatorial Africa
CLM	Community Land Model
ETR	Evapotranspiration
GCM	General Circulation Model
HDEF	High Deforestation
JJA	June July August
LAI	Leaf Area Index
LH	Latent Heat Flux
MAM	March April May
NCAR	National Center for Atmospheric Research
NCEP	National Centers for Environment Prediction
OND	October November December
PPT	Precipitation
SAI	Stem Area Index
SH	Sensible Heat Flux
SST	Sea Surface Temperature

SUMMARY

A comprehensive hydrological study of large watersheds in Africa e.g. the Congo basin and the Nile basin has not been vigorously pursued for various reasons. One of the major reasons is the lack of adequate modeling tools that would not be very demanding in terms of input data needs and yet inclusive enough to cover such wide extents (over 3 million square kilometers for the Congo basin).

Using a coupled run of the Community Atmospheric model (CAM3) and Community Land Model (CLM3) components of the Community Climate System of Models (CCSM), this study looks into the spatial and temporal variation of precipitation and river runoff in the Congo basin in the light of increasing trends in deforestation of the tropical forests. The effect of deforestation on precipitation and runoff is investigated by changing the land cover-type from the current configuration of broadleaf evergreen/deciduous, non-Artic grass and corn to a mostly grass type of vegetation. Discharge simulation for the river Congo is centered at the point of entrance to the Atlantic Ocean.

Although the CLM3 does not presently simulate the observed river runoff to within at least one standard deviation it gives an opportunity to iteratively improve on the land surface parameterization with a possibility of future accurate prediction of mean monthly river runoffs under varying climate scenarios and land use practices. When forced with the National Center for Environment and Prediction (NCEP) re-analysis data the CLM3 runoff simulation results are relatively more stable and much closer to the observed. An improved CLM3 when coupled to CAM3 or other Global Climate Models

is definitely a better tool for investigative studies on the regional hydrological cycle in comparison to the traditional methods.

There was a slight reduction in rainfall in the first experiment which mimicked a severe form of deforestation and a slight increase in rainfall following low level of deforestation. These changes in rainfall were however statistically insignificant when compared to the control simulation. There was notable heterogeneity in the spatial distribution of the changes in rainfall following deforestation.

CHAPTER 1

INTRODUCTION

The Central African Equatorial region (CEA) which is composed mainly of the Congo Basin, has not received adequate attention in the field of climate research despite its crucial position as the third largest deep convection center in the world after the West Pacific warm pool region and the Amazon Basin. It is still the least endowed in terms of climate data collection (equipment) and experimental (field) research. More often West Africa, especially the Sahel region, East Africa and to a lesser extent Southern Africa are the subject of most African climate variability studies covered in literature. The CEA region therefore represents a notable gap in our understanding of some aspects of the tropical climate system, e.g. the influence of tropical land cover type on some climate parameters like rainfall and river runoff.

This situation has led to large data gaps in a key climatic zone which make it difficult to address the global climatic situation in a more integrated manner. The recent trend, i.e. the use of models and modern data collection facilities e.g. satellites is a most welcome event for bridging the data gaps in the region.

Tropospheric heating resulting from deep convection within the Congo basin is one of the major driving forces of the general circulation especially over the tropics. In the last part of this study an attempt has been made to look at the relationship between the upper level (above 600 mb) wind patterns and the seasonal rainfall variability.

Paleoclimatological and sedimentary data in the mid-Holocene period indicate that the Sahara/Sahel region might have been much wetter and greener than is currently the

case. Simulations from coupled biosphere–atmosphere models, e.g. Bureau of Meteorology's atmosphere model (zonal BAM), show that changes in the land-cover type, possibly due to anthropogenic activities, could be largely responsible for the southward spread of the desert by about 5° in latitude from its early- Holocene boundaries (Irizarry-Ortiz et al, 2003).

Charney's hypothesis on the dynamics of deserts and droughts in the Sahel region (Charney, 1975) seems to lend credence to the southward spread of the Sahara due to anthropogenic activities. However, the Congo basin's resilience in precipitation and water yield goes against the grain in this case. Chapter 6 of this study suggests that the large scale circulation patterns as indicated by the upper level wind convergence and divergence might offer the negative feedback that steadies the rainfall regime over the basin.

1.1 Literature Review

The continuing work on the biosphere-Atmosphere interaction can be traced back to the proposal by Charney (1975), whose work on the drought mechanisms of the Sahel focused on the role of land use changes in forcing the atmosphere. Since then a number of studies have been undertaken using general circulation models (GCM) with the purpose of understanding the environmental effects and climate alterations that might be associated with the continuous removal of tropical rainforests (Henderson-Sellers and Gornitz, 1984; Dickinson and Henderson-Sellers, 1986; Lean and Warrilow, 1989; Shukla et al., 1990; Nobre et al., 1991)

The earlier experiments used models with much lower spatial resolutions and were not able to represent the mosaic nature of the plant types on a single grid. Henderson-Sellers and Gornitz (1984) performed the first deforestation experiment using the Goddard Institute for Space Studies finite difference model which had a resolution of 8° latitude by 10° longitude. To mimic the change in vegetation from tropical forest to grassland, the albedo value was increased while the roughness length and soil moisture-holding capacity was reduced. A total area of 4.94×10^6 square kilometers was deforested from the Amazonian Basin. A 10-year simulation was done and the last 5 years were then compared to the last 5 years of a 20-year control run. Their results indicated no change in surface temperature, decreased rainfall (rainfall decreased by 0.6mm per day), decreased evaporation (0.4-0.5 mm per day), decreased cloud cover (5-15 %), increased planetary albedo (1-1.5%) and decreased soil moisture availability. They did not observe any significant regional or global scale effects.

Dickinson and Henderson-Sellers (1988) modeled tropical deforestation (Amazonian Basin) by changing several parameters in the Biosphere-Atmosphere Transfer Scheme (BATS) to represent the change from tropical moist forest to impoverished grassland. They used the National Centre for Atmospheric Research Community Climate Model (NCAR CCMOB) at a resolution of 4.5° by 7.5°. They noted that seasonal pattern of precipitation was satisfactorily simulated but that the modeled precipitation was greater than observed in some parts of the study area. Their observations included a rainfall response that was noisy with no systematic regional change, an increase in surface and soil temperature (approximately 2K), decreased evaporation except in September and decreased canopy interception except in August.

Shukla et al's (1990) simulation was conducted with relatively high resolution in comparison to others in the past as summarized in the report by Nobre et al (1991). Deforestation was modeled by changing a range of physical parameters in the SiB land-surface scheme (Sellers et al., 1986). They used the NMC GCM (spectral) model at R40 (1.8° X 2.8°) resolution (Sela, 1980; Kinter et al., 1988; Sato et al., 1989). The SST fields for the model were fixed at December values and cloudiness was prescribed from seasonal means.

The last few years have seen more improvements in model resolutions and in the mosaic representation of the various plant functional types. There have also been significant improvements in the land-surface schemes used in the coupled global circulation models. The advances on the land surface schemes tailor-made for use in General Circulation Models (GCMs) are mostly expansions on Dickinson's et al (1984) BATS and Sellers's et al (1986) Simple Biosphere Scheme (SiB).

Recent work on the influence of land cover change on the African climate have used more 'realistic' scenarios for simulating the impacts by taking advantage of the improved computational capacity (Maynard and Royer, 2004). Where as the past studies needed 'complete' deforestation to be able to detect the model response to the land use change, current experiments can investigate less drastic perturbations like fractional decline of specific plant functional types. A couple of experiments have attempted to investigate the relationship between the surface energy budgets and both the atmospheric circulation and the hydrological cycle. Numaguti (1993) highlighted the role of evapotranspiration in the Hadley circulation dynamics by indicating that a small fractional change in evapotranspiration, as often occurs in deforestation experiments,

could course large changes in the energy supply thereby resulting in significant modification to the meridional structure of the Hadley circulation. The possibility of large scale climate disturbances originating from the effects of tropical deforestation have also been investigated by Zhang et al (1996) , Sudd et al (1996) and Zeng et al (1996)

The role of soil moisture content in regulating the impact of tropical deforestation has also been receiving some attention. Osborne et al (2003) have shown that the introduction of freely draining soils in the tropics via the hydraulic parameters reduces significantly the climate sensitivity to vegetation and by implication to land use change. Eltahir and Gong's (1996) and Irizary-Ortiz et al (2002) have looked at the influence of deforestation on the West African Monsoon and have pointed out the positive correlation between the meridional gradient of boundary layer entropy and the zonal wind at upper levels. The impact of tropical deforestation on hydroclimatic variables (e.g. precipitation, soil moisture, evaporation) in the extra-tropical regions have been shown in some studies to have very little statistical significance (Findell et al 2005).

Most of the studies mentioned above have focused on various elements of the climate parameters in diverse places within the tropics. This study focuses on the climatic parameters over the Congo basin and offers a unique view of the integrated influence of deforestation on the Central African Equatorial region. It looks at the spatial and temporal variation of precipitation, evapotranspiration and runoff, i.e. the land surface components of the hydrological cycle, and the divergence/convergence of the upper levels winds over the basin in response to various levels of deforestation. The idea is to be able to identify the existence of a compensatory influx of water vapor at the upper levels following the reduction in local upward flux of moisture associated with deforestation. The study has

looked into the change in circulation pattern that might be inhibiting a positive feedback between deforestation and precipitation or the intensity of the hydrological cycle.

1.2 The Congo Basin

The Congo basin is located in the central and western region of the African Continent roughly within latitudes 10°E- 30° E and longitudes 10° S-5° N. The Congo basin forest has shown much resilience in size and water yield despite the clearly increasing trends of deforestation in the recent past. The basin is 3.4 million square kilometers in size and its water yield per unit river length is second only to the Amazonian basin, giving it a prominent position in the water stressed continent of Africa. The changing demography and socio economic issues in the region have a direct impact on the land use practices with accompanying climatic feedbacks. Deforestation is currently one of the most visible anthropogenic influences in the Congo basin.

1.3 Global perspectives on deforestation

For the period 1980-1990 the tropical forests of the world are estimated to have been disappearing at the rate of 17 million ha annually (Lanly et al., 1991). This figure is known to have increased to 20 million ha annually in the early 1990s (Lal, 1995). While the accuracy of these figures may be open to debate, there has been a deluge of publications giving specific and vivid descriptions of environmental changes wrought by deforestation (Proctor, 1989). These publications have lead many to automatically associate tropical deforestation with negative impacts like lower rainfall, lower water

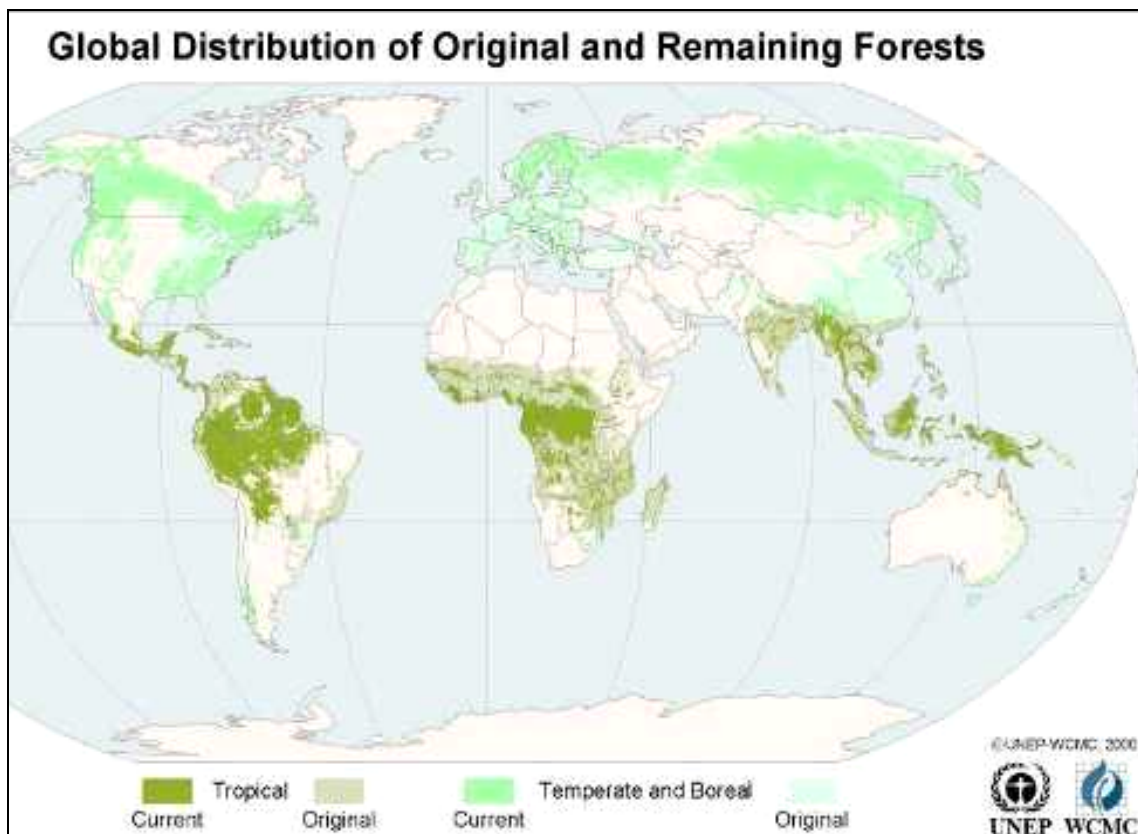
yields from springs and streams, major floods, extreme sedimentation and hence the choking of reservoirs and irrigation canals, etc.

Deforestation is defined as the clearing of large spaces in the natural forest, mostly through anthropogenic activities, as the expanding human populations seeks to exploit the forested areas for its own comfort and 'survival'. Despite efforts by the international community to stem deforestation, it has to a large extent persisted, especially in areas like the African tropical forests where the quest for modern living styles are quickly encroaching together with the increase in population (figure 1.1). The reasons for deforestation range from the need for more land for agriculture, livestock and habitat to commercialization of forest for the manufacture of paper and other wood products. In Central Africa many landless people have been moving into the once forested areas and are quickly converting them into cultivated plots using simple slash and burn methods to create more space. The use of fuel-wood as the main source of energy is another major reason that leads to tropical deforestation.

These forests are valuable sources of biological diversity. Tropical forests provide irreplaceable habitat for as much as 80% of the world's species of plants and animals most of which remain to be discovered and described scientifically. More than one quarter of the prescription drugs in the United States have their origin in the tropical plants (Vig and Kraft, 2003). Forests also act to stabilize soils and to regulate local climates, watersheds and river systems. The destruction of tropical forests is also a contributor to the increasing levels of carbon dioxide in the atmosphere (the greenhouse effect), a global concern due to its impact on global temperatures. Plants, through the

process of photosynthesis, remove carbon dioxide from the atmosphere and release oxygen.

Forests can be cleared by occasional fires, cyclones, selective logging etc. Some of these disturbances are of intermediate intensity and the forest tends to recover after a relatively short while. This study is looking into the scenario where the forest is converted into grassland due to persistent logging for cultivation purposes or for settlement. This is therefore a long- term change where recovery might not happen for several decades.



Document URL: <http://www.unep-wcmc.org/forest/original.htm>

Figure 1.1 Global Distribution of Original and Remaining Forest by the year 2000.

CHAPTER 2

MODEL DESCRIPTION AND VALIDATION

2.1 Coupled Land/Atmosphere Model

The Community Atmospheric Model (CAM) and the Community Land Model (CLM) are the Atmospheric and Land-surface modules, respectively, of the well documented, modular and versatile general circulation system of models known as the Community Climate System of Models (CCSM). The CAM3 model is the latest in a series of atmospheric components (originally known as CCM) of the fully coupled CCSM. This series was renamed CAM to reflect the role (atmospheric component) it plays in the fully coupled run of the CCSM. Similarly CLM3 is the latest in the land component series of the CCSM.

2.1.1 CAM3

CAM3 is a comprehensive, three-dimensional global atmospheric model that has been made suitable for coupling to land, ocean and sea-ice component models. The version of this model used had a T42 spectral resolution (approximately 2.8 x 2.8 degree transform grid) with 26 vertical levels in hybrid (sigma-pressure) coordinates and a lid at 2.917 mb. Although it is based on the semi-implicit Eulerian spectral transform dynamical core the code includes the option to use the semi-Lagrange dynamics.

Land surface fluxes of momentum, sensible heat, and latent heat are calculated from Monin-Obukhov similarity theory applied to the surface (i.e. constant flux) layer.

The process of deep convection is treated with a parameterization scheme developed by Zhang and McFarlane [1995]. The scheme is based on a plume ensemble approach where it is assumed that an ensemble of convective scale updrafts (and the associated saturated downdrafts) may exist whenever the atmosphere is conditionally unstable in the lower troposphere.

The CAM 3.0 employs a Sundqvist [1988] style evaporation of the convective precipitation as it makes its way to the surface. This scheme relates the rate at which raindrops evaporate to the local large-scale subsaturation and the rate at which convective rainwater is made available to the subsaturated model layer

Cloud amount (or cloud fraction), and the associated optical properties, are evaluated via a diagnostic method in CAM 3.0. The diagnosis of cloud fraction is a generalization of the scheme introduced by Slingo [1987]. Cloud fraction depends on relative humidity, atmospheric stability and convective mass fluxes. The three types of clouds diagnosed by the scheme are low-level marine stratus (Cst), convective cloud (Ccir), and layered cloud (Cc). Layered clouds form when the relative humidity exceeds a threshold value which varies according to pressure.

The shortwave parameterization (insolation) is computed using the method of Berger [1978], while the longwave radiative transfer is based on an absorptivity/emissivity formulation [Ramanathan and Downey, 1986]

The parameterization of non-convective cloud processes in CAM 3.0 is described in Rasch and Kristj'ansson [1998] and Zhang et al. [2003]. The original formulation is introduced in Rasch and Kristj'ansson [1998]. Revisions to the parameterization to deal

more realistically with the treatment of the condensation and evaporation under forcing by large scale processes and changing cloud fraction are described in Zhang et al. [2003].

There is a new treatment of aerosols in CAM 3.0 replacing the uniform background boundary-layer aerosol used in previous versions of CAM and CCM.

The surface exchange of heat, moisture and momentum between the atmosphere and land, ocean or ice surfaces are treated with a bulk exchange formulation.

2.1.2 CLM3

In the initial stages of their creation GCMs treated land as a simple reservoir of water and thermal energy. The representation of parameters was spatially very sketchy and there was very little comparison to observations. Since the 1980's however, there has been a tremendous growth in the knowledge base of the land surface processes leading to more specificity in areal representation of processes and the inclusion of vegetation, soil texture and even soil color data.

The data used in these early stages were inferred from a wide variety of heterogeneous sources e.g. geographical data were obtained from national atlases. Much improvement on land cover data collection has been achieved by the use of satellites over the past two decades. Scientists can now reformulate the models to factor in spatial heterogeneities and other details related to canopy characteristics.

The CLM is designed for coupling to atmospheric numerical models. It provides surface albedos (direct beam and diffuse for visible and near-infrared wavebands), upward longwave radiation, sensible heat flux, latent heat flux, water vapor flux, and zonal and meridional surface stresses required by atmospheric models. These are

regulated in part by many ecological and hydrological processes, and the model simulates processes such as leaf phenology, stomata physiology, and the hydrologic cycle. The model accounts for ecological differences among vegetation types, hydraulic and thermal differences among soil types (Table 2.1), and allows for multiple land cover types within a grid cell.

It is intended to capture the biogeophysical and biogeochemical differences between broad categories of plants in terms of their functional characteristics. Up to 4 of 15 possible plant functional types (PFTs) that differ in physiology and structure may coexist on a single column. All fluxes to and from the surface are defined at the PFT level, as are the vegetation state variables (e.g. vegetation temperature and canopy water storage).

A river transport model routes runoff downstream to oceans. Because the model is designed for coupling to climate and numerical weather prediction models, there is a compromise between computational efficiency and the complexity with which land surface processes are parameterized. The model is not meant to be a detailed description of hydrometeorology and terrestrial ecosystems, but rather a simplified treatment of surface processes that reproduces at minimal computational cost the essential characteristics of land-atmosphere interactions important for climate simulations (NCAR Technical Note, 2004).

Table 2.1 Congo Basin boundaries, soil texture profile and plant functional types

Congo Basin																	
Boundaries			Soil														
East	30		Layer	Sand %	Clay %												
West	10		1	48.9	29.9												
North	5		2	48.7	30.4												
South	-10		3	47.6	31.3												
			4	47.1	32.2												
			5	46.0	34.0												
			6	45.2	35.4												
			7	44.1	36.8												
			8	44.1	36.8												
			9	44.6	35.8												
			10	44.3	39.0												
Size of Basin			Color														
Total Grids	42		5.62														
Land Grids	39.18																
Ocean Grids	2.82																
Land mask Grids	41																
Wetland Grids	0.84																
Lake Grids	0.12																
Area Coverage		04 Broadleaf Evergreen Tropical			06 Broadleaf Deciduous Tropical			13 C3 Non-Artic Grass		14 C4 Grass		15 Corn		Non-Vegetation		Composite	
		44.51%			14.37%			15.39%		24.44%		1.17%		0.12%		100%	
Month	LAI	SAI	SAI	LAI	SAI	LAI	SAI	LAI	SAI	LAI	SAI	LAI	SAI	LAI	SAI	LAI	
Jan	3.44	6	0.5	2.18	0.34	2.28	0.65	2.36	0.63	2.35	0	0	0	2.80	3.94		
Feb	3.55	6	0.5	2.17	0.56	2.32	1.71	2.40	1.62	2.31	0	0	0	2.86	3.95		
Mar	3.62	6	0.5	2.07	0.63	2.19	0.86	2.29	0.83	2.34	0	0	0	2.83	3.89		
Apr	3.63	6	0.5	1.84	0.81	1.93	0.37	2.02	0.37	2.15	0	0	0	2.70	3.75		
May	3.59	6	0.5	1.50	0.68	1.60	0.37	1.66	0.37	1.57	0	0	0	2.48	3.56		
Jun	3.42	6	0.5	1.04	0.24	1.21	0.40	1.23	0.40	0.91	0	0	0	2.17	3.32		
Jul	3.10	6	0.5	0.90	0.36	1.05	0.45	1.05	0.47	0.44	0	0	0	1.93	3.22		
Aug	2.97	6	0.5	1.00	0.44	1.05	0.89	1.09	0.98	0.29	0	0	0	1.90	3.25		
Sep	3.07	6	0.5	1.34	0.57	1.33	0.54	1.48	0.57	0.32	0	0	0	2.13	3.43		
Oct	3.20	6	0.5	1.77	0.59	1.65	0.33	1.82	0.33	0.60	0	0	0	2.38	3.63		
Nov	3.25	6	0.5	2.06	0.52	1.87	0.33	2.02	0.33	1.36	0	0	0	2.54	3.76		
Dec	3.34	6	0.5	2.13	0.26	2.12	0.40	2.23	0.40	2.14	0	0	0	2.69	3.87		
Average	3.35	6	0.50	1.67	0.50	1.72	0.61	1.80	0.61	1.40	0	0	0	2.45	3.63		

2.1.3 Model Data Needs

The input dataset needed for CAM3 include the initial state data, ozone boundary data and water vapor absorptivity and emissivity data. The initial dataset consists of the prognostic variables like zonal wind component, meridional wind component, temperature, specific humidity, surface pressure and cloud mass mixing ratio among others. A climatological dataset of sea surface temperatures (SST) containing 12 monthly time samples is read in by the ocean data model.

The major input in the land component (CLM3) is the dataset providing plant functional type and physiological constants. A default land surface dataset based on the International Geosphere-Biosphere Program (IGPB) classification is provided with the model. Modification of this dataset for the Congo basin is the major focus in this experiment. Other indices that define the land surface characteristics are the soil texture and soil color.

The coupled CAM3/CLM3 model run involves data input/output exchange between the two models. The atmospheric model input to the land model is shown in table B1.2 while the converse is shown in table B1.3. The grid-average atmospheric forcing is used to force all subgrid units within a grid cell. The surface variables and fluxes required by the atmosphere are obtained by averaging the subgrid quantities weighted by their fractional areas.

2.2 Model Validation

2.2.1 Simulated versus observed Precipitation

The first step in this experiment is to find out how well the CAM model captures the temporal and spatial distribution of rainfall in the basin. To this end monthly mean (observed) rainfall data in the Congo basin for 15 stations was plotted against the CAM3 simulated rainfall. The observed data was collected by Sharon Nicholson (NCAR Data Support Section-1982-Monthly African rainfall data).

The model overestimates the mean monthly precipitation for the 20 year period 1979-1988 when compared to the mean of observations from the 15 stations within the basin. The model however reproduces the seasonal variations of precipitation and more noticeably the bi-modal pattern of the equatorial region precipitation (figure 2.1).

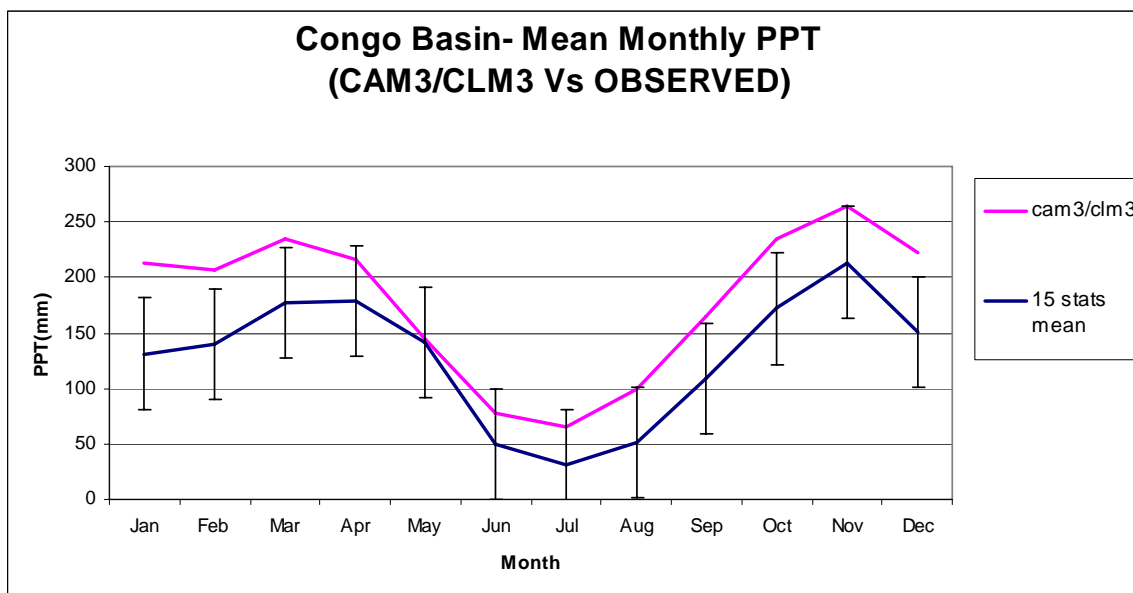


Figure 2.1 Average monthly rainfall in the Congo Basin (model versus observation)

2.2.2 Simulated versus TRMM Precipitation data

There is also considerable variance in the spatial distribution of the mean monthly rainfall between the simulated (CAM3) results and the observed rainfall data obtained from the Tropical Rainfall Monitoring Mission (TRMM), figures 2.3, figure 2.4 and figure 2.5. These figures show the spatial distribution of seasonal averages in MAM, JJA and OND precipitation. The MAM rainfall from the TRMM is heaviest (above 6 mm/day) in the Southwestern corner of the basin while the same level of rainfall from the CAM3- simulated (control) MAM rainfall is a well mixed patch a cross the basin. The drier period of the year, JJA, shows better agreement in values of rainfall between TRMM and CAM3 with the TRMM data having a slightly wider coverage for the above 6 mm/day rainfall. The OND rainy season depicts some discrepancy between the TRMM and CAM3 simulation. The CAM3 simulation has a wider spread of above 6 mm/day rainfall while the TRMM restricts it to the Northwest portion of the basin.

The best results of the CAM3 simulation in comparison to the observed TRMM data is for the drier JJA period. The wetter MAM and OND months are not as good. A likely contribution to this fact is the uncertainty associated with convective cloud parameterization in the CAM3. This theory is also supported by a simple analysis of the correlations among the Net Solar Flux at the surface, Clear Sky Net Solar Flux at the surface and total precipitation in mm/day, figure 2.2

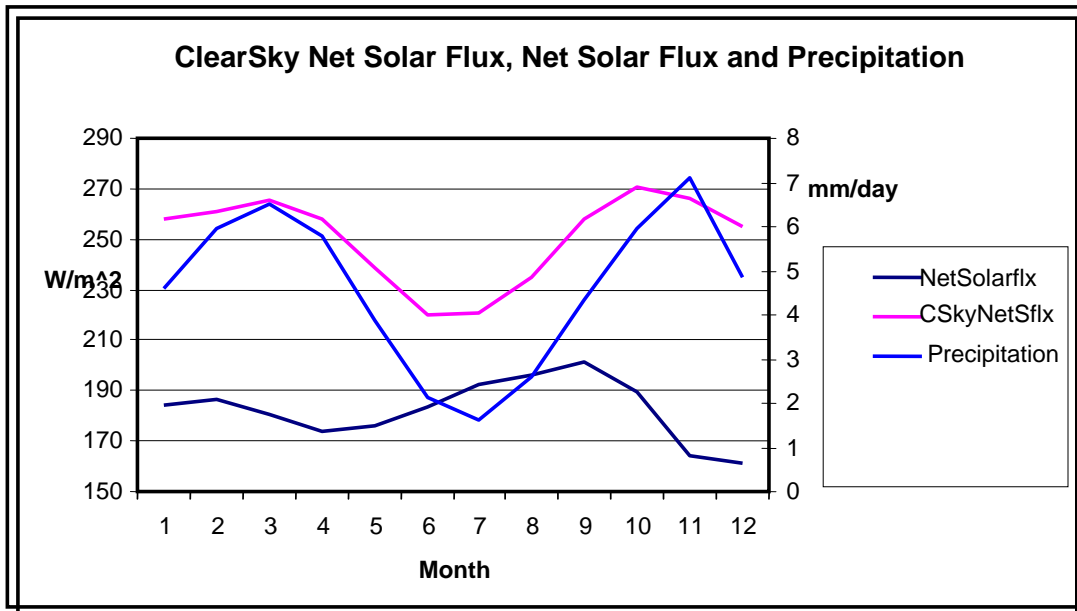
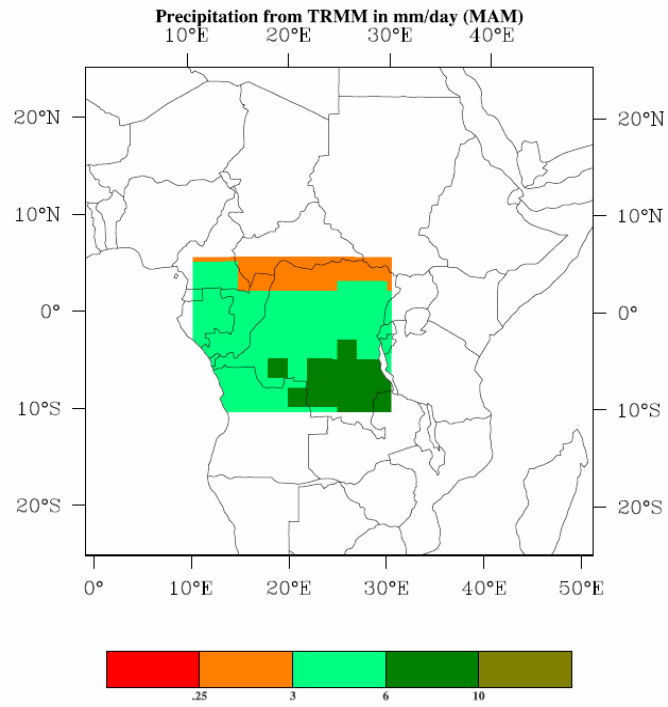
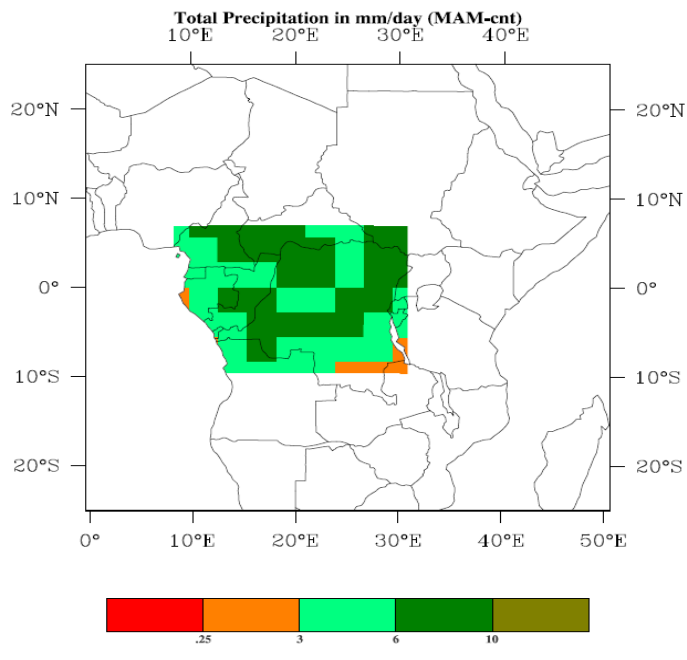


Figure 2.2 Net Solar Flux (surface), Clear Sky Net Solar Flux and Precipitation

The Clear Sky Net Solar flux at the surface (figure 2.2) has a higher correlation to total precipitation in comparison to the correlation between Net Solar flux and precipitation. This fact hints at the likelihood of inaccuracies in the current cloud parameterization within the CAM3. In a convectively active area like the Congo Basin the shortcomings of the cloud parameterization scheme are likely to be enhanced.



(a)



(b)

Figure 2.3 MAM, (a) TRMM and (b) CAM3 (control) simulated rainfall- Congo basin

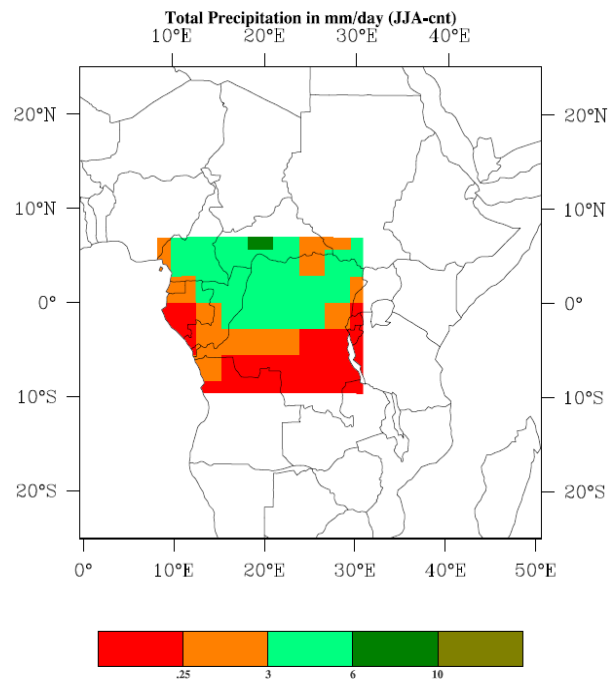
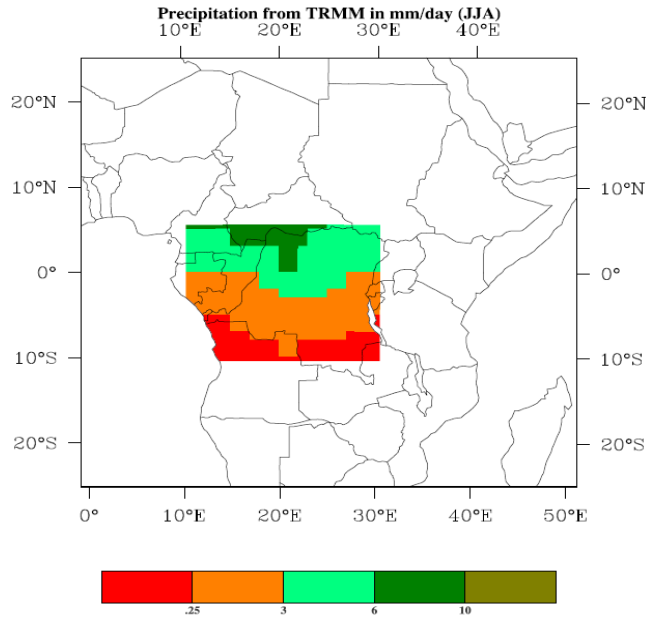


Figure 2.4 JJA, (a) TRMM and (b) CAM3 (control) simulated rainfall- Congo Basin

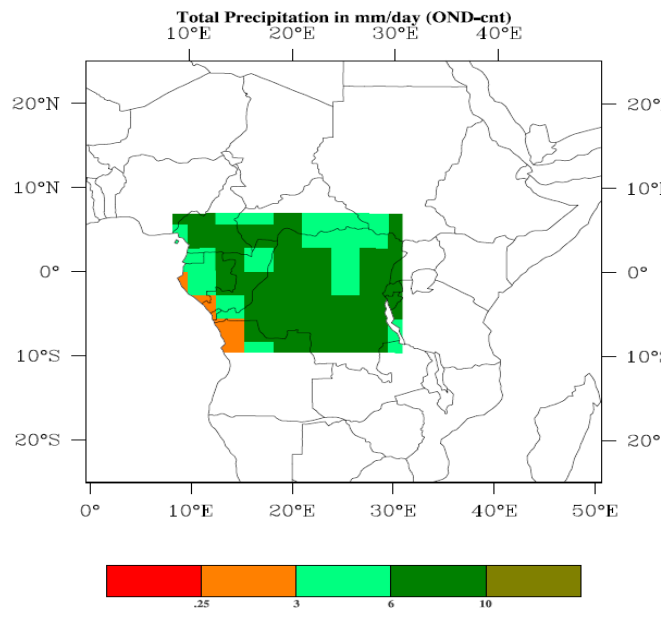
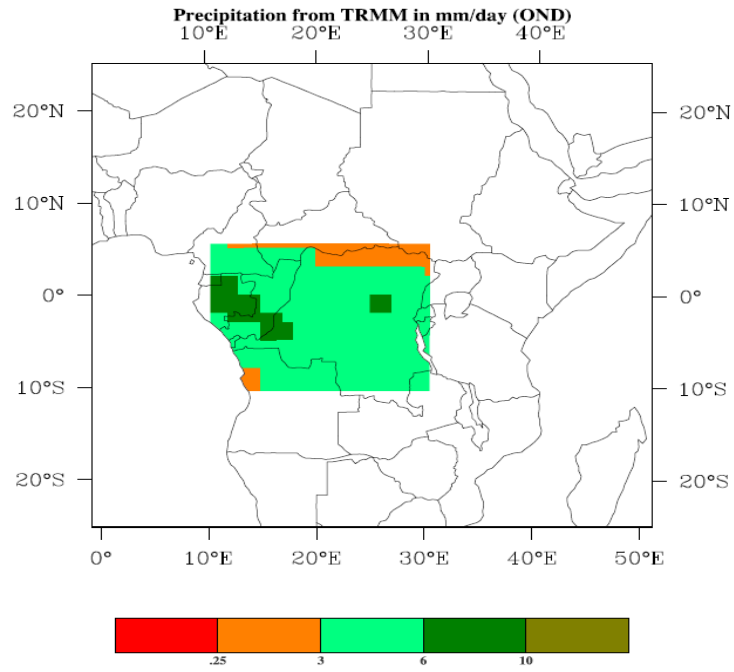


Figure 2.5 OND, (a) TRMM and (b) CAM3 (control) simulated rainfall- Congo Basin

2.2.3 Simulation of the Inter-Tropical Convergence Zone

Maximum rainfall in the Central Equatorial region of Africa is usually collocated with the Inter-Tropical Convergence Zone over the African Continent (ITCZ). The ITCZ is characterized by a belt of low-level convergence and upper-level divergence with strong upward motion, deep convection and heavy rainfall. The ITCZ migrates seasonally across the equator in response to the position of the sun in the tropics of Cancer, Capricorn and the Equinox. Usually the shift is between 8°N in April-November and 8°S in December-March. This phenomenon is observable from satellites and from the rain-gauge data collections on the ground. Most GCM's have not been able to reproduce the seasonal migration of rainfall in phase with the location of the ITCZ (Gates et al 1999, Hacks et al 1998). This failure to simulate the ITCZ location has been a long standing challenge in the climate modeling circles.

The zonal average precipitation values for the MAM, JJA and OND seasons are shown in figure 2.6 (a), figure 2.6 (b) and figure 2.7 respectively. They indicate that maximum precipitation is always located north of the equator. Its migration southwards is simply a spread of the rainfall maxima region and stays northwards of the 5°S latitude. This indicates that the CAM3 like other GCMs fails to simulate correctly the migration of the ITCZ to the south during the boreal winter.

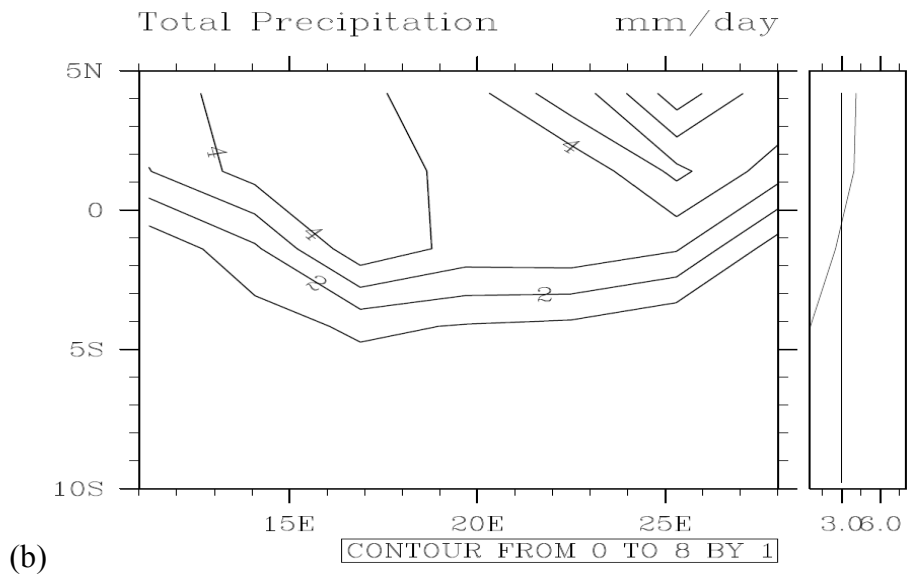
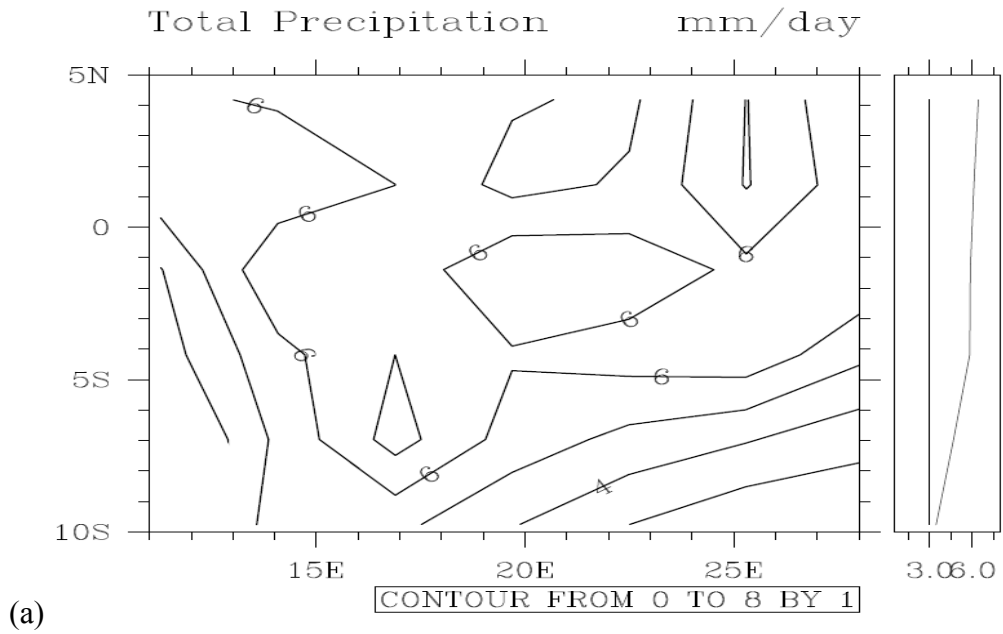


Figure 2.6 Zonal Averages - (a) MAM PPT and (b) JJA PPT. The box on the extreme right shows the range and zonal average values of precipitation

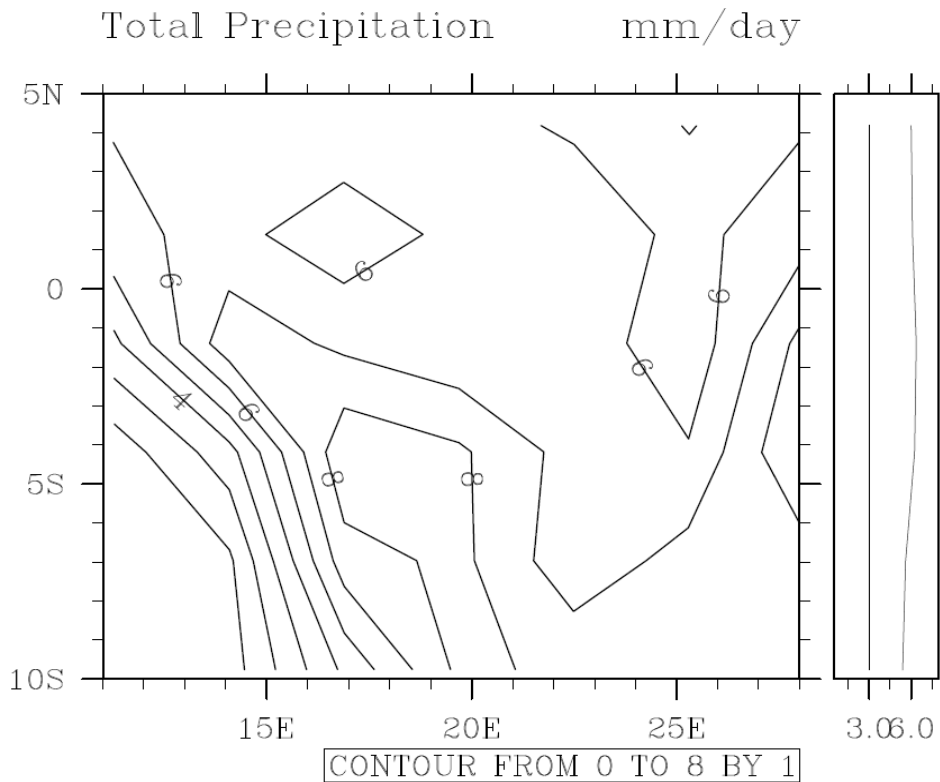


Figure 2.7 Zonal Averages -OND PPT. The box on the extreme right shows the range and zonal average values of precipitation.

2.2.4 Simulation of Soil Water

The sensitivity of climate to vegetation and other lands use changes is dependant on the hydraulic characteristics of the soil. The correct simulation of regional and global soil water conditions by the model is therefore a good test of its fitness for atmosphere-land surface interaction studies. The coupled CAM3/CLM3 (global) simulation of the soil water content at the surface layer for the period 1980-1984 is shown in figure 2.8. The simulation is in closer agreement with the soil climate map of the US department of Agriculture, Natural Resources Conservation Service (USDA-NRCS), Soil Survey Division, shown in figure 2.9.

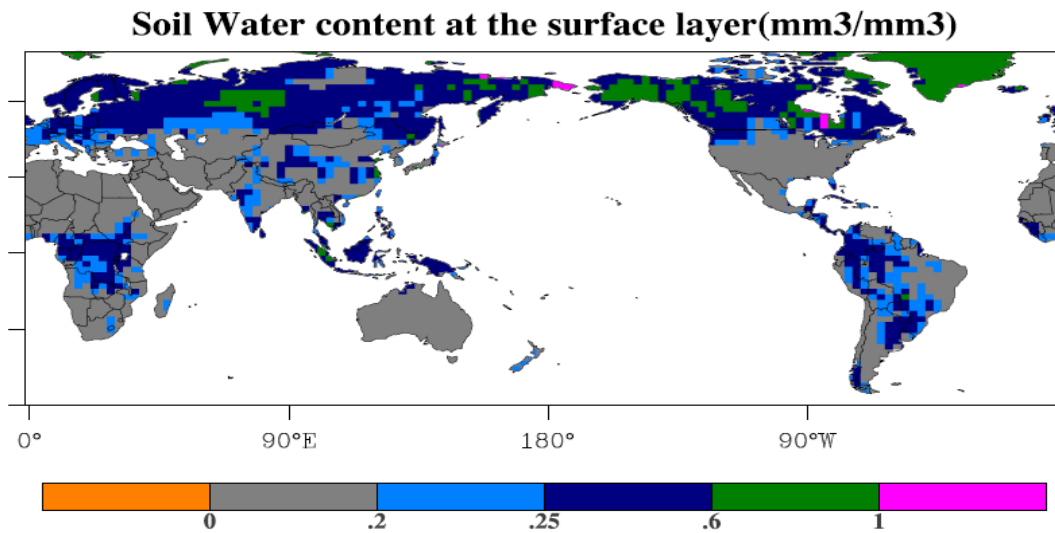


Figure 2.8 CAM3/CLM3 simulated average soil water content at the surface layer (1980-1983)

Even though the soil climate map of the US department of Agriculture is only an assessment of the water holding capacity of the soils and not the actual quantity of the water held, the similarity of the pattern to the CAM3/CLM3 simulation gives credence to the model formulation of global soil water characteristics.

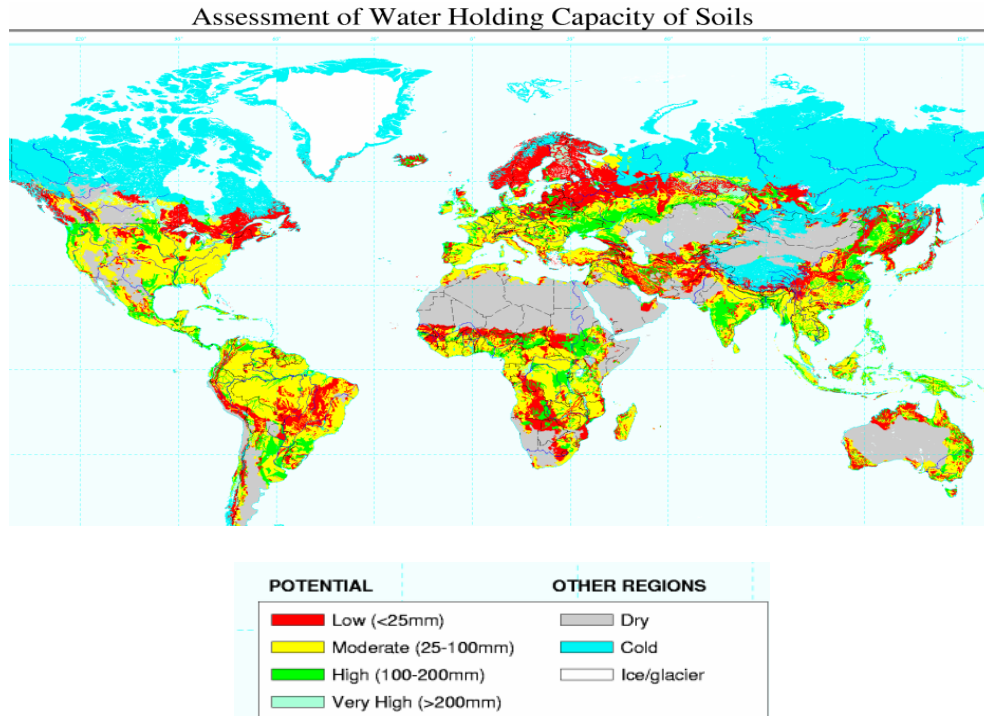


Figure 2.9 Source: Soil map and soil climate map, USDA-NRCS, Soil Survey Division, World Soil Resources, Washington D.C.

Validation of soil water characteristics at higher resolutions in the tropics is restricted by the availability of field data. The importance of soil parameters in the hydrology of the tropics has been ably captured in Osborne et al's, (2004) paper. The authors noted that the impact of soil parameterization on GCM climate simulation is relatively unexplored partly due to the lack or difficulty in acquiring quality global information on soil characteristics, as well as the large variation of soil properties on the subgrid scales. The close simulation of the global soil water by CAM3/CLM3 should therefore be considered as a satisfactory base for regional hydrological studies.

2.3 Temporal and Spatial Variability of Precipitation (EOF Analysis)

Statistical analysis of the spatial and temporal distribution of rainfall in the basin using Empirical Orthogonal Functions (EOFs) indicates a latitudinal shift in rainfall intensity in phase with the Inter-tropical Convergence Zone as shown in the time series of the expansion coefficient associated with the first mode (figure 2.10) and the corresponding spatial pattern of this mode (figures 2.11). The first mode explains 55 percent of the rainfall variability and is indicative of the predominance of the annual cycle over any other phenomena in the rainfall pattern. The second mode (figure 2.12 and figure 2.13) explains 13% of the variability and depicts a periodicity of roughly 3 years.

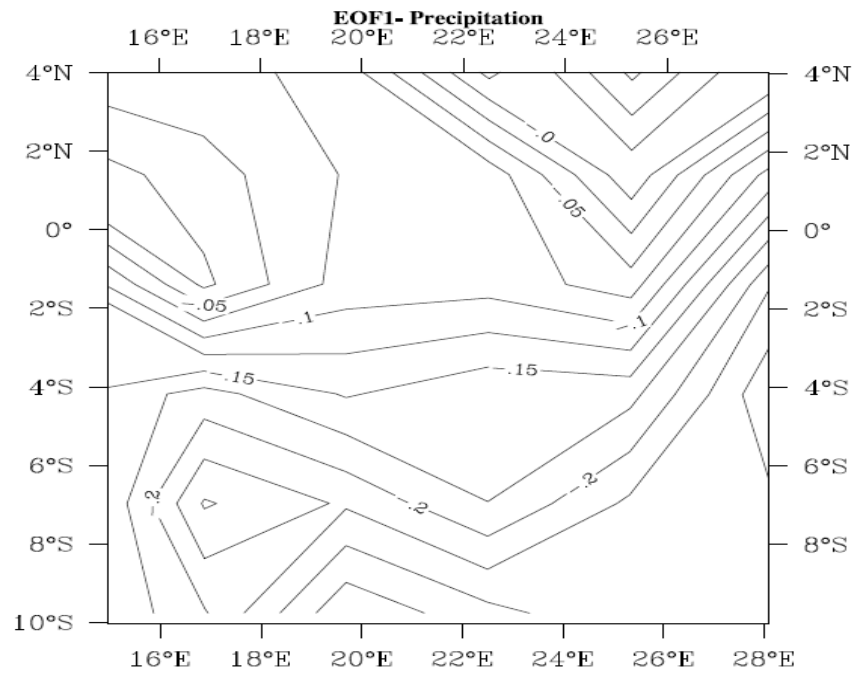


Figure 2.10 EOF mode 1 spatial pattern of precipitation

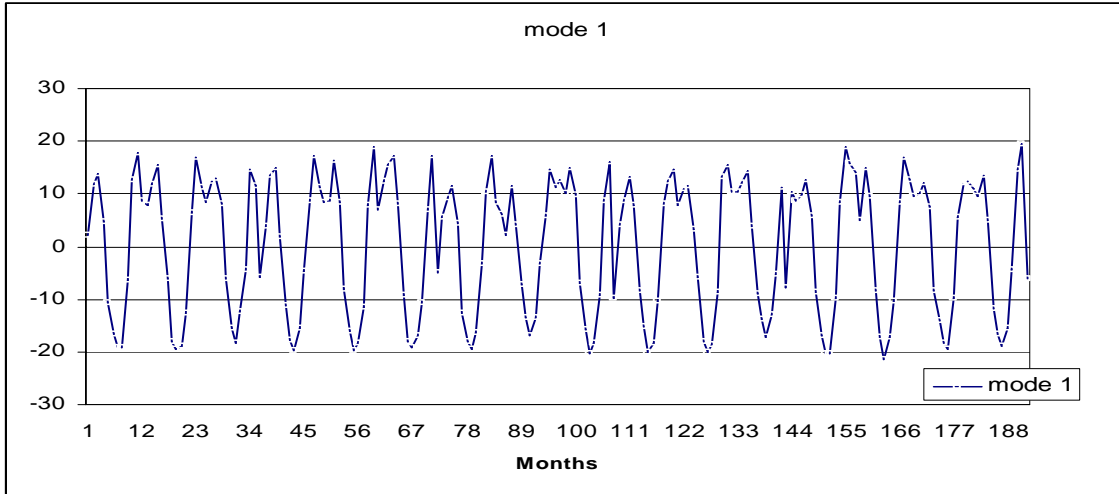


Figure 2.11 Mode 1 - temporal pattern of precipitation

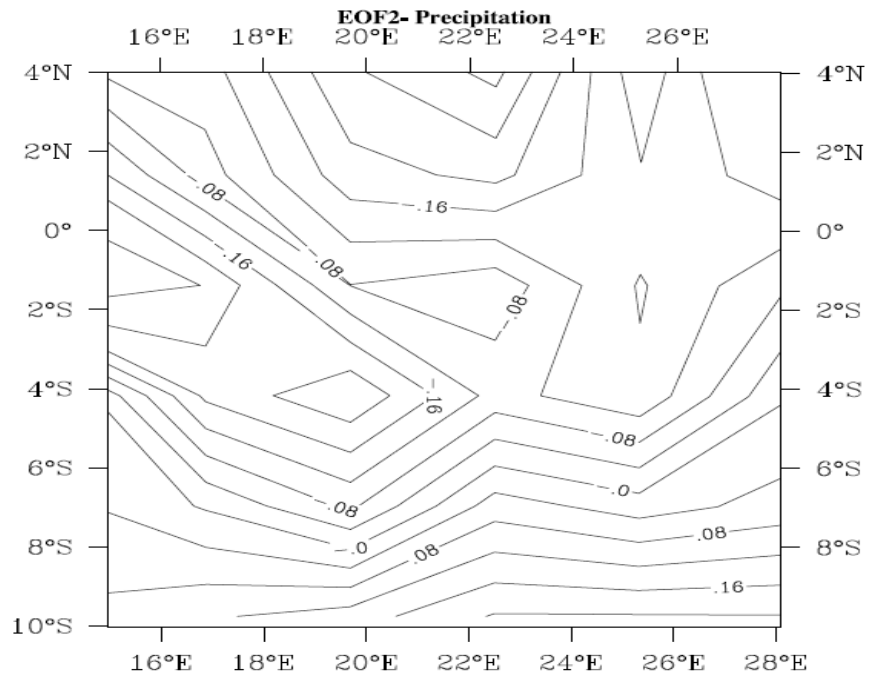


Figure 2.12 Mode 2 – Spatial pattern of precipitation

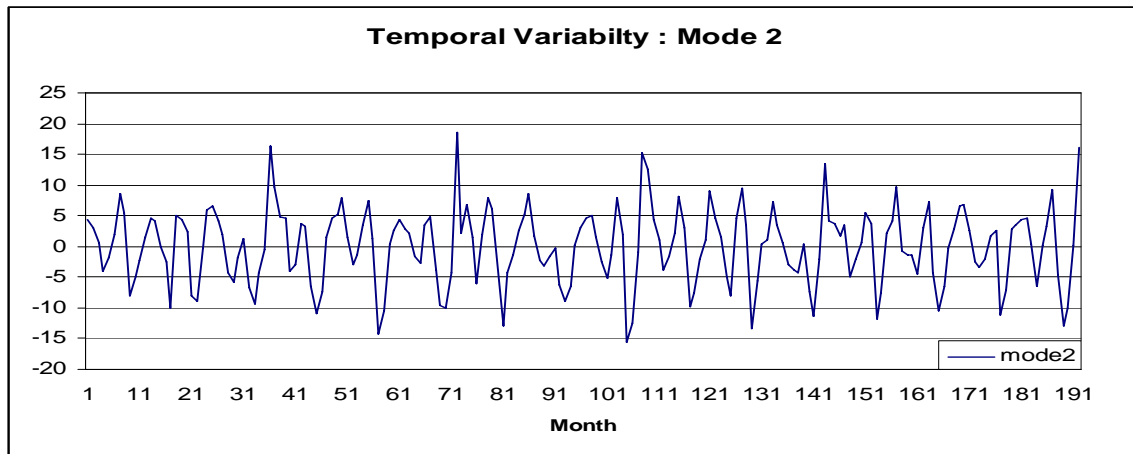


Figure 2.13 Mode 2 – temporal pattern of precipitation

The EOF mode 1 results indicate that most of the variance is explained by the seasonal change in mean rainfall in the southern part (south of 2°S latitude) of the basin, figure 2.10. The EOF mode 2 results implies that the next most important source of variance in rainfall data is the tri-annual change in mean rainfall which is more predominant in the Northern part of the basin, figure 2.12. The 3 year periodicity depicted in mode2 is probably an indication of the ENSO mechanism which is responsible for many of the well established rainfall teleconnections in the continent including strong tendencies for opposite anomalies in equatorial and southern Africa (Nicholson, 1997)

2.4 EOF Analysis of Channel Runoff

A similar (EOF) analysis for River Congo model generated channel runoff is shown in figure 2.14. The first mode explains 87% of the runoff variability. A reconstruction of the data from the EOFs and the expansion coefficients is performed mathematically as

$$R = \sum_{j=1}^p a_j (EOF_j) \quad (1)$$

where EOF_j is the eigenvector associated with the j th eigen value and a_j is the corresponding J th expansion coefficient. A graphical plot of R results in figure 2.16. The figure correctly locates the Congo River Channel even though the truncation was made only at the four largest eigenvectors i.e. $j=4 < p$. This implies that the first 4 eigenvectors are capturing the dynamical behavior of the channel runoff.

However, model generated Congo River runoff values in the controlled run are not realistic and are more than twice the observed runoff during the rainfall season. Congo River runoff simulations and its modification will be discussed in chapter 4.

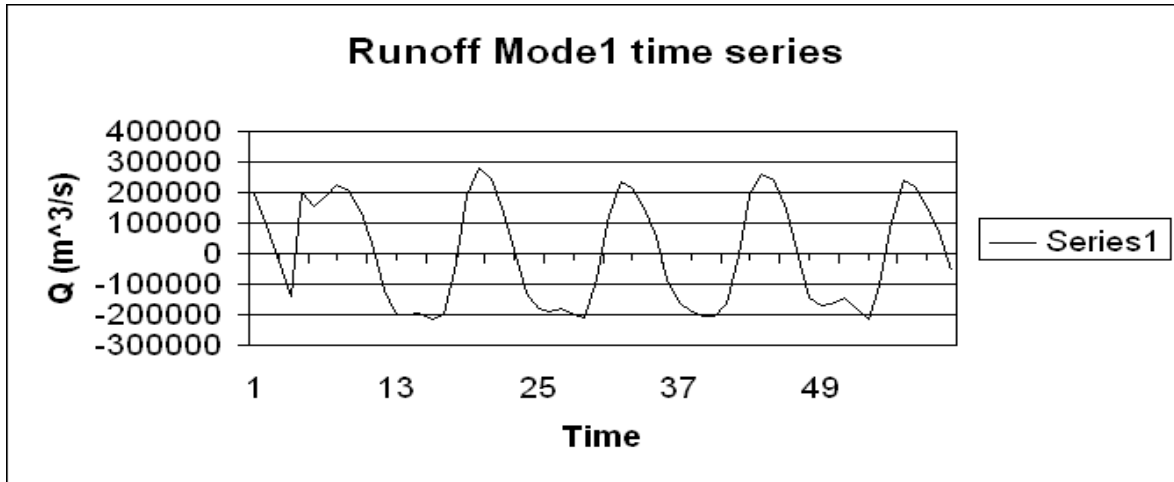


Figure 2.14 Mode 1- temporal variability of runoff at the Kinshasha gauging station

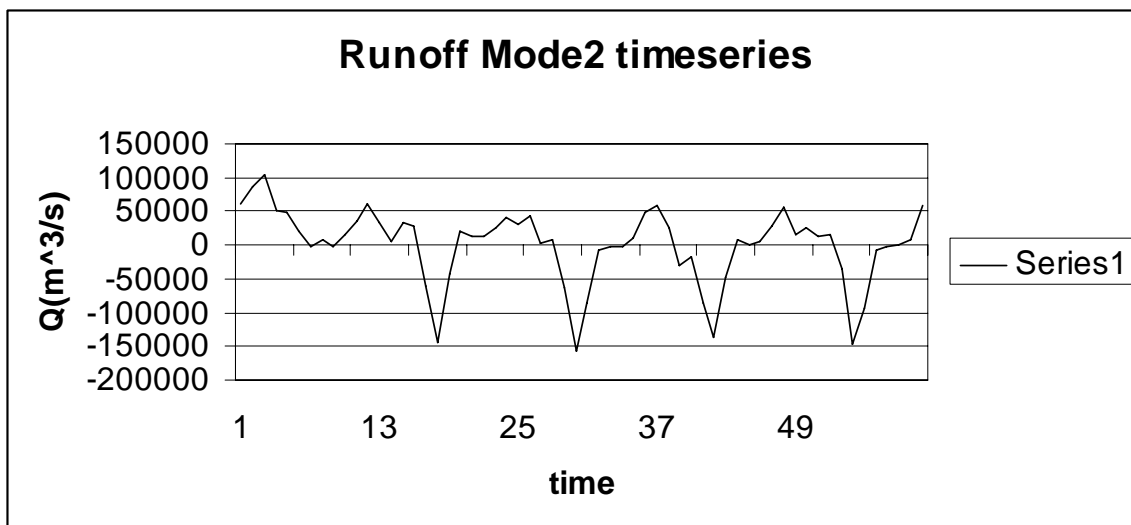


Figure 2.15- Mode 2 –temporal variability of runoff at the Kinshasha gauging station

CLM3-(RTM) SIMULATION
_multiply_ev_# EOF ANALYSIS FOR CONGO RIVER DISCHARGE
Mean 0.00853029 Max 0.25784 Min -0.000132065

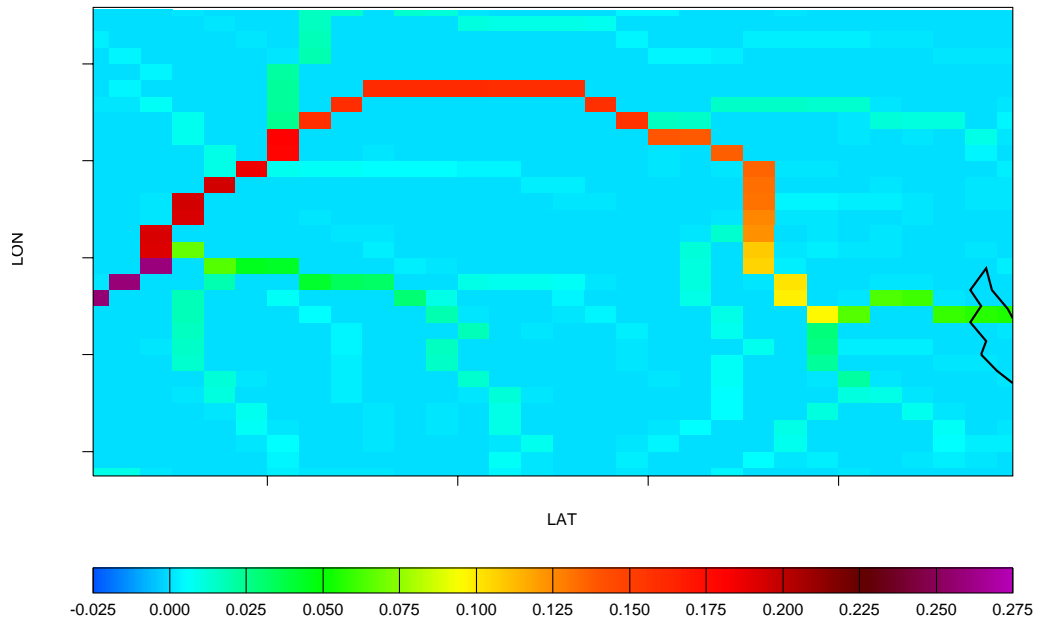


Figure 2.16 Reconstructed plot from the EOF analysis of the Congo River runoff

CHAPTER 3

EXPERIMENTS

3.1 Design

Experiments on the impact of deforestation of the Congo Basin on climatic parameters like precipitation, evaporation and river runoff were performed by simulating three different scenarios, namely, high, medium and low deforestation over a 15 year period (1979-1994).

In the CLM3 model, vegetated surfaces are comprised of up to 4 of 15 possible plant functional types (PFTs) plus bare ground (Table 3.1). These PFTs differ in physiological and morphological traits along with climatic preferences (Bonan et al. 2002b). The 7 primary PFTs are needleleaf evergreen or deciduous tree, broadleaf evergreen or deciduous tree, shrub, grass, and crop. These 7 primary PFTs have been expanded to 15 physiological variants based on climate rules to distinguish arctic, boreal, temperate, and tropical PFTs, C_3 and C_4 grasses, and evergreen and deciduous shrubs (Table A1.1).

These plant types differ in leaf and stem optical properties that determine reflection, transmittance, and absorption of solar radiation (Table A1.2), root distribution parameters that control the uptake of water from the soil (Table A1.3), aerodynamic parameters that determine resistance to heat, moisture, and momentum transfer, and photosynthetic parameters that determine stomatal resistance, photosynthesis, and transpiration (Table A1.4). Parameter values are as in Bonan et al. (2002a) with root distribution parameters from Zeng (2001). In the control run, the composition and

abundance of PFTs within a grid cell are time-invariant and are prescribed from 1-km satellite data (Bonan et al. 2002b).

Table 3.1 IGBP Plant functional types in CLM3

CODE	Vegetation Type
0	'not vegetated'
1	'needle leaf evergreen temperate tree'
2	'needle leaf evergreen boreal tree'
3	'needle leaf deciduous boreal tree'
4	'broadleaf evergreen tropical tree'
5	'broadleaf evergreen temperate tree'
6	'broadleaf deciduous tropical tree'
7	'broadleaf deciduous temperate tree'
8	'broadleaf deciduous boreal tree'
9	'broadleaf evergreen shrub'
10	'broadleaf deciduous temperate shrub'
11	'broadleaf deciduous boreal shrub'
12	'c3 arctic grass'
13	'c3 non-arctic grass'
14	'c4 grass'
15	'corn'
16	wheat'

3.1.1 Experiment 1 (High Deforestation)

In this experiment the current plant functional type which is configured in the CLM3 as 44.5% broadleaf evergreen tropical trees, 14.4% Broadleaf deciduous tropical trees, 15.4% C3 Non-Arctic grass, 24.5% C4 grass, 1.17% corn and 0.12% Non-Vegetation (Figure 3.1) was altered to 96 % C4 grass, 2% C13 grass, 1 % corn and 1% broadleaf evergreen tropical trees (Figure 3.3) to mimic a long term (at least 10 years)

permanent change of plant functional type and hence a change in the ecosystem of the Congo basin. The percentage of the vegetated portion of the grids occupied by the various plant functions types are shown in Figure 3.2 for the control case and Figure 3.4 for the highly deforested case.

In aggregate this is essentially a shift in the optical properties, roughness length (aerodynamic properties), root distribution and photosynthetic parameters of the predominant land cover from forest to savannah grass- type vegetation.

3.1.2 Experiment 2 (Medium Deforestation)

In this scenario the broadleaf deciduous tropical trees was completely wiped out but the broadleaf evergreen tropical trees was slightly reduced to 40% while the C4 grass, non-arctic grass and corn now covered 57%, 2% and 1% of the land surface respectively, figure 3.5.

The percentage of the vegetated portion of the grids occupied by the various plant functions types in this experiment is shown in figure 3.6.

3.1.3 Experiment 3 (Low deforestation)

This scenario assumes equal size coverage of land surface by the evergreen tropical trees, evergreen deciduous trees, C4 grass and C3 non arctic grass type i.e. at 25 % each.

3.1.4 Experiment 4 (Reforestation)

To amplify the impact of vegetation on the parameters in question the very unlikely situation of a doubling in the forest size is considered. The evergreen tree covers 96 %, C4 grass covers 2 %, while both corn and non –arctic grass cover 1% each.

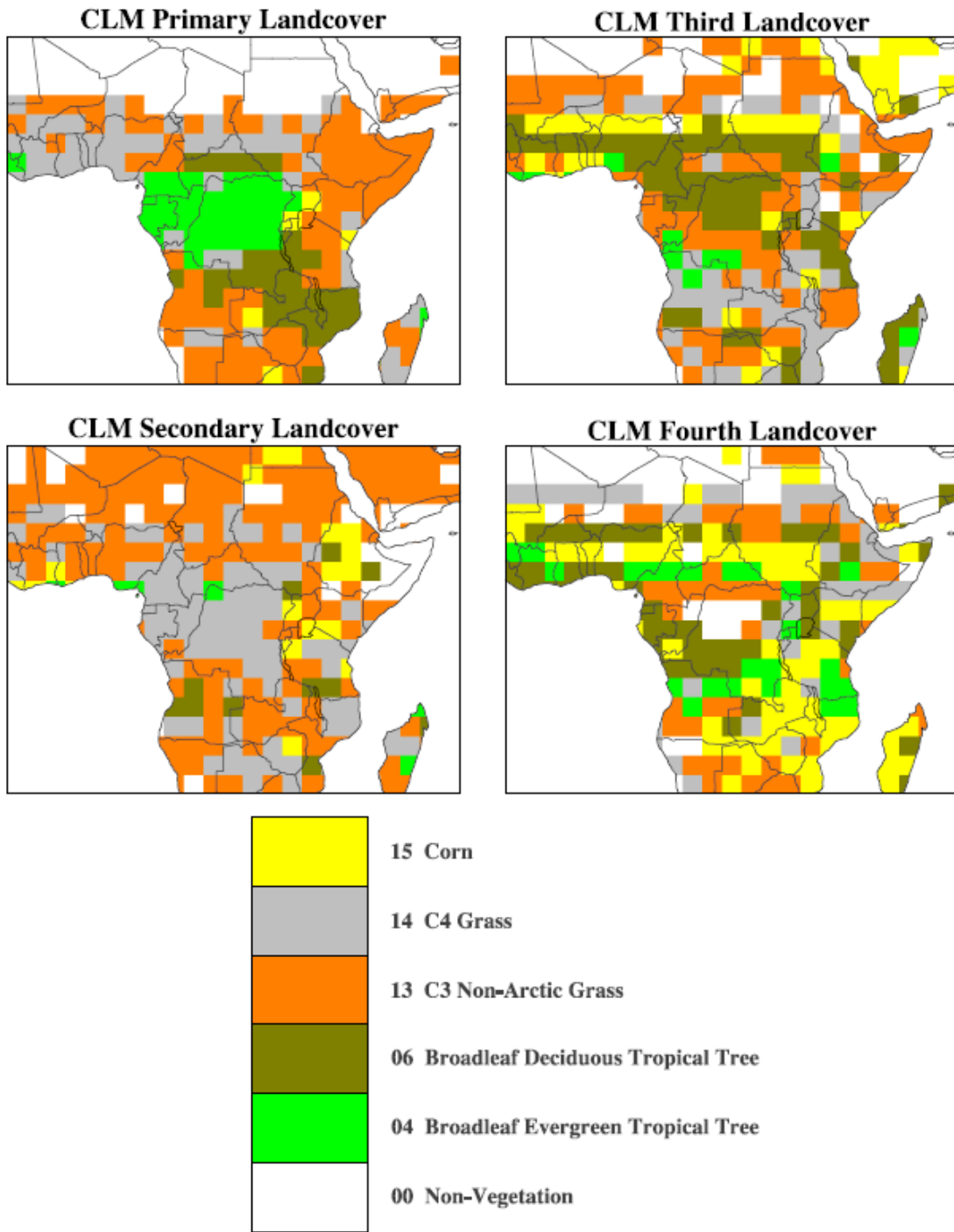


Figure 3.1 Land-cover types for the control simulation

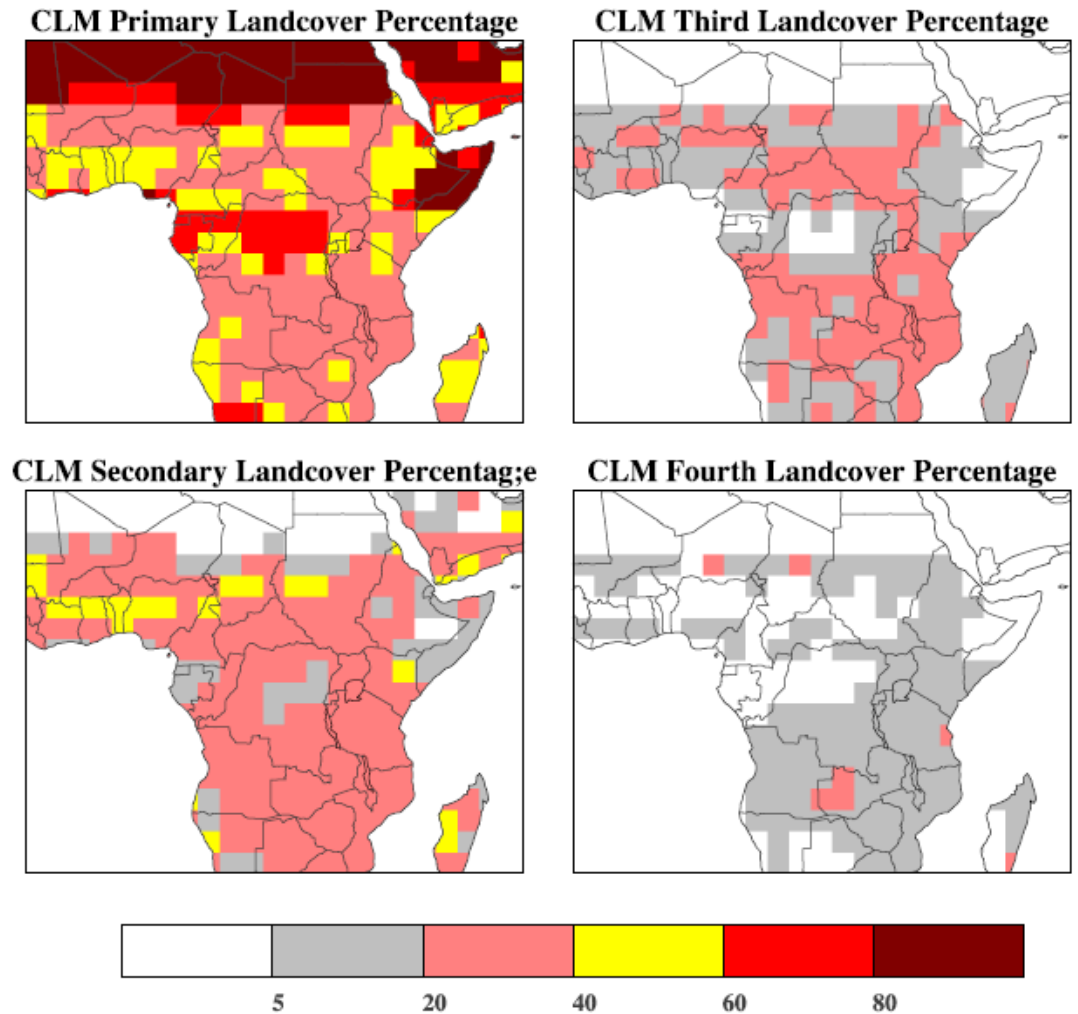


Figure 3.2 Land-cover percentages for control simulation

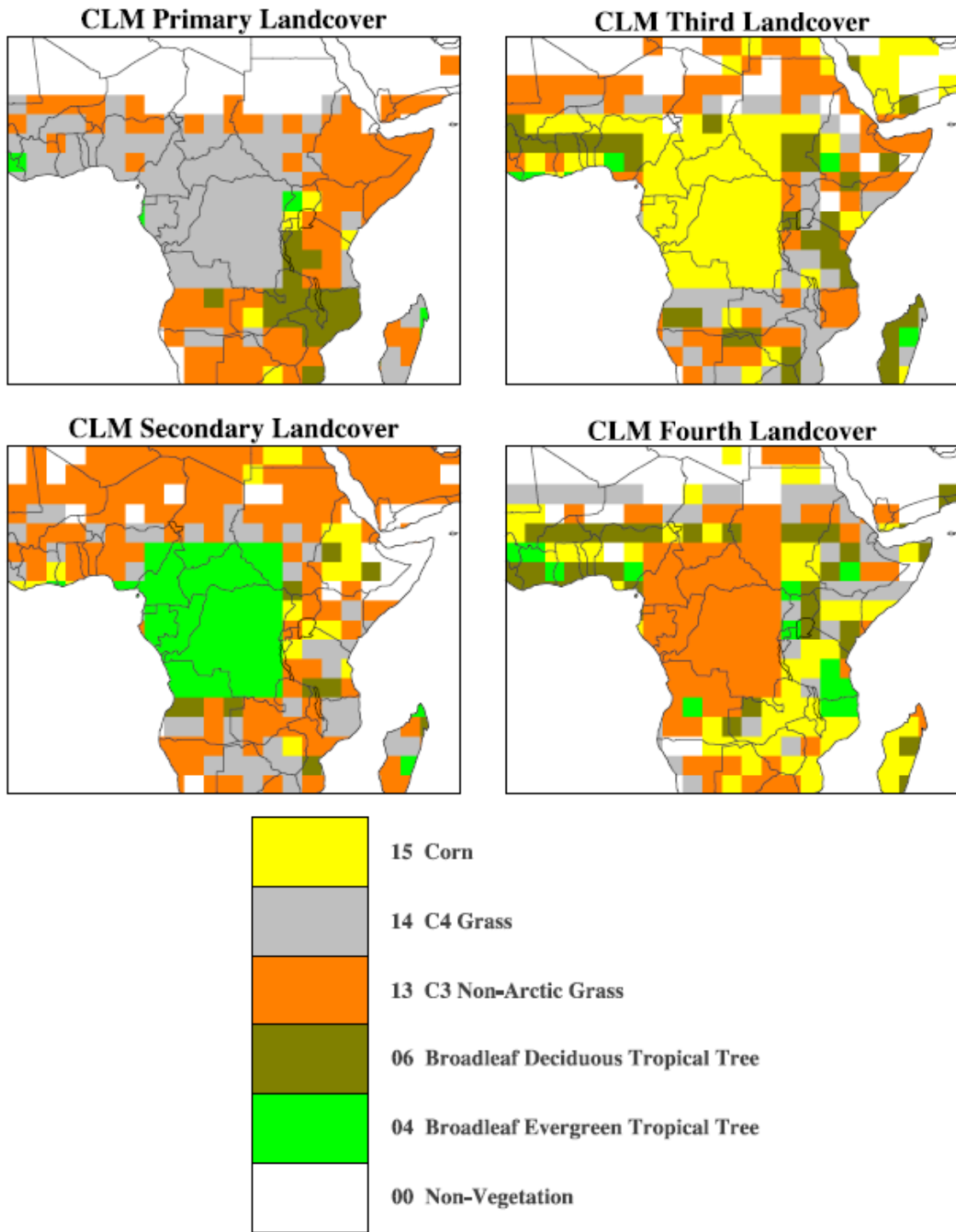


Figure 3.3 Land-cover types for experiment 1 -high deforestation

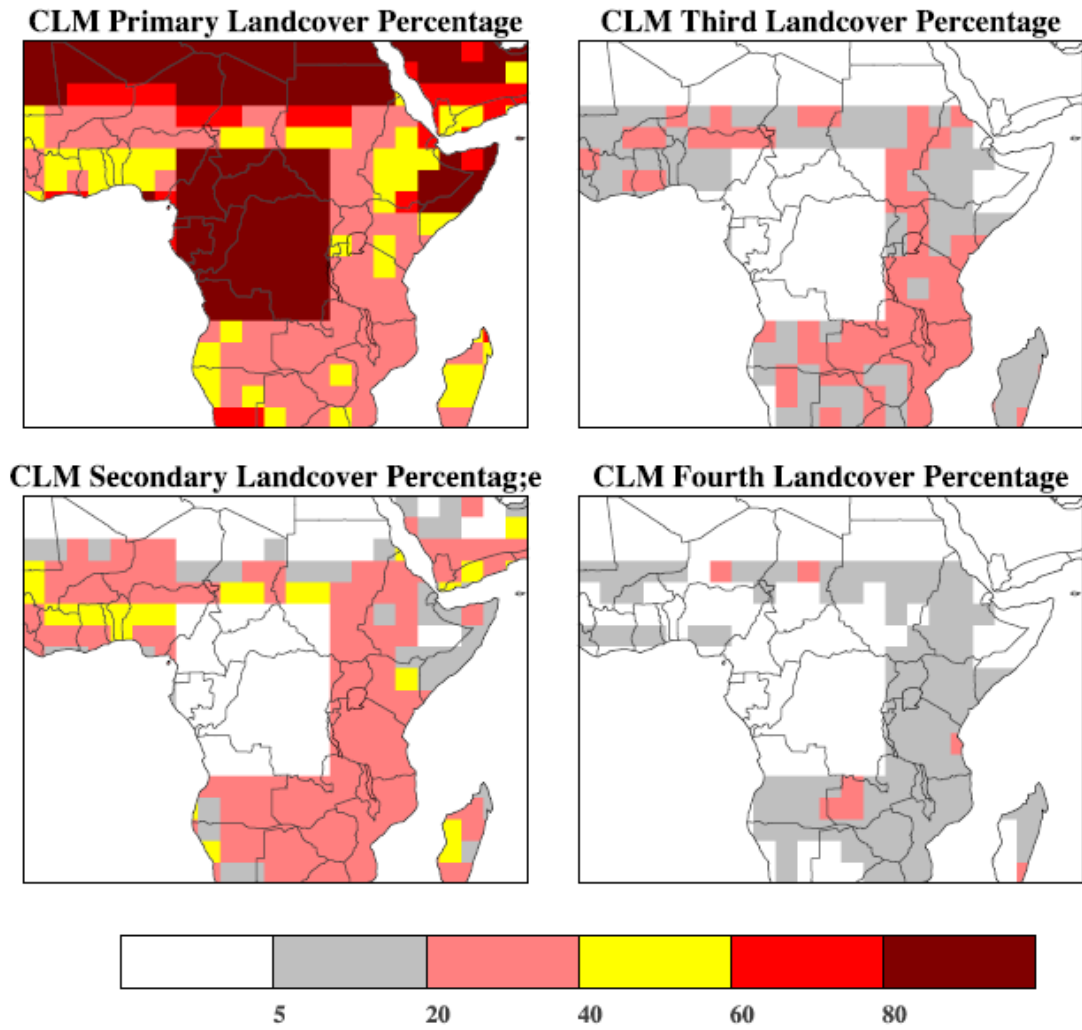


Figure 3.4 Land-cover percentages for experiment 1 –high deforestation

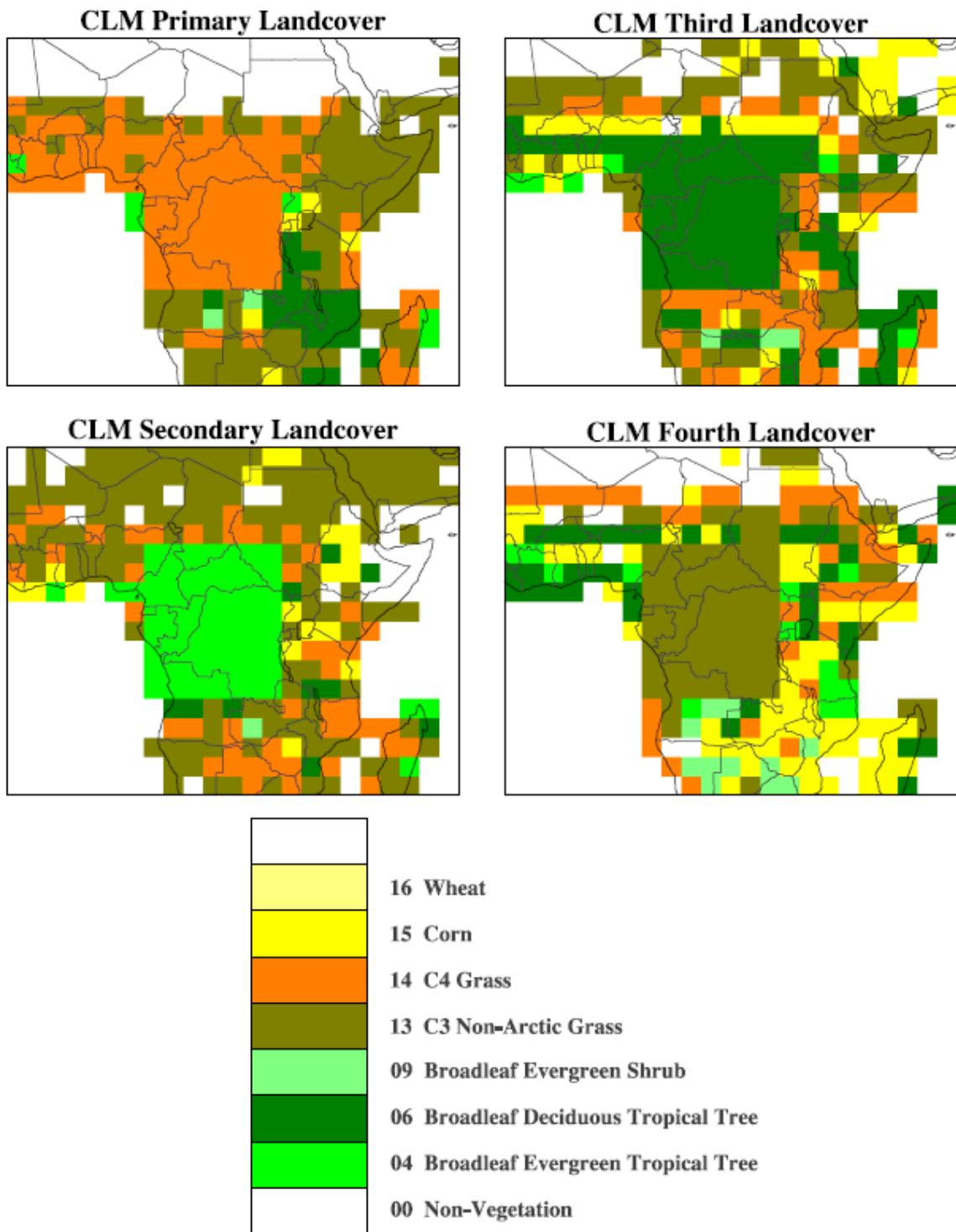


Figure 3.5 Land-cover types for experiment 2 – medium deforestation

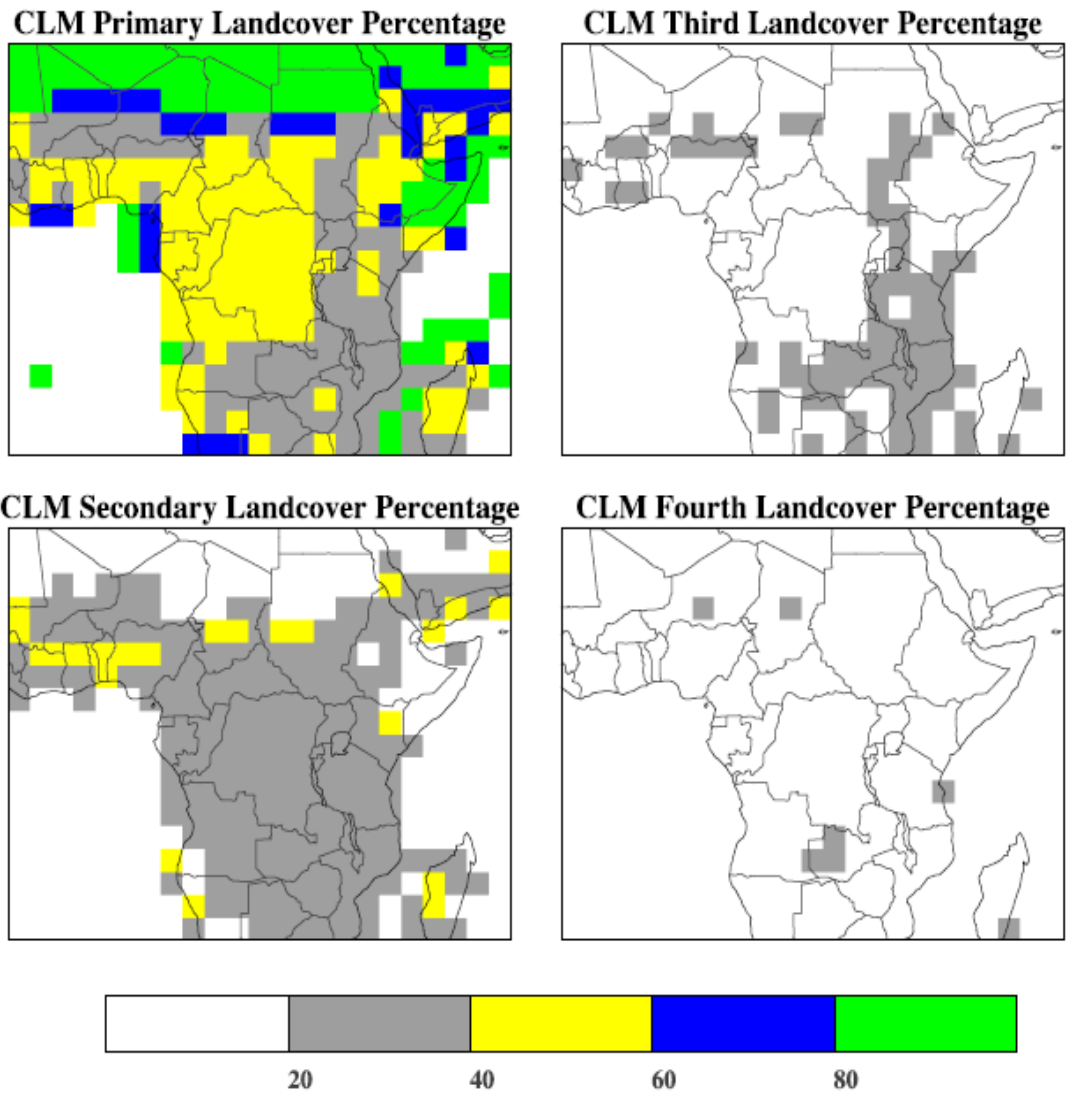


Figure 3.6 Land-cover percentages for experiment 2 – medium deforestation

3.2 Results and Discussions

3.2.1 Precipitation

There are mixed signals in the temporal change in rainfall following the various levels of deforestation.

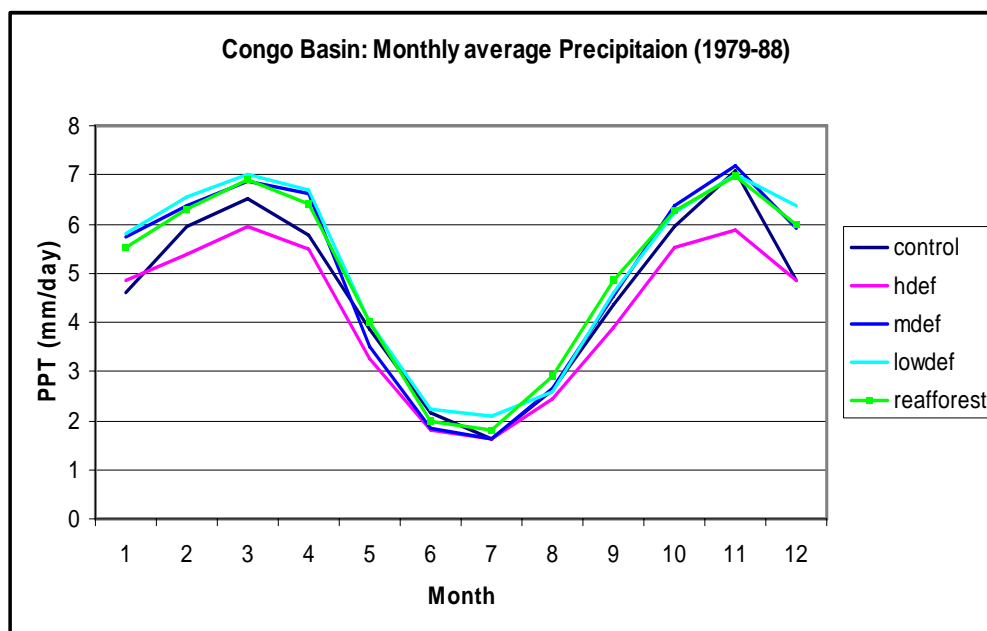


Figure 3.7 The impact of different levels of deforestation on rainfall

In experiment 1, namely, high deforestation, there is a decrease of precipitation by an average of 0.3 mm/day during the rainy season of MAM and a more noticeable decrease (a maximum of about 1 mm/day in November) for the OND. There is no significant change in precipitation for the drier period extending from May to September following high deforestation. The reduction in precipitation during the MAM period is predominant

in the Northern part of the basin where the corresponding reduction in evapotranspiration inhibits the intensity of the ITCZ-induced deep convection. The reduction in precipitation (experiment 1) during the OND period is more widespread in comparison to the MAM period.

The time-averaged (temporal) effect of this change on distribution of precipitation is shown in figure 3.7. A paired-sample student's t (Appendix B) test indicates that the decrease in precipitation after high deforestation is significant at the 95% confidence level. A paired-sample t-test is used to side step the possible correlation between the control run and the deforestation experiments. Although this is only a crude and provisional estimate of statistical significance it is a more powerful test of the null hypothesis (i.e. mean precipitation for the control run is equal to the mean precipitation in the experiment) than the ordinary student's t test. The regular student's t test is actually inappropriate in this case since some of the assumptions in such a test (e.g. equal variance in the ensemble) are not strictly applicable to this experiment.

The spatial distribution of the seasonal changes in precipitation for MAM, JJA and OND following high deforestation are shown in figure 3.8, figure 3.9 and figure 3.10 respectively.

The change in precipitation after deforestation does not seem to be linearly dependant on the amount of broadleaf evergreen forest removed but rather on the aggregate properties of the mosaic of the remaining plant functional types. Hence there seems to be an increase in precipitation following low-deforestation (figure 3.7) in comparison to the control run and the high-deforestation scenario.

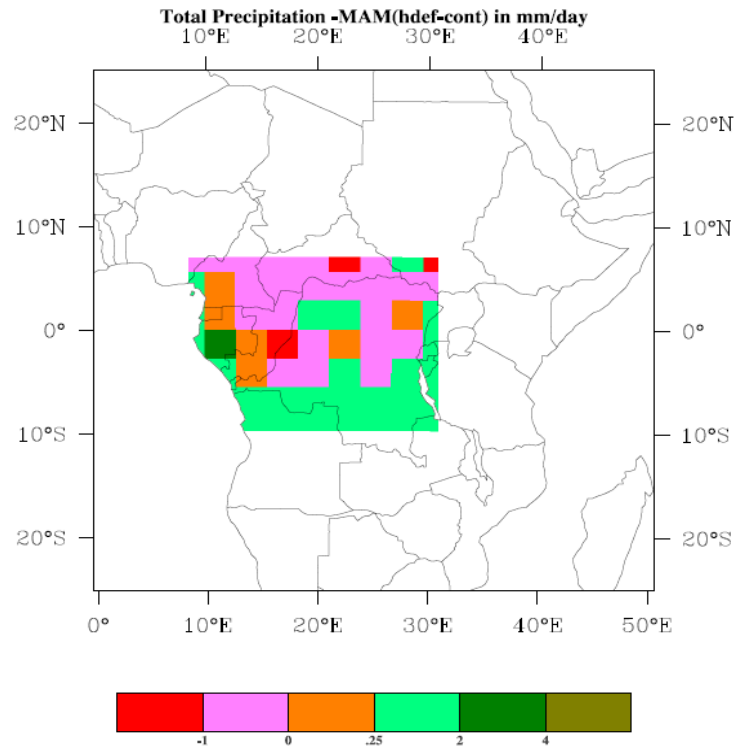


Figure 3.8 Change in precipitation after high deforestation-MAM

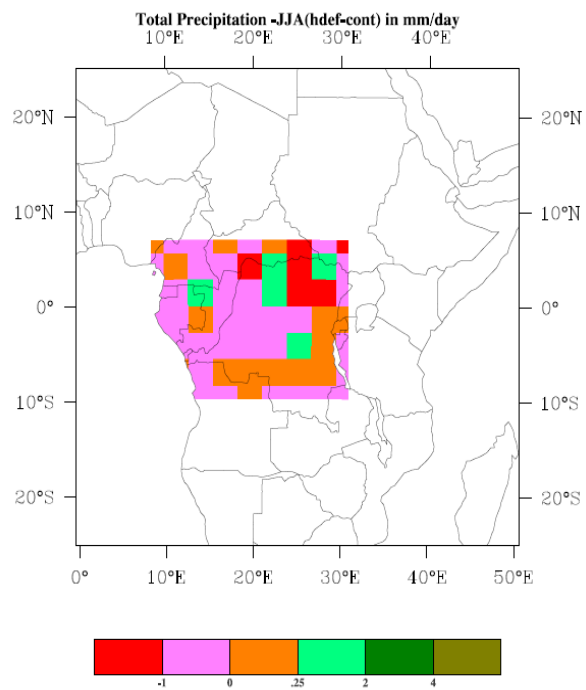


Figure 3.9 Change in precipitation after high deforestation-JJA

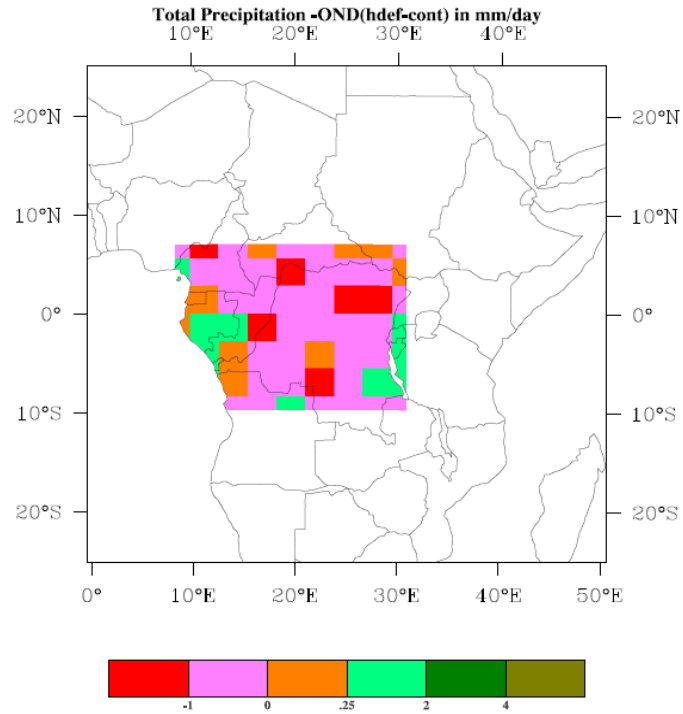


Figure 3.10 Change in precipitation after high deforestation-OND

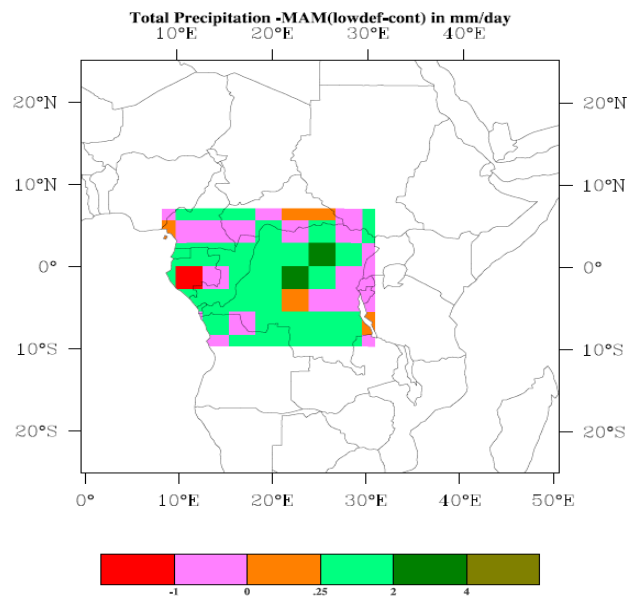


Figure 3.11 Change in precipitation after low deforestation -MAM

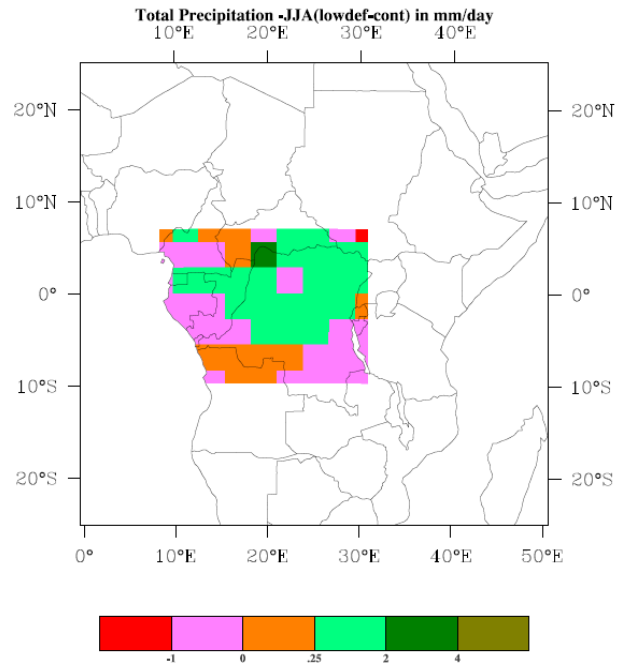


Figure 3.12 Change in precipitation after low deforestation-JJA

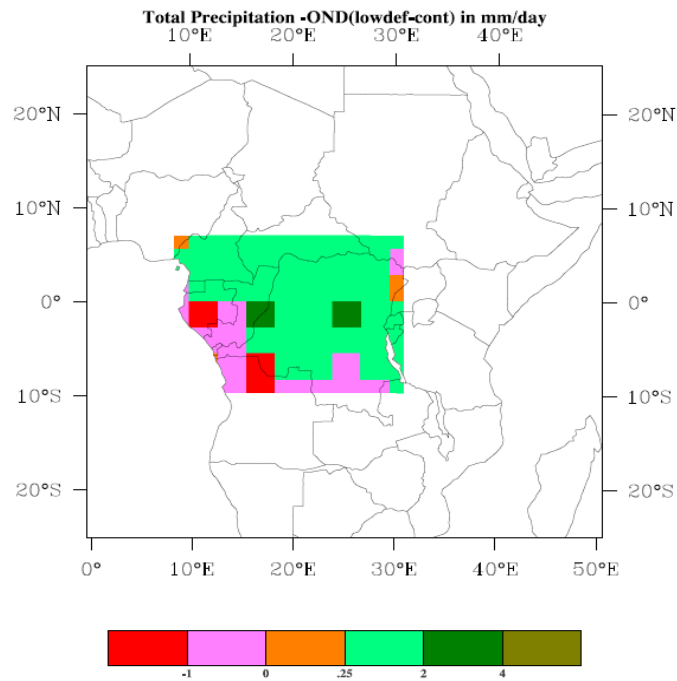


Figure 3.13 Change in precipitation after low deforestation -OND

3.2.2 Evapotranspiration

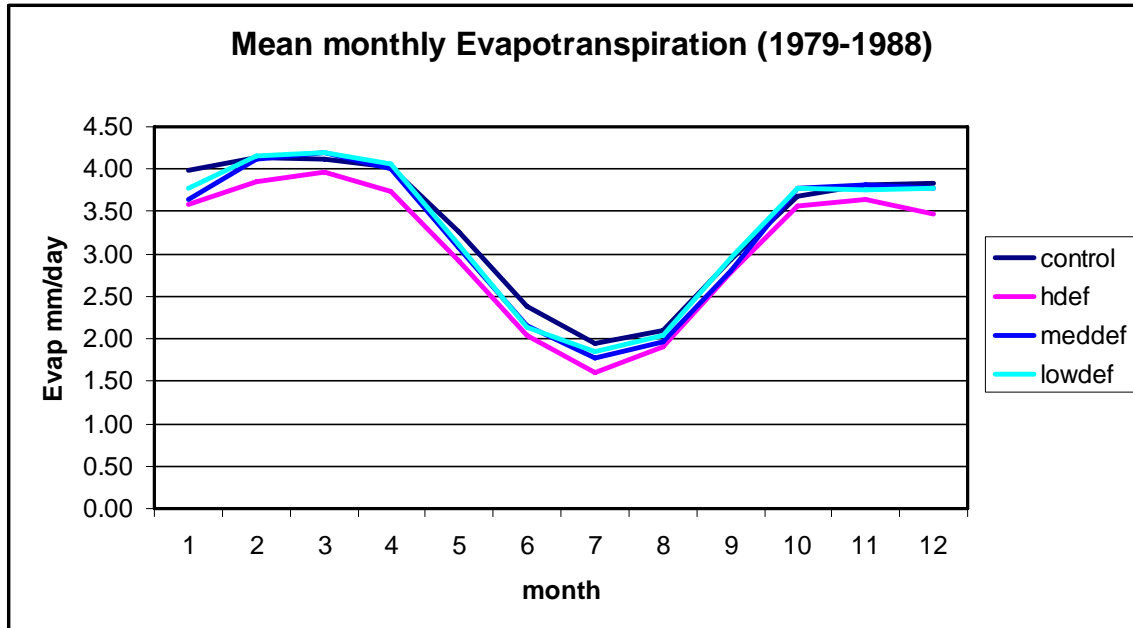


Figure 3.14 The impact of different levels of deforestation on Evapotranspiration

Experiment 1 results show a nearly uniform decrease in evapotranspiration (i.e. ground evaporation plus transpiration from the plants) of about 0.5 mm/day. The resulting changes in the temporal distribution of evapotranspiration are shown in figure 3.14. The change in evapotranspiration following reforestation is shown in separately in figure 3.15 for the sake of clarity.

In general the change in evapotranspiration is less drastic than the change in precipitation for all the experiments (figures 3.18- figure 3.23) as depicted by the prevalence of the purple and brown color coding. This phenomenon gives some weight to

the theory of changes in moisture convergence and divergence from the basin due to changes in the circulation pattern following deforestation.

Experiment 2, medium deforestation, does not significantly alter evapotranspiration for the rainy seasons of MAM and OND but it shows a marked reduction of evapotranspiration in the drier JJA season (figure 3.7). Considering temporal averages experiment 3 (low deforestation) produces almost the same results as experiment 2 for the entire 12 months period.

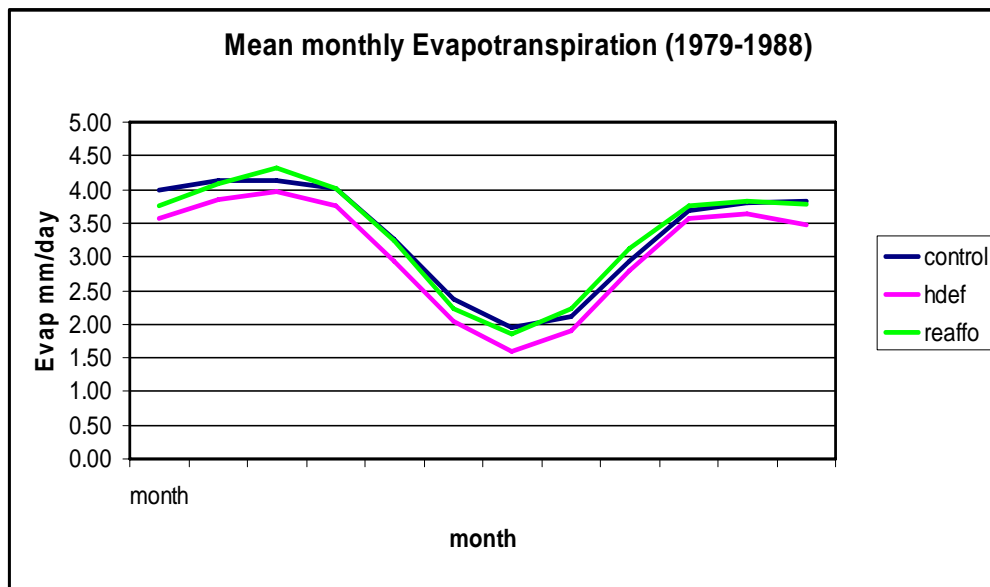


Figure 3.15 Contrasting the impact of deforestation and reforestation on evapotranspiration

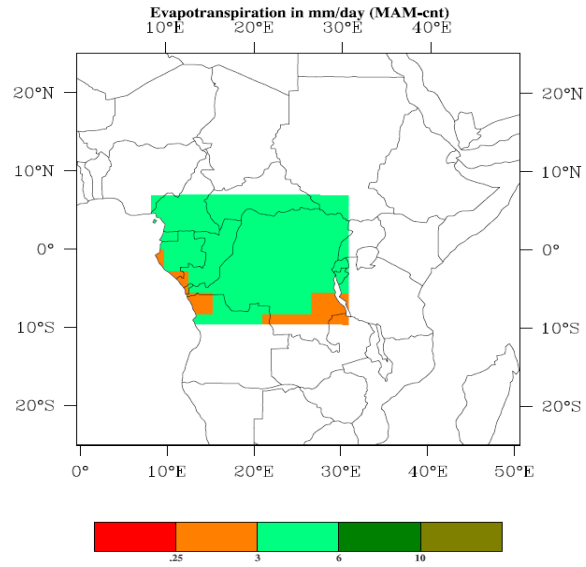


Figure 3.16 Spatial distribution of control evapotranspiration- MAM

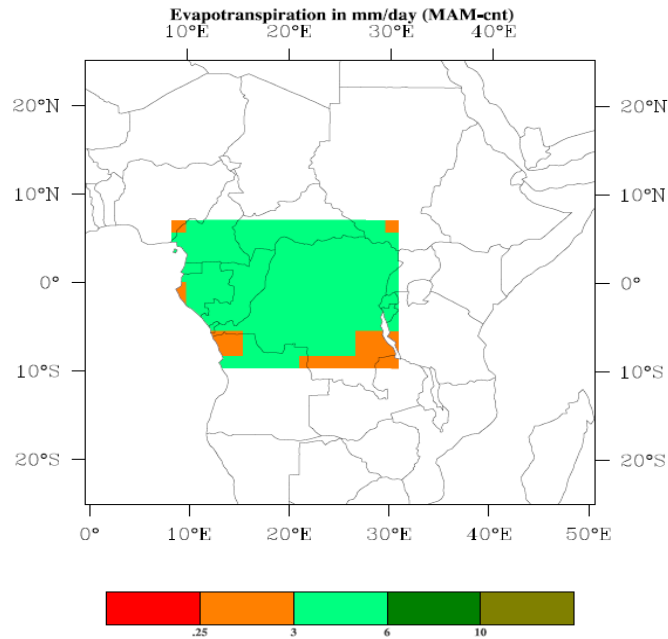


Figure 3.17 Spatial distribution of Experiment 1 evapotranspiration- MAM

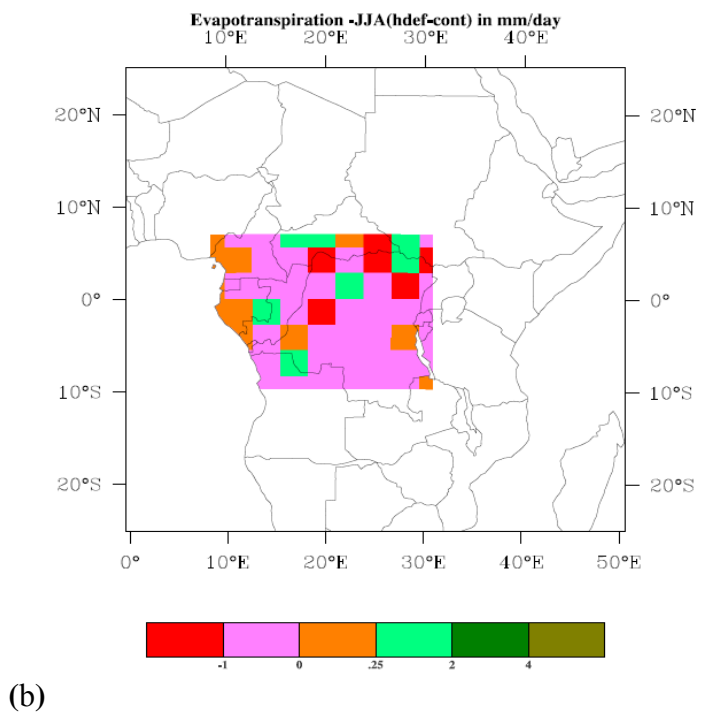
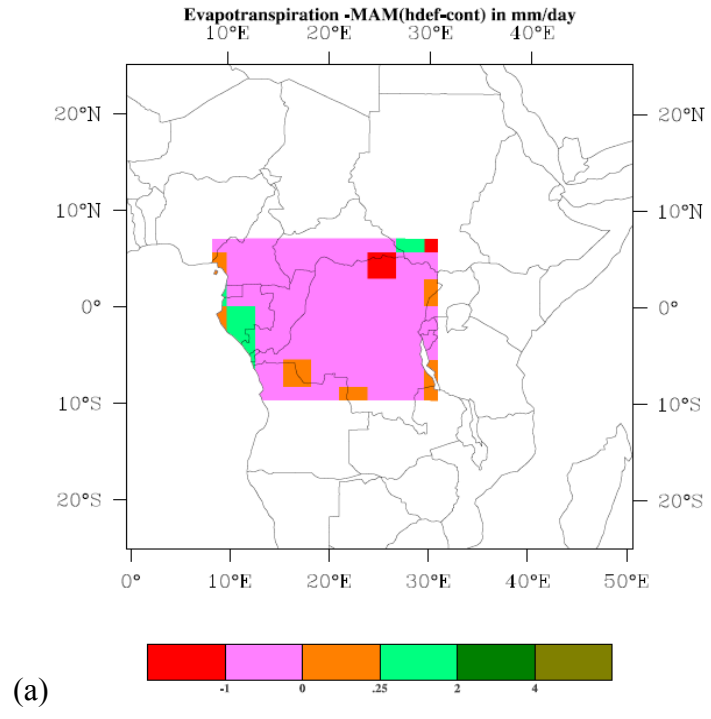


Figure 3.18 Change in evapotranspiration after high deforestation (a) MAM and (b) JJA

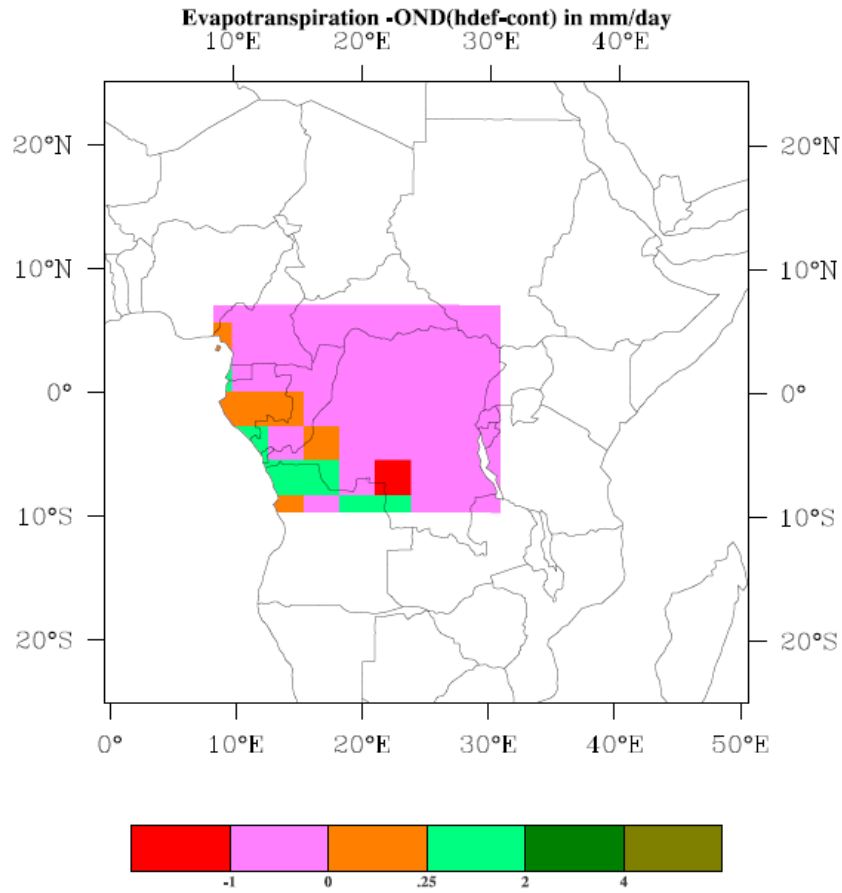


Figure 3.19 Change in evapotranspiration after high deforestation -OND

The spatial distribution of changes in evapotranspiration, however, indicates some differences between experiment 2 and experiment 3. In experiment 3 (low deforestation) there is actually an increase in evapotranspiration in the southern portion of the basin (figure 3.22 a) and a more widespread increase in evapotranspiration in the OND Season.

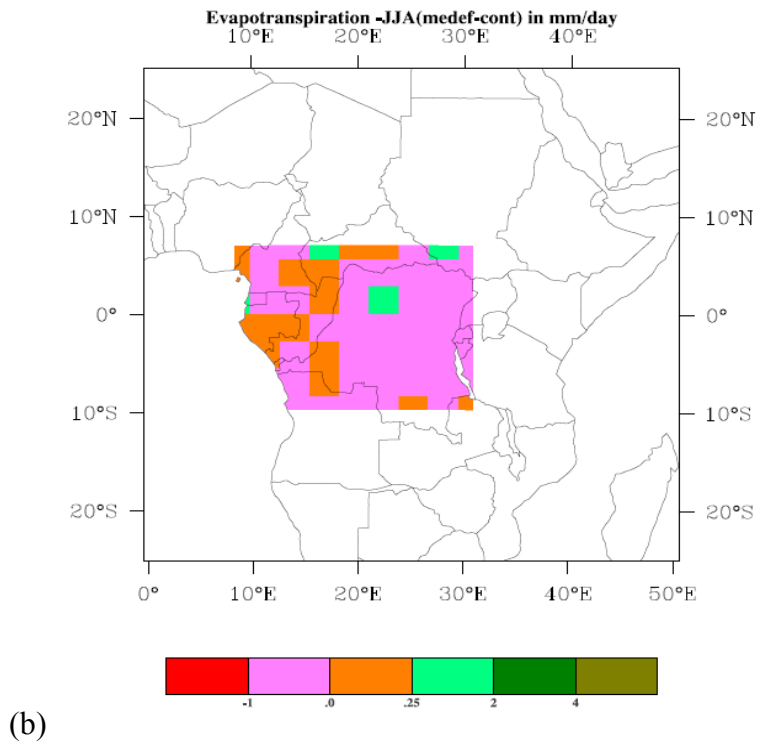
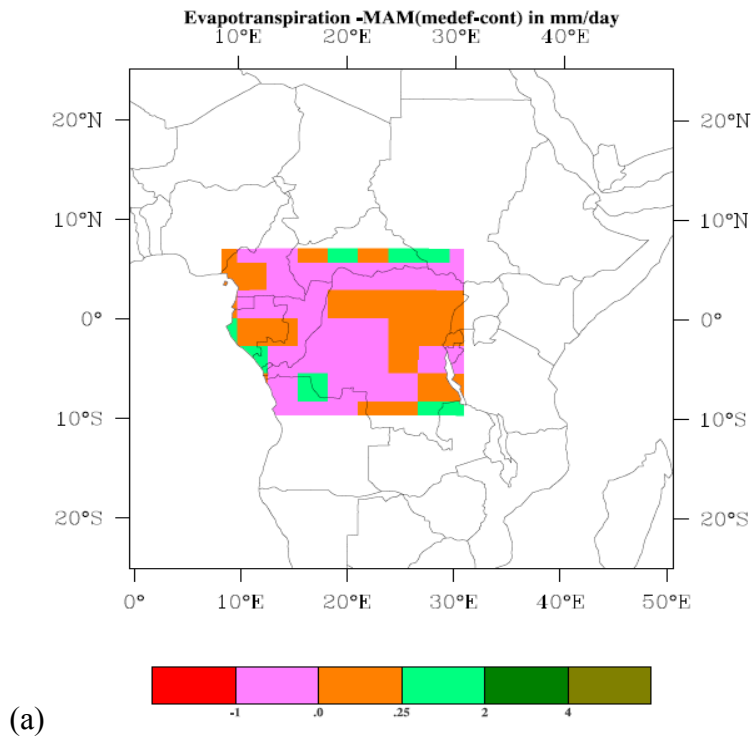


Figure 3.20 Change in evapotranspiration after medium deforestation (a) MAM and (b) JJA

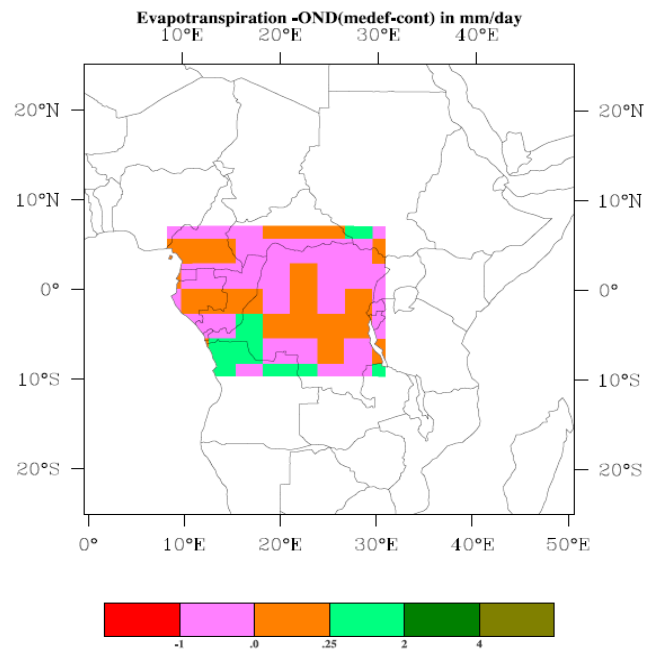


Figure 3.21 Change in evapotranspiration after medium deforestation -OND

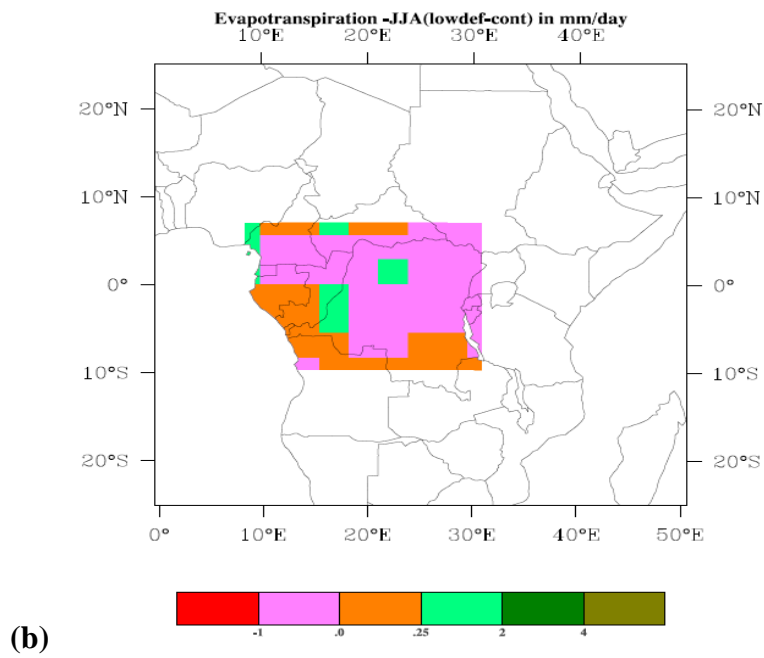
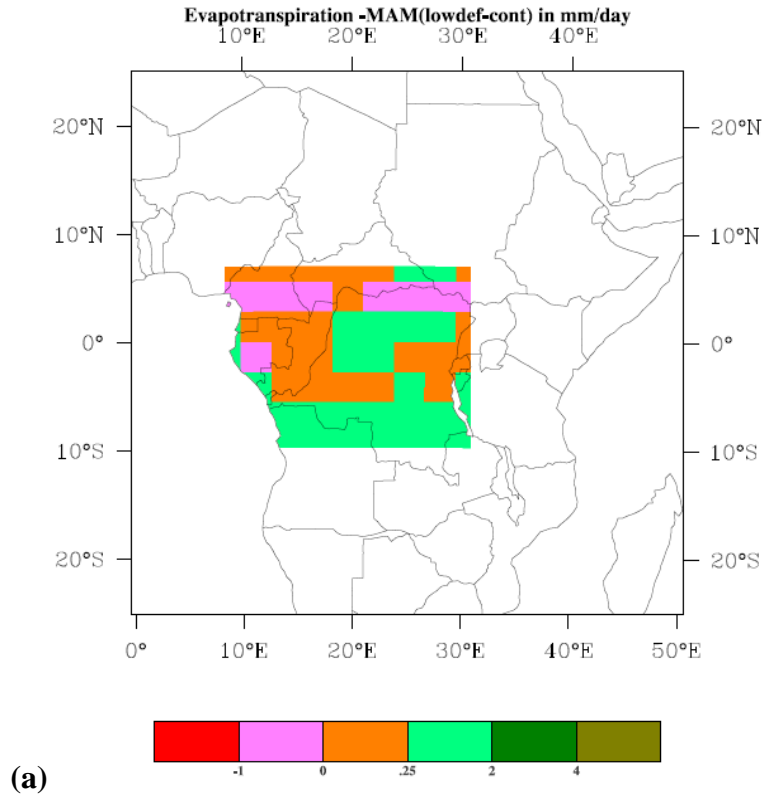


Figure 3.22 Change in evapotranspiration after low deforestation (a) MAM and (b) JJA

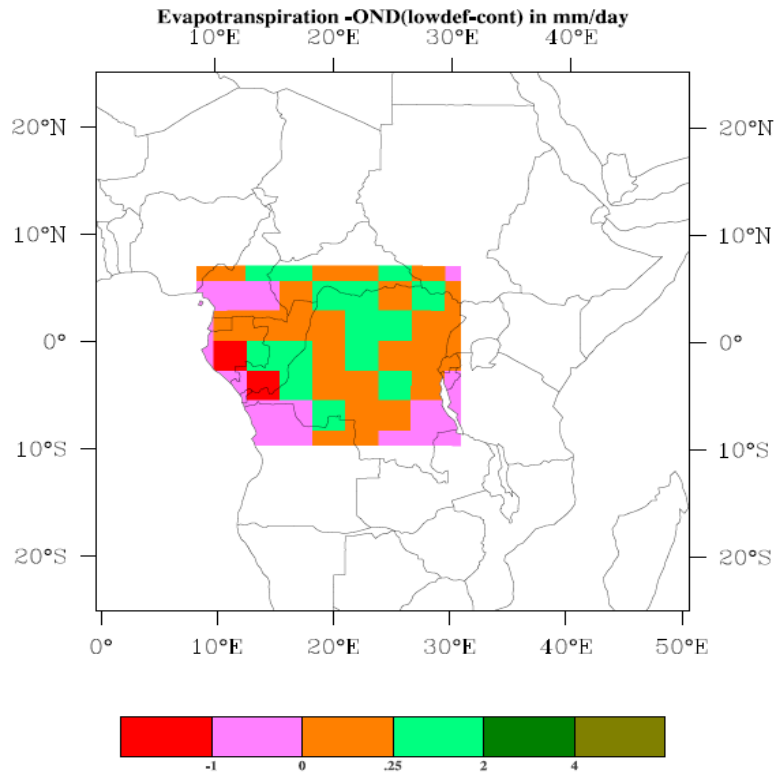


Figure 3.23 Change in evapotranspiration after low deforestation-OND

3.2.3 River Runoff

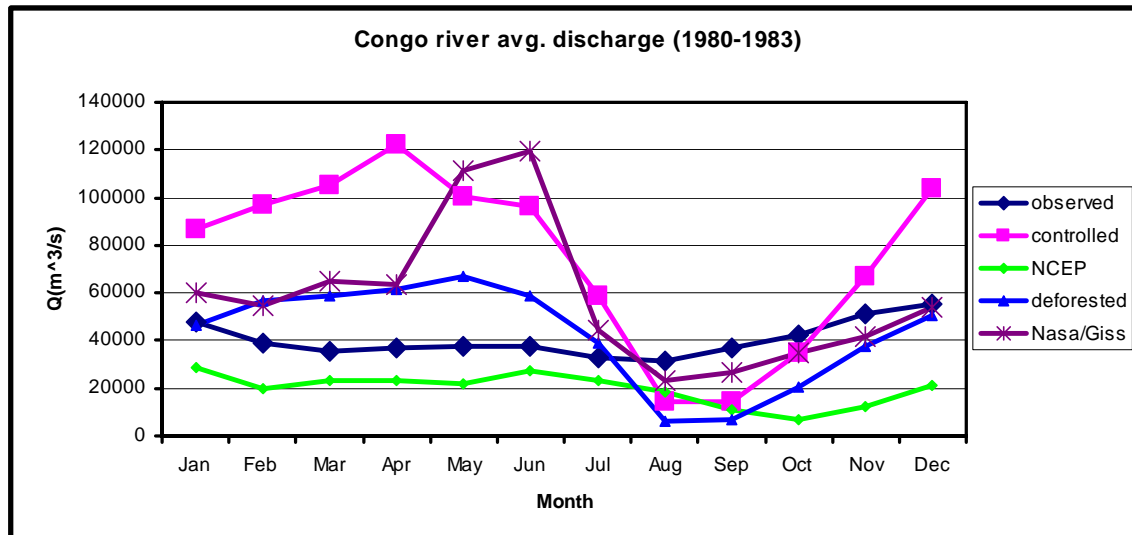


Figure 3.24 Congo River runoff; Observed (IRI); Cam3/Clm3 simulation (control and experiment 1); Clm3 (offline) simulation using NCEP rainfall data and Nasa/Giss simulation

The runoff analysis includes comparison with results from the NASA/GISS model and the use of NCEP re-analysis data (Figure 4.6).

The river Congo runoff at the gauging station located at Kinshasa (4.3° S, 15° E) just before entry into the Atlantic Ocean (see figure 4.1) has been simulated and compared to the observed and other sources of runoff data. The simulated discharge is more than twice the observed values from January to June. From July to October the simulated runoff drops below the observed values but then rises again to almost 3 times the observed by December. There is a noticeable lack of seasonality in the observed data. Experiment 1 (high deforestation) reduces the simulated runoff by about 50% between January and June. Due to the wide discrepancy between the simulated and observed runoff further analysis and sensitivity exercises are discussed in chapter 4.

3.2.4 Temperature

The average monthly values of the reference height (2m) temperatures following the various experiments are as shown in figure 3.25. There is almost a linear relationship between temperature and precipitation (figure 3.7 and figure 3.25) with the low deforestation experiment resulting in the highest values of both temperature and rainfall (for MAM, JJA and OND seasons) while the high deforestation experiment results in the lowest values of the two variables

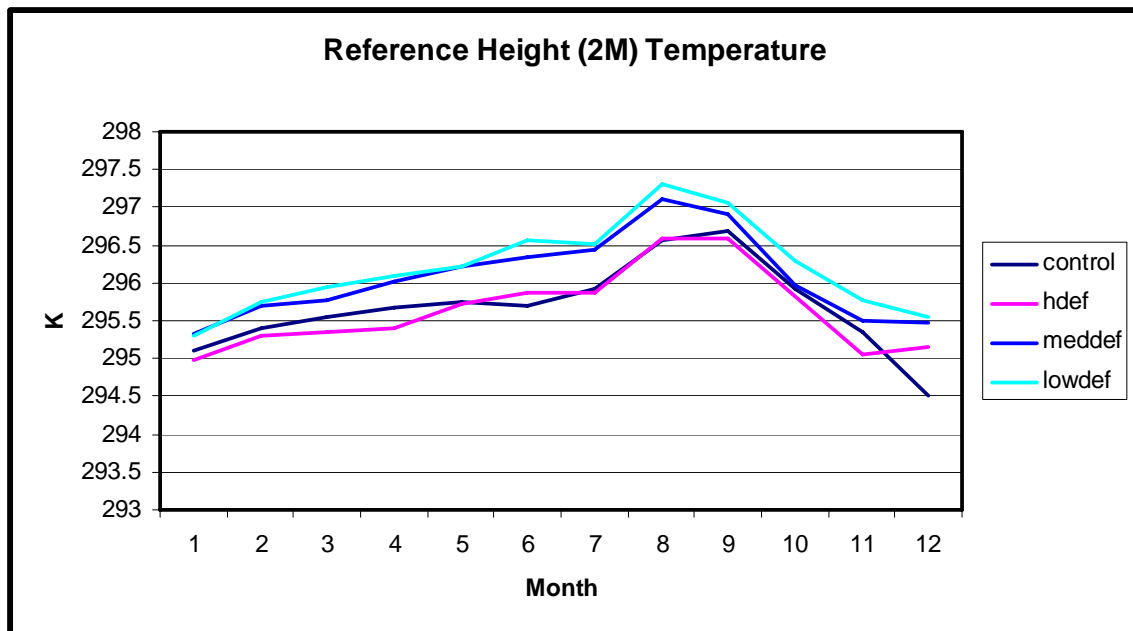


Figure 3.25 The impact of different levels of deforestation on temperature

The increase in temperature associated with low deforestation (experiment 3) is consistent with the corresponding increase in sensible heat flux (figure 3.26). Variations in reference height temperatures are a result of the interplay between changes in both the vegetation albedo and the energy at the surface due to latent cooling. Apparently the decrease in albedo after low deforestation resulted in higher absorption of solar radiation and in the presence of relatively higher moisture from evapotranspiration (compared to other experiments) gave rise to optimal conditions for convective rainfall formation.

On the other hand high deforestation (experiment 1) led to an increase in albedo, less absorption of solar radiation, reduced evapotranspiration and hence reduced convective activity despite the increased energy available from the reduction in latent heat cooling. The influence of albedo on temperature and precipitation is further compounded by the fact that drier soils have higher albedo values, Table 3.2.

Table 3.2 Dry versus wet soil albedo

Color Class	Dry		Saturated	
	vis	nir	vis	nir
1 = light	0.24	0.48	0.12	0.24
2	0.22	0.44	0.11	0.22
3	0.20	0.40	0.10	0.20
4	0.18	0.36	0.09	0.18
5	0.16	0.32	0.08	0.16
6	0.14	0.28	0.07	0.14
7	0.12	0.24	0.06	0.12
8 = dark	0.10	0.20	0.05	0.10

3.2.5 Sensible heat flux

Changes in sensible heat flux are a mirror image of changes in temperature. This is because sensible heat flux tends to increase as a result of increased energy at the surface when there is less moisture (evapotranspiration) and hence reduced latent cooling. Temperature is actually a measure of the sensible heat flux. However, variations in sensible heat flux following the various experiments are limited to a very small range (within 2W/m^2) except for the rainy seasons of MAM and OND. Sensible heat

decreased by an average of 3 W/m^2 in the rainy seasons of MAM and OND following high deforestation (experiment 1) and increased by a similar amount after experiment 3 (low deforestation). The increase (decrease) in sensible heat flux corresponds to the increase (decrease) in precipitation over the basin.

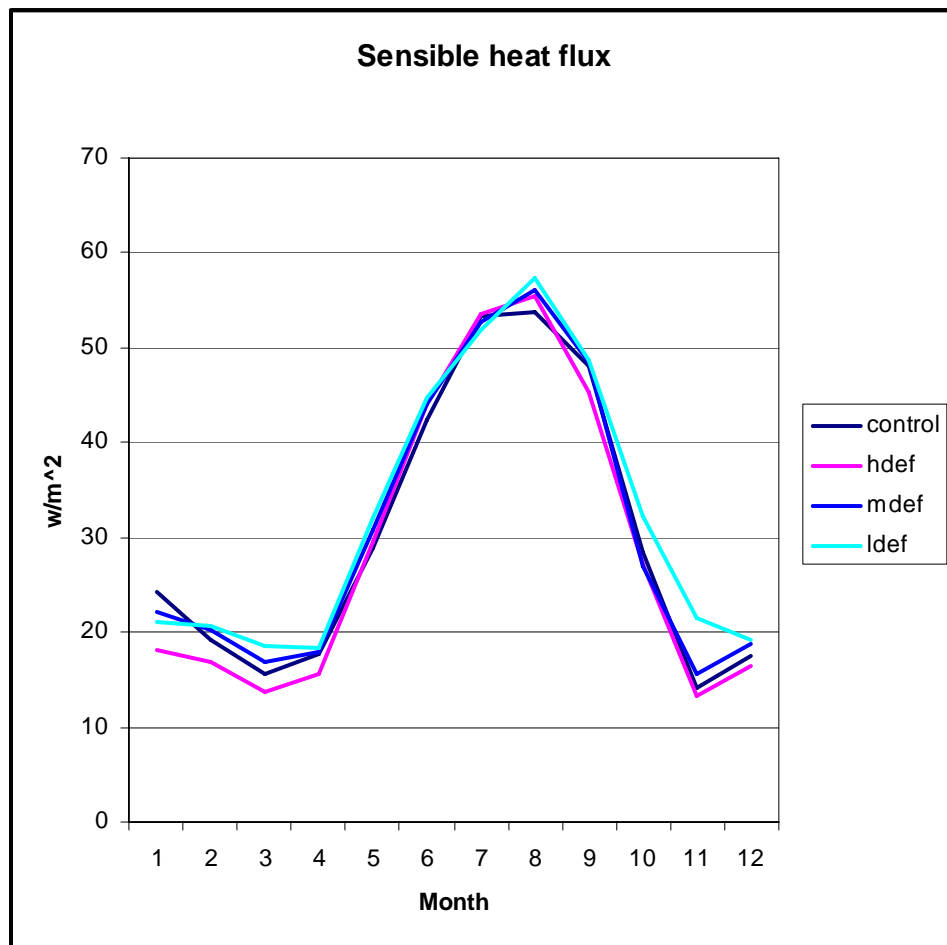


Figure 3.26 The impact of different levels of deforestation on Sensible Heat Flux

3.2.6 Latent heat flux

The most noticeable phenomenon is that enhanced (reduced) latent heat flux corresponds to enhanced (decreased) precipitation (figures 3.7 and figure 3.27). Experiment 1 (high deforestation) results in the lowest values of latent heat flux in the rainy periods of MAM and OND and also in the highest reduction in precipitation during the same periods. The opposite is true for experiment 3 (low deforestation) which resulted in an increase of precipitation.

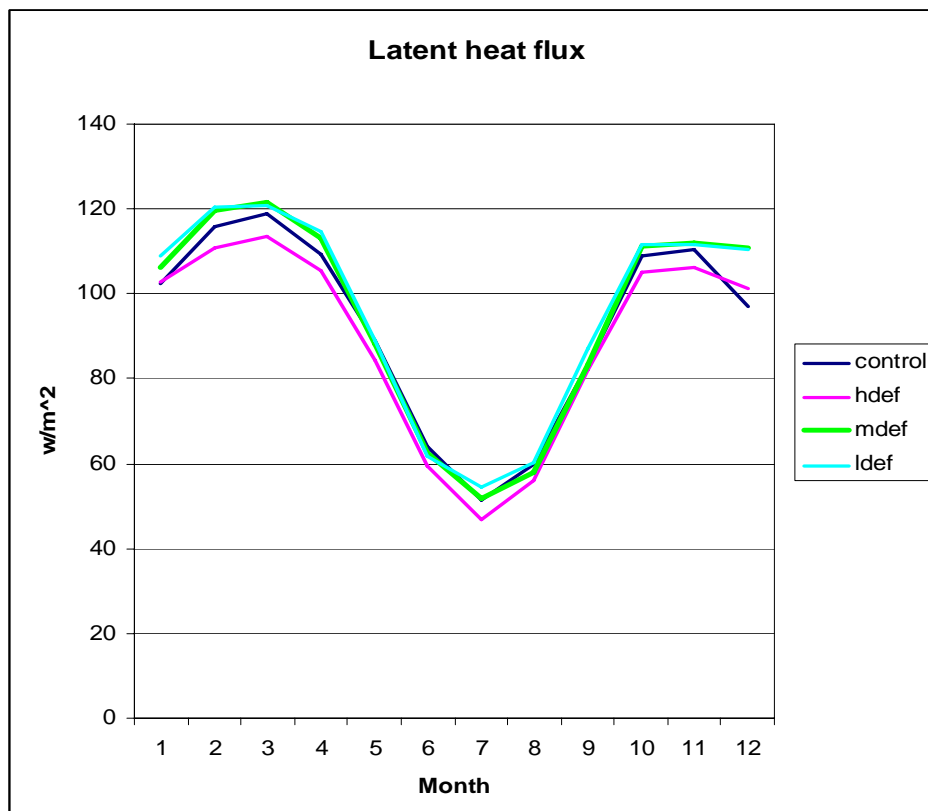


Figure 3.27 The impact of different levels of deforestation on Latent Heat Flux

Through this mechanism vegetation does have a significant moderating effect on precipitation since it influences, via evapotranspiration, the degree of cooling of the surface through enhanced/decreased latent heat fluxes.

The decrease in latent heat flux during MAM and OND for experiment 1 did not give rise to an increase of sensible heat flux as would be expected. A possible explanation is that the increase in albedo following deforestation had a stronger influence on the sensible heat flux than the reduction in latent heat flux did through reduced evapotranspiration.

3.2.7 Soil Water Content

The discretization of the soil column in CLM is as shown in figure 3.28. Soil water output variables e.g. volumetric soil water content (expressed as a fraction), soil liquid (expressed in kg/m^2) are generated for each layer

Volumetric soil water content for the control and experiment 1 results are shown in figure 3.29. The volumetric soil water for the bottom layers (layer 10) has little seasonal change while the surface layer water content varies with the seasons. The bottom soil layer has lower values of volumetric soil water for the control case in comparison to the highly deforested case (experiment 1). The upper soil layers, however, have higher values of volumetric soil water for the control case than the deforested case. The control case has a larger area of forest trees with roots that drain water from deep layers, possibly accounting for the relative dryness of the bottom layers. Closer to the

surface, the density of the root distribution of the residue vegetation is much higher and hence the increased abstraction of the soil water.

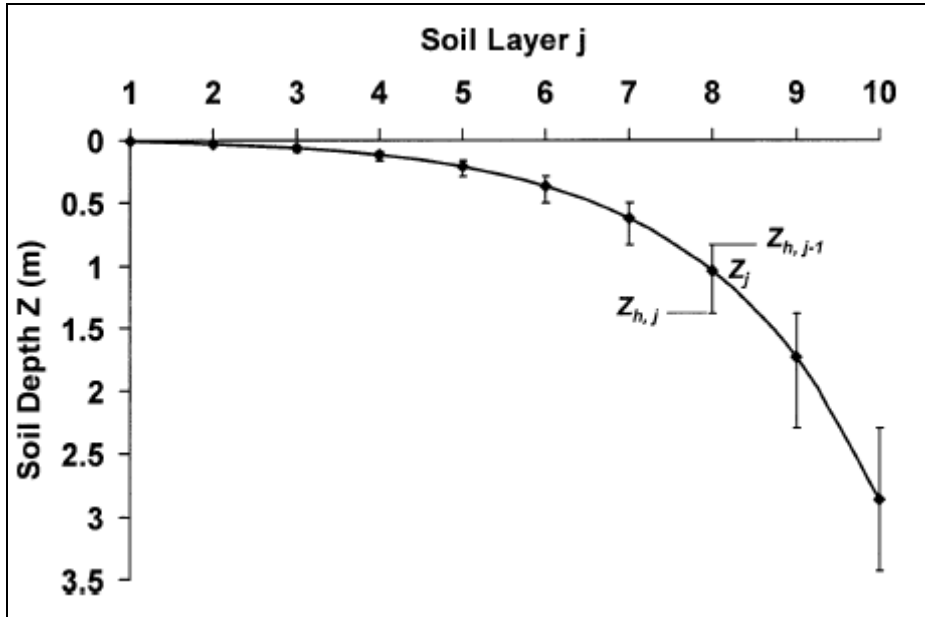


Figure 3.28 discretization of soil column in CLM: Z is the node depth for soil layer j (Wu and Dickinson 2004)

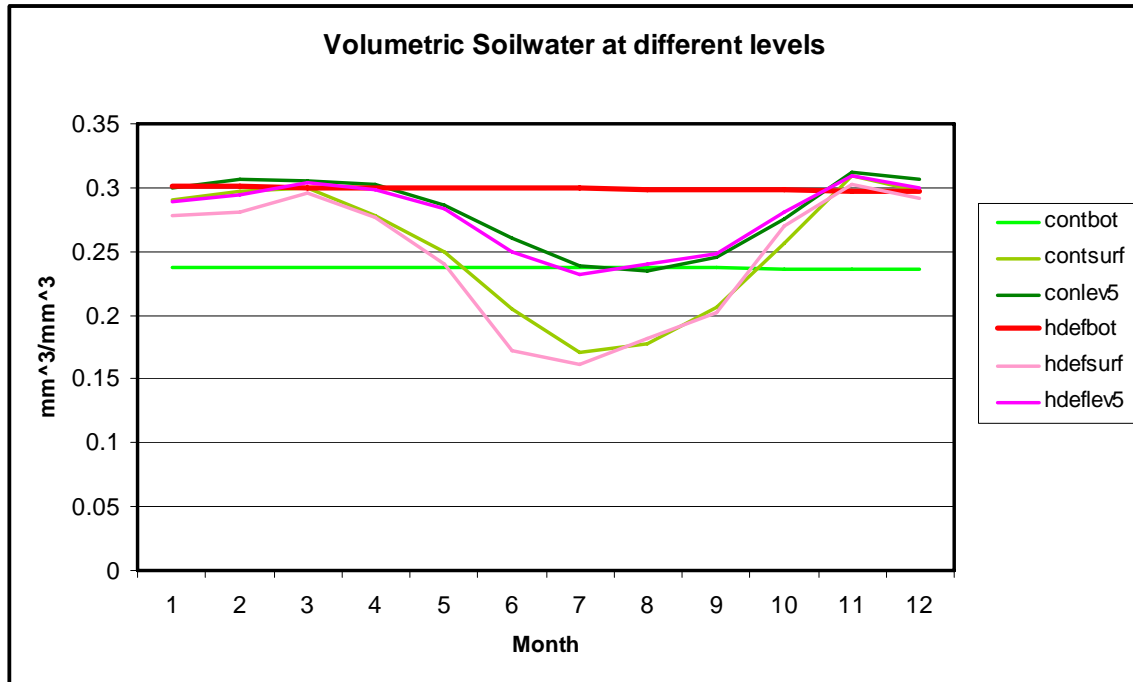


Figure 3.29 Volumetric soil water content for various soil layers after the control and high deforestation experiments.

The soil water content for the other layers tend to cluster together according to their depth from the surface while the bottom layer soil water contents maintain some clear lines of separation (see figure 3.30 below). That is, the soil water content for the bottom layer seems to be less correlated with the water contents for the other soil layers.

Though the low deforestation scenario does not seem to affect the soil water content at the bottom layer significantly, it does allow more moisture transfer from this layer relative to the high deforestation case. Low deforestation therefore seems to have

struck the balance of drawing moisture both from the lower layers and from the surface.
 This could explain the increased evapotranspiration values from this experiment

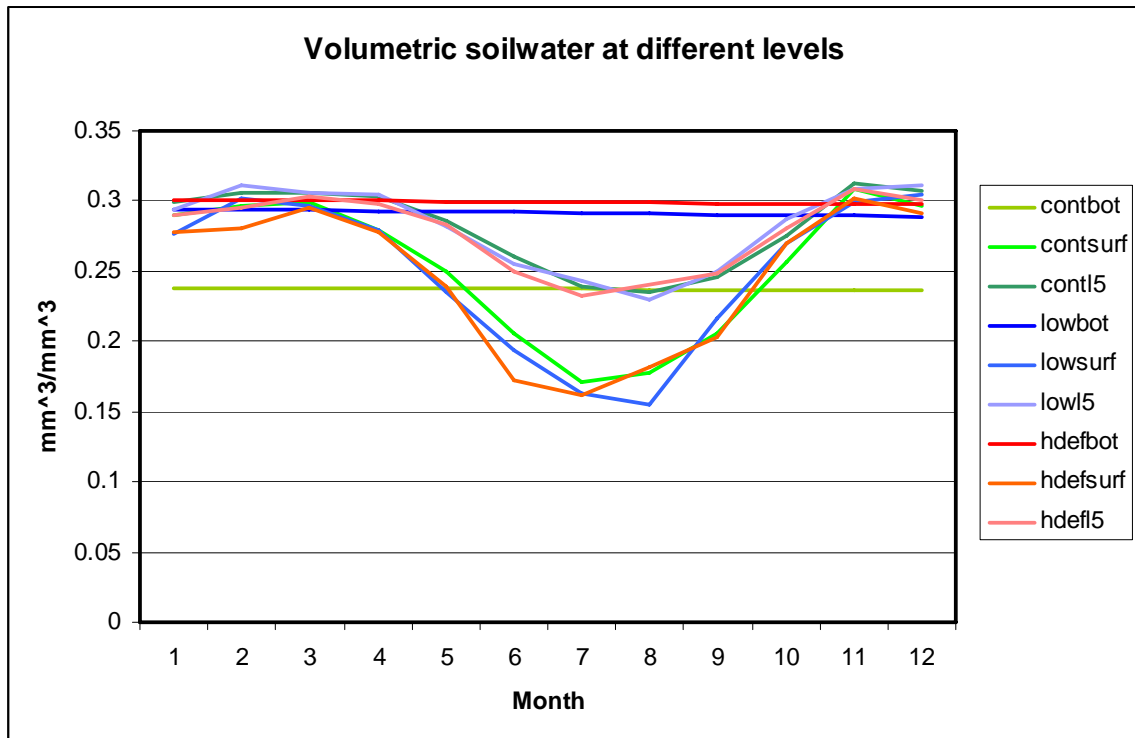


Figure 3.30 Volumetric soil water content for various soil layers after the control, high and low deforestation experiments

The captions contbot, contsurf and contl5 refer to the bottom, surface and layer 5 levels in the control simulation while the corresponding low and high deforestation cases are preceded by the prefixes low and hdef respectively.

3.2.7.1 Correlation between Soil Moisture and Precipitation

An analysis of the correlation between soil moisture and precipitation for the control case and the high deforestation case (experiment 1) indicates higher coherency in the latter (see figure 3.31, figure 3.32 and also figure 3.33 and figure 3.34)

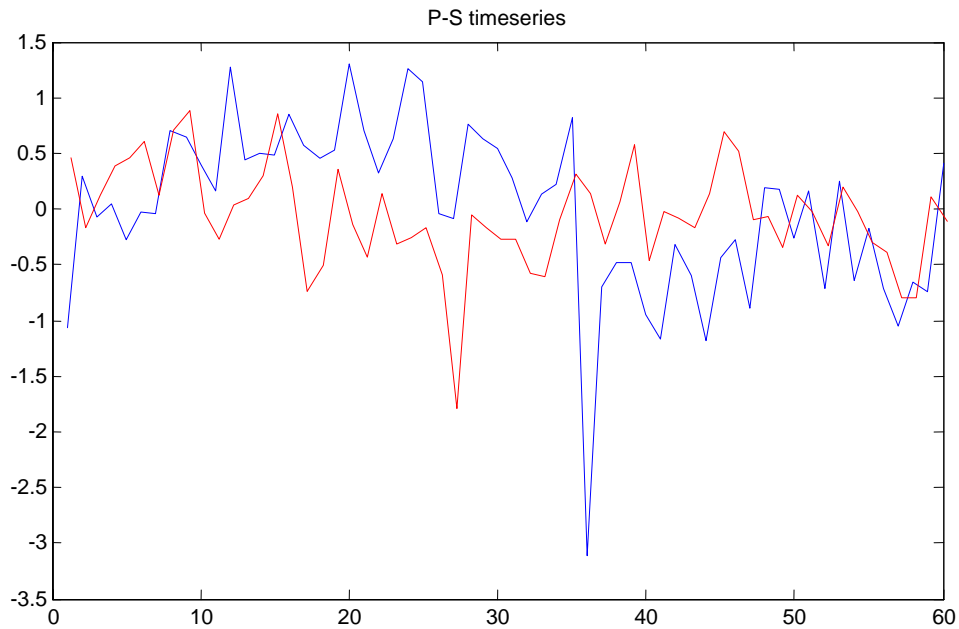


Figure 3.31 Monthly time series of precipitation versus soil liquid in layer 1 - control case –after removing the seasonal cycle.

The red line and the blue line in figure 3.31 and figure 3.32 represent precipitation and volumetric soil water content respectively

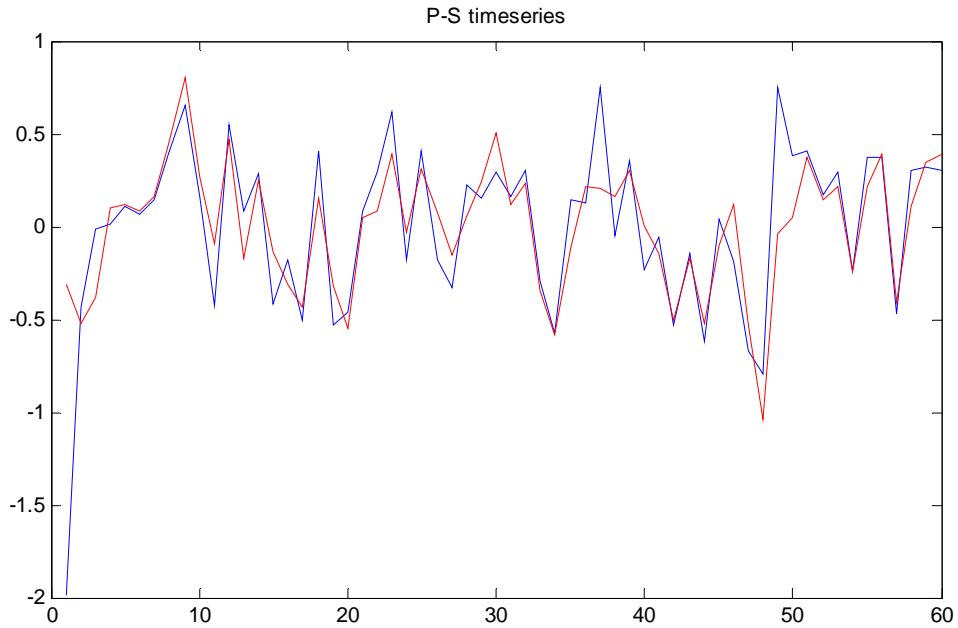


Figure 3.32 Monthly time series of precipitation versus soil liquid in layer 1 –high deforestation case–after removing the seasonal cycle.

The correlation between the two variables i.e., precipitation and upper layer soil liquid, is relatively poorer in comparison to the highly deforested case, especially for cycles longer than 8 months, figure 3.33 and figure 3.34 (coherency plot). The cross-wavelet analysis similarly shows stronger correlation between the two variables over wider amplitude in the deforested case than in the control case, figure 3.33 and figure 3.34 (cross-wavelet). The correlation between the two variables diminishes with soil layer depth.

In these cross-spectral analyses, the horizontal scale represents the data period (time) in months while the vertical scale represents the frequencies in months

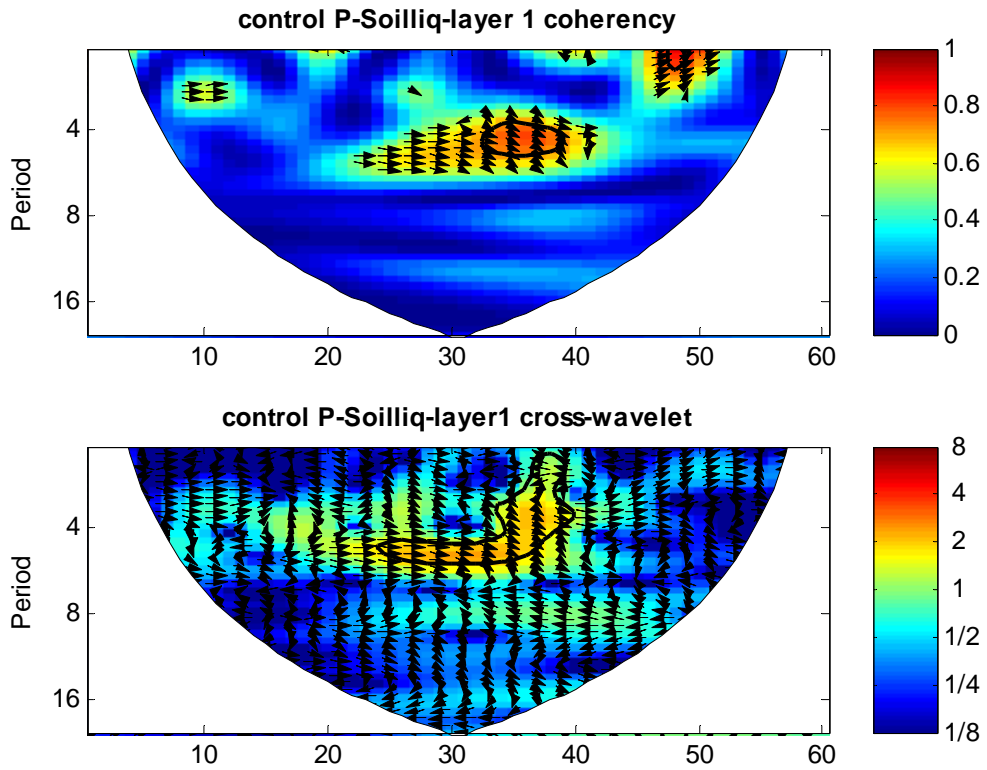


Figure 3.33 Coherency and cross-wavelet between precipitation and soil liquid in layer 1 -control case

The correlation coefficient between precipitation and soil water content for the top soil layer in the control case is mostly less than 0.2 for most of the period except between approximately 25 to 40 months time period. Even for these cycles the correlation coefficient higher than 0.2 is limited to the frequency range of about 5 to 6 months, figure 3.33. The high deforestation case shows a higher correlation between the two variables over a broader range of frequencies and wavelengths, figure 3.34.

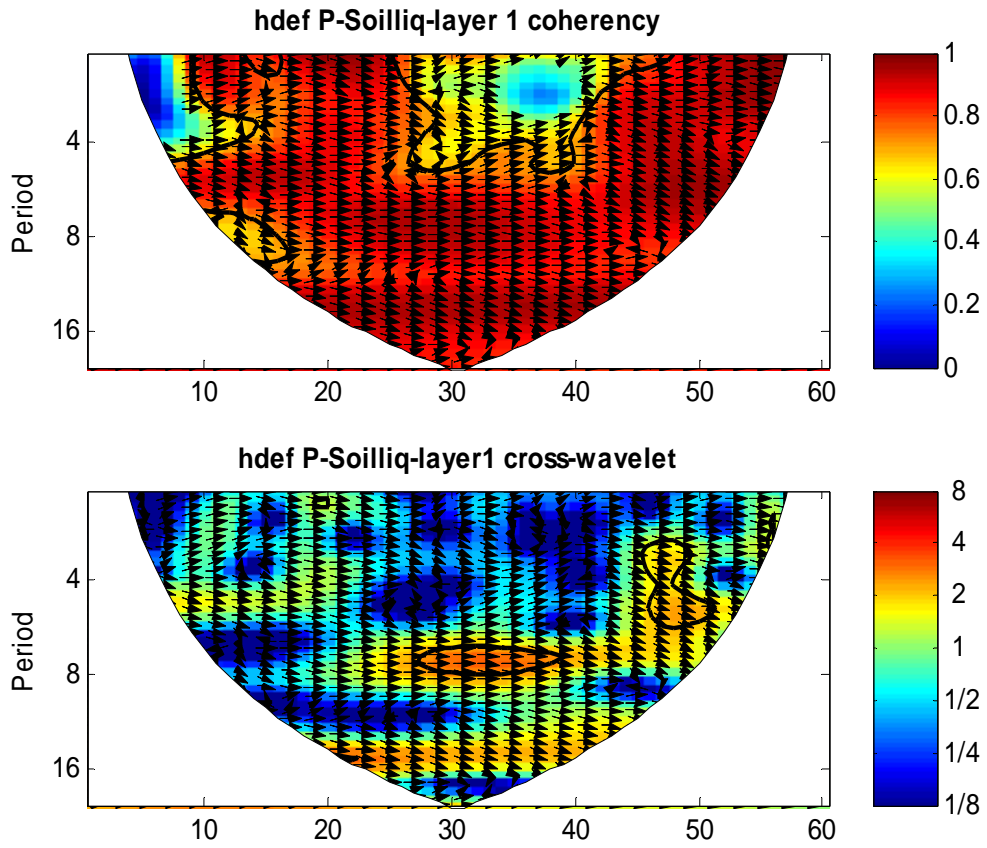


Figure 3.34 Coherency and cross-wavelet between precipitation and soil liquid in layer 1 –high deforestation case

Even in the deforested state, the coherency between soil moisture and precipitation reduces with the layer depth and is not significant after the seventh soil layer, figure 3.35 and figure 3.36 (red line represents precipitation while the blue line represent volumetric soil moisture). This is in good agreement with the findings of Wu and Dickinson (2004) that the correlation coefficients of precipitation and soil moisture at all frequencies for broadleaf tropical forests decreased with depth into the soil.

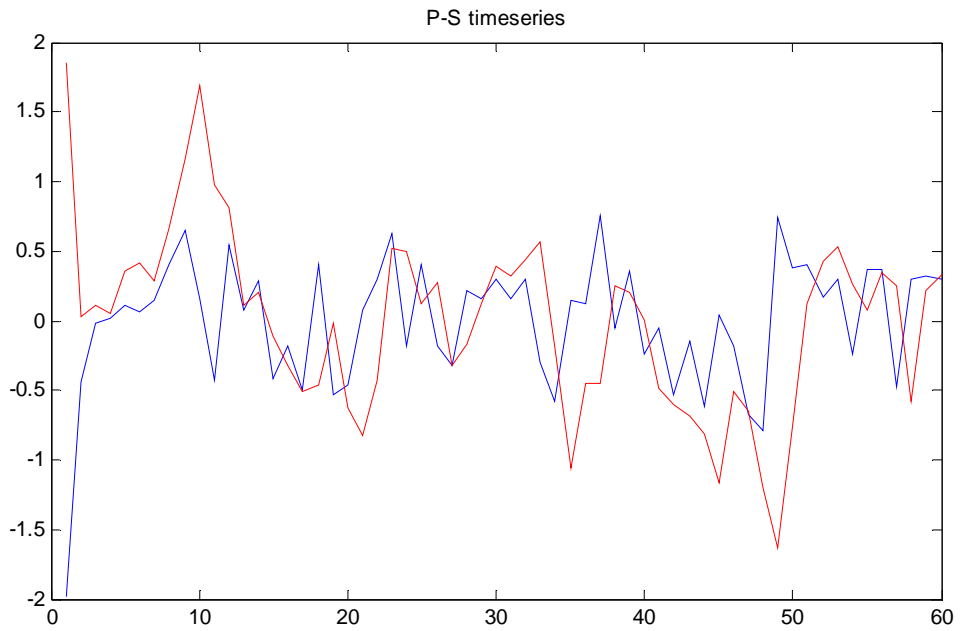


Fig 3.35 Monthly time series of precipitation versus soil liquid in layer 7 – high deforestation case- after removal of the seasonal cycle

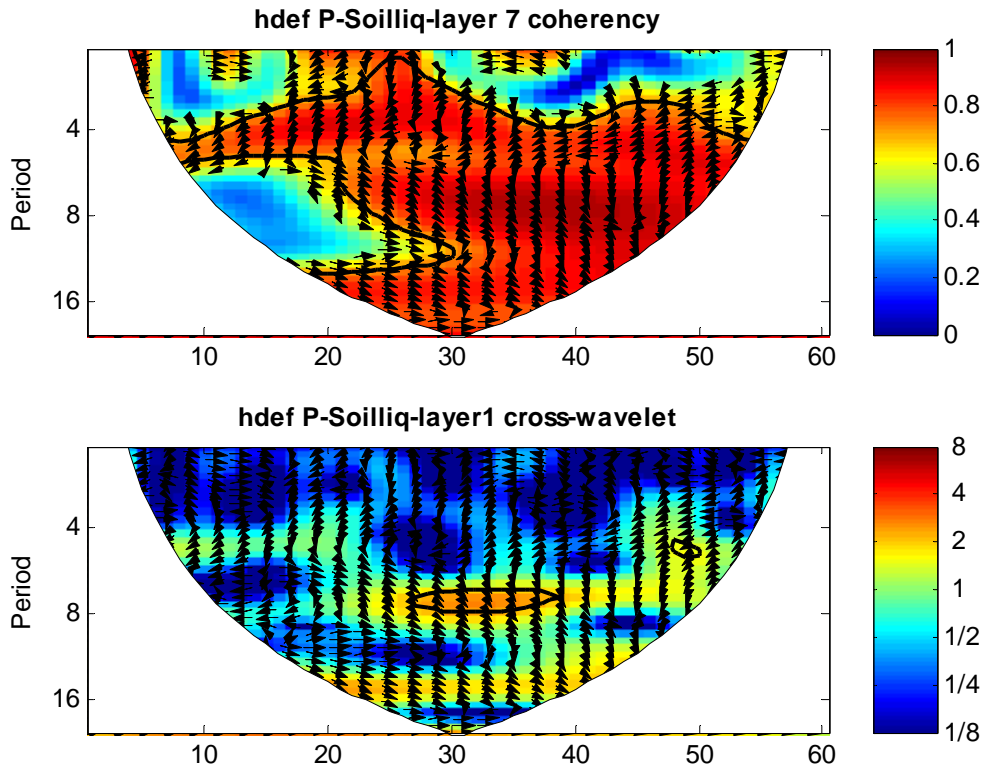


Figure 3.36 Coherency and cross-wavelet between precipitation and soil liquid in layer 7 –high deforestation case

3.3 Conclusions

The parameters that are directly affected by deforestation are albedo (increased/decreased), roughness length (reduced), total soil moisture (reduced) and vegetation cover (LAI-reduced). The decrease in vegetation roughness length results in the reduction of turbulent exchange of energy and thereby reduces the transfer of energy between the surface and the atmosphere. This might explain the reduction of convective activities and hence the fall in mean precipitation values following high deforestation as in experiment 1.

The quantity of moisture in the boundary layer is somewhat dependant on the plant functional type via evapotranspiration. When there is a reduction in the amount of boundary layer moisture, less energy is used for latent heat cooling and there is a tendency for the sensible heat flux to increase. However, the increase in sensible heat flux is also influenced by the absorption of the incoming flux of solar radiation. This absorption is in turn dependant on the albedo of the particular plant functional type. There is therefore a loop of interdependencies among the various parameters like evapotranspiration, albedo, sensible heat flux and latent heat flux..

The impact of deforestation on the volumetric soil water content is consistent with the characteristics of root depth and root water abstraction from the different plant functional types. The bottom layer seems to be the defining level with regard to the impact of deforestation since the water content at this level stands out in the different experiments. There seems to be a level-dependent cluster of soil water contents for the other layers. The low deforestation scenario, which results in the highest precipitation

values, seems to have a better balance in abstracting moisture from the bottom, intermediate and surface layers.

A ranking of the various parameters i.e. precipitation, evapotranspiration, sensible heat flux and latent heat flux shown in table 3.2 indicates the relative impacts on the variables after each experiment. Coherency and cross-wavelet analysis for precipitation and soil moisture shown in figure 3.31—3.32 indicate that various interrelationships can be determined from these rankings.

Table 3.2 Ranking of the key variables and precipitation from the various experiments.

Experiment	PPT (rank)	ETR (rank)	SH (rank)	LH (rank)
control	3	2	3	3
(1) High deforestation	4	4	4	4
(2) Medium deforestation	2	3	2	2
(3) Low deforestation	1	1	1	1

NOTE: PPT- Precipitation ETR- Evapotranspiration SH- Sensible Heat Flux

LH – Latent Heat Flux

CHAPTER 4

SIMULATION OF THE RIVER CONGO RUNOFF

4.1 Water balance for the Congo Basin

The terrestrial water balance is given by the equation

$$S = P - E - R_o - R_s \quad (4.1)$$

where

S= rate of storage of water

P= precipitation rate

E = Evaporation rate (includes evapotranspiration over land and sublimation over snow and ice)

R_o = Surface runoff

R_s = Subterranean runoff

For a large region like the Congo basin the net subterranean runoff is usually small and can be neglected to simplify the equation to the form

$$\{\bar{S}\} = \{\bar{P} - \bar{E}\} - \{\bar{R}_o\}, \quad (4.2)$$

where the parenthesis { } and the bar (̄) indicate the spatial average values of the parameters over the whole region and a time average respectively. Over long periods of

time and in large areas S becomes small in comparison to other terms and hence the equation reduces to

$$\{ \overline{Ro} \} = \{ \overline{P} - \overline{E} \} \quad (4.3)$$

The model results for the right hand parameters of equation 4.3 over the period 1979-1983 are not in exact agreement with the average of the observed values of Ro. (approximately $47 \cdot 10^3$ m³/s and $40 \cdot 10^3$ m³/s respectively) . However, the average value of the model runoff routed via the River Transfer Module is almost twice the observed value i.e. $74 \cdot 10^3$ m³/s. The implication is that the River Transfer module overestimates runoff in this basin.

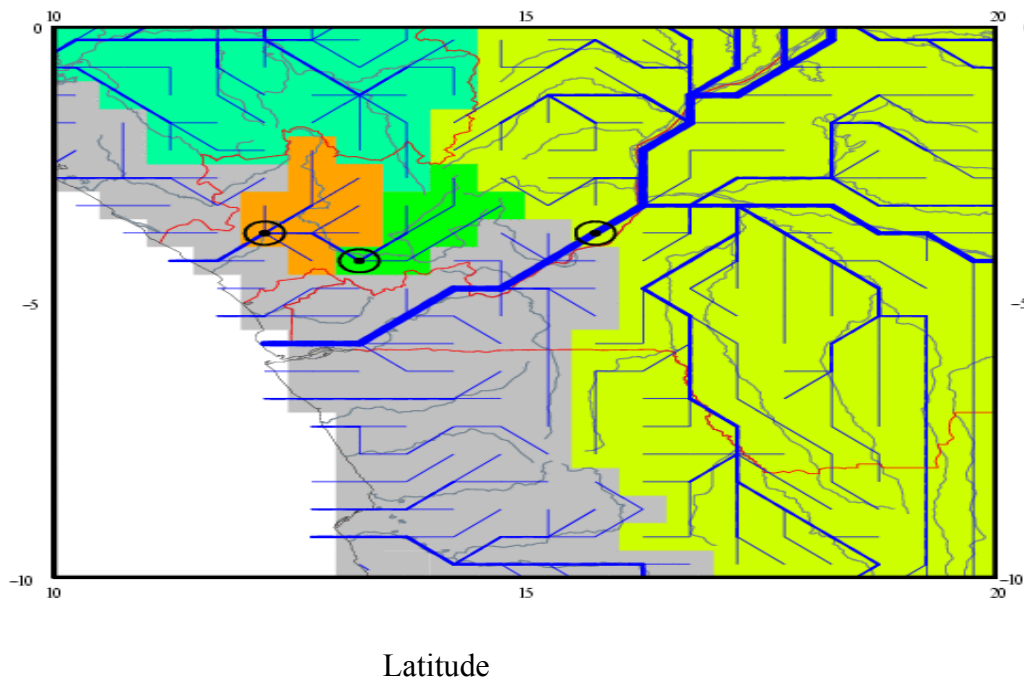


Figure 4.1 Congo River- gauging station located at Kinshasa (4.3^0 S, 15^0 E) - from Global Runoff Data Center.

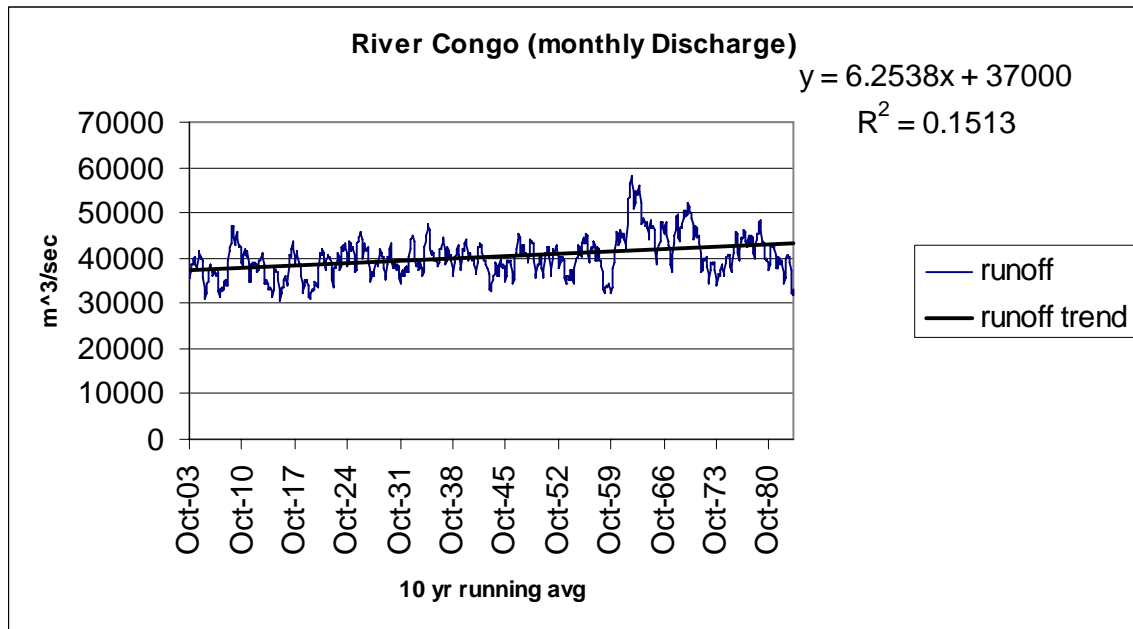


Figure 4.2 River Congo Runoff (observed) at the entry to the Atlantic Ocean –obtained from the International Research Institute (IRI) database

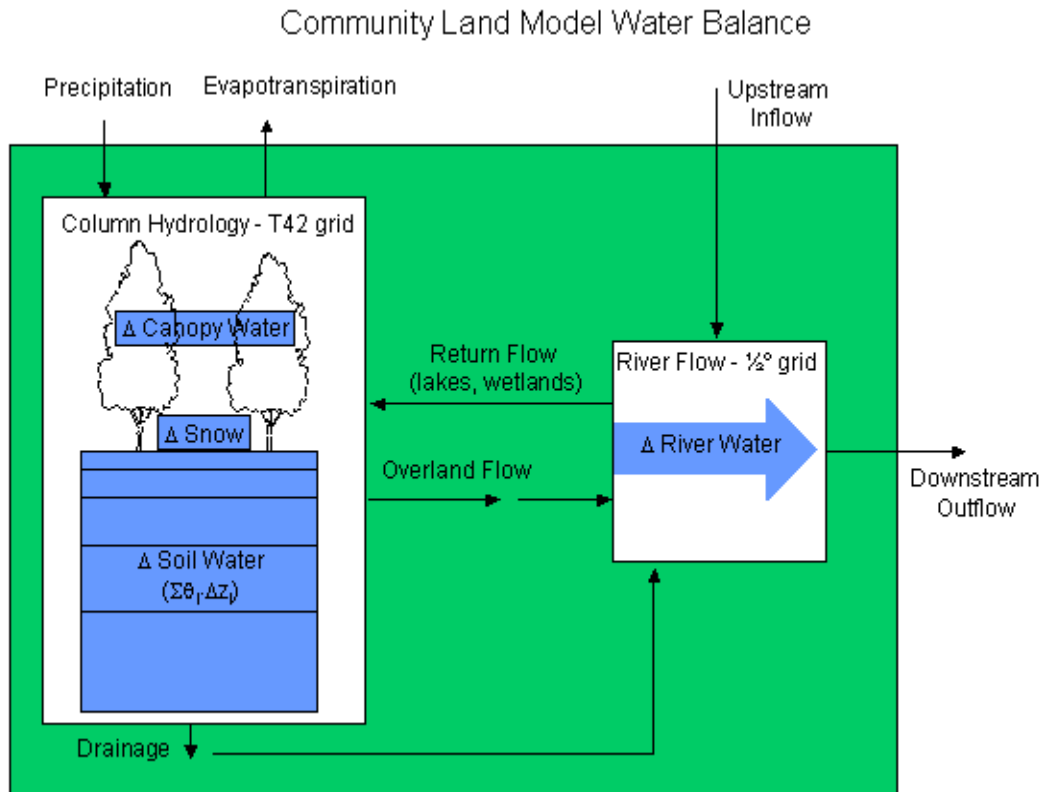


Figure 4.3 Community Land Model Water Balance obtained from <http://www.cgd.ucar.edu/tss/clm/rtn/waterbalance.gif>

4.2 Runoff generation in CLM3

CLM3 uses modified TOPMODEL (Beven and Kirkby, 1979) concepts in the generation of runoff. The original TOPMODEL scheme was formulated to represent hydrological processes at the scale of hill slopes and its implementation in any global circulation model must necessarily come with several compromises. A key feature in the application of the TOPMODEL in CLM3 is the assumption that saturated hydraulic conductivity decays exponentially with depth. The basis for this assumption is that in

many soils the hydraulic conductivity decreases with depth due to compaction while biological activity at the surface leads to the formation of large pores.

Although the assumption of exponential decay of hydraulic conductivity leads to reasonable values of transmissivity in some watersheds, in some regions it can be shown that saturated hydraulic conductivity actually increases or stays constant with depth (Pan et al, 2005) figure 4.4 The exponential decay of the hydraulic conductivity influences the soil moisture conditions and hence the runoff generation and the hydrological cycle and ultimately impacts on the mass and energy fluxes to the atmosphere.

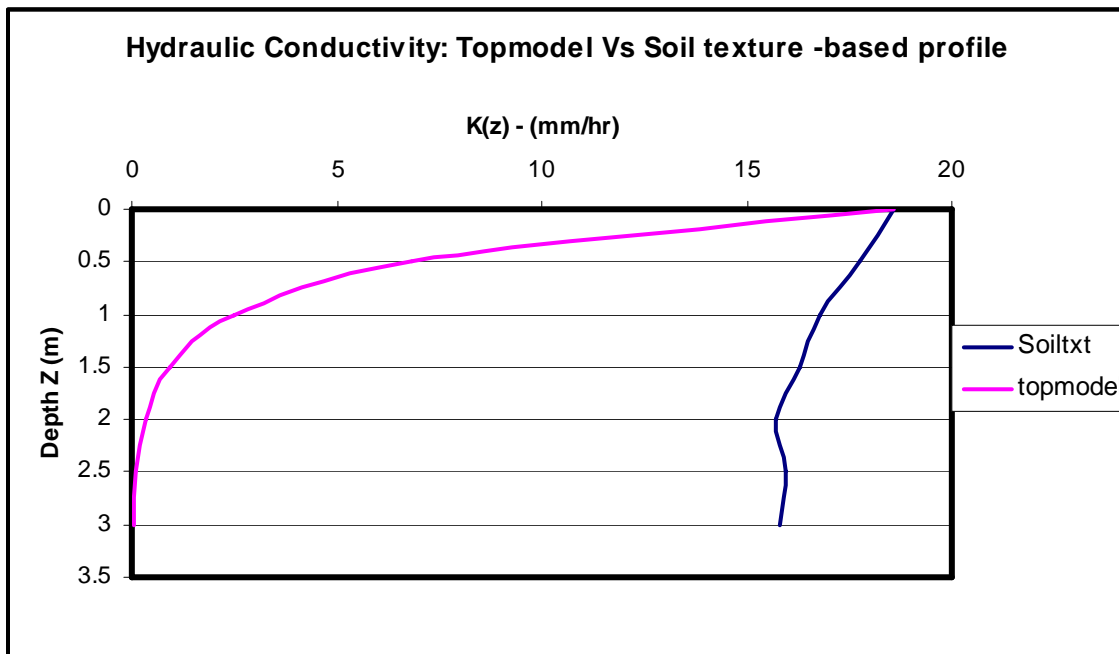


Figure 4.4 The difference between the actual hydraulic conductivity (K_s) profile based on soil texture and the exponential decay profile based on the TOPMODEL

The surface saturated hydraulic conductivity, K_0 , is given in CLM3 as

$$K_0 = 0.007055 * 10^{-0.884 + 0.0153(\% \text{ sand})} \quad (4.4)$$

The above expression is based on the definition on soil hydraulic characteristics by Clapp and Hornberger (1978). CLM3 assumes an exponential decrease of the saturated hydraulic conductivity with depth i.e.

$$K_s(z) = K_0 \exp(-z/z^*) \quad (4.5)$$

where $K_s(z)$ is the saturated hydraulic conductivity at depth z and z^* is the characteristic length scale for the decrease of K_s (z^* is set to 0.5m in the model); z^* is usually written as f in most literature. Table 4.1 shows the various values of f used in most hydrological simulations

Table 4.1 The values of exponential decay factor, f , of the saturated hydraulic conductivity

Authors	sites/regions	f
Beven, 1982	Various sites	-2.35 -9.15
Famiglietti et al., 1992	FIFFE	1.5 -5.17
Stieglitz et al., 1997	Sleepers River	3.26
Dai et al., 2002	Global	2.0
Chen and Kumar, 2001	North America	1.8
Yang et al., 2000	Red Arkansas River	8.0

A grid box in the atmospheric model is divided into saturated and unsaturated zones. The saturated zone also known as the partial contributing area is parameterized as

$$F_{\text{sat}} = W_{\text{fact}} \exp(-z_w) \quad (4.6)$$

where W_{fact} is a parameter determined by the distribution of the topographic index (W_{fact} is set to 0.3 in CLM3), z_w is the mean water table depth.

Surface runoff R_s and base flow R_b are computed for saturated and unsaturated regions separately according to

$$R_s = (1-f_{\text{sat}})R_{s,1} + (f_{\text{sat}})R_{s,2} \quad (4.7)$$

$$R_b = (1-f_{\text{sat}})R_{b,1} + (f_{\text{sat}})R_{b,2} \quad (4.8)$$

and $R_{s,1} = W_s * 4 * G_w \quad (4.9)$

$$R_{s,2} = G_w \quad (4.10)$$

$$R_{b,1} = K_D * W_b (2B+3) \quad (4.11)$$

$$R_{b,2} = I_b \exp(-z_w) \quad (4.12)$$

where G_w is effective rainfall i.e. through fall plus drip from the canopy, W_s is the soil layer thickness weighted soil wetness in the top three layers, W_b is the soil layer thickness and hydraulic conductivity weighted soil wetness in the bottom five layers. K_D is the saturated hydraulic conductivity for the bottom layers contributing to the base flow. I_b is a base flow parameter for the saturated fraction of the grid and may be estimated from soil and topographic features.

Runoff simulations using the coupled Cam3/Clm3 models for the station shown in Figure 4.1 are as plotted in Figure 4.5

The River Transfer Module (RTM) highly over estimates the discharge (almost 3 times in the worst cases) during the rainfall months of March-May (MAM) and almost doubles the discharge during the other rainfall period of OND. It underestimates the runoff during the drier months of JJA. Considering its size as the second largest river in the world (after Amazon) in terms of water yield it is important that the rate of its freshwater discharge into the Ocean be correctly modeled if its impact on the coastal ocean water properties e.g. salinity, temperature, density etc and hence on the local ocean-land -atmosphere interactions is to be correctly determined. Errors in the calculation of freshwater inflows into the ocean are subsequently transferred to other parameters through the ocean module coupling.

One of the likely causes of poor simulation of the Congo River runoff is the determination of the saturated zone also known as the partial contributing area. In the topmodel concept this area is given by

$$F_{sat} = \int_{\lambda \geq (\bar{\lambda} + fz\Delta)} pdf(\lambda) d\lambda \quad (4.13)$$

where $\lambda = \ln(a / \tan \beta)$ is the topographic index, a is the contributing area and $\tan \beta$ is the local slope. $\bar{\lambda}$ is the mean value of λ in the grid cell, $pdf(\lambda)$ is the probability density function of λ and $z\Delta$ is the grid-mean water table depth. The CLM3 parameterized the partial contributing area based on the hypothesis of Stieglitz et al. (1997) as

$$f_{sat} = W_{fact} \exp(-Zw) \quad (4.14)$$

Where W_{fact} is a parameter determined by the distribution of the topographic index and Zw is the mean water table depth given by equation 4.15. In an ideal situation these parameters should be estimated from the topographic characteristics of the basin. However due to lack of high resolution topographic data some empirical estimates have been used such as setting $W_{fact} = 0.3$ in CLM3. Zw is formulated as

$$Z_w = f_z (Z_{bot} - \sum S_j \Delta Z_j) \quad (4.15)$$

where f_z is a water table depth scale parameter, Z_{bot} is the bottom depth of the lowest soil layer, S_j is soil wetness at layer j and ΔZ_j is the soil layer thickness at layer j . In CLM3 f_z is given the value $1m^{-1}$.

4.3 Congo River Runoff using NCEP Re-analysis data

An offline run of CLM3 using the NCEP-reanalysis precipitation data significantly reduces the Congo River runoff as can be seen in figure 3.24 (green curve). It also reduces the exaggeration of the seasonal variability of runoff which is persistent in the coupled CLM3 runs

However, the National Center for Environmental Prediction (NCEP) re-analysis precipitation data is significantly different from both the observed (TRMM) and the

model generated data (figure 4.6). Except for the month of February, the NCEP data is more than 1 standard-deviation below the observed data provided by Sharon Nicholson. The NCEP data indicates a longer period of rainfall below the 4mm/day level, i.e. from April to November. The NCEP February rainfall peak of 10 mm/day is much higher than the MAM peaks (about 7 mm/day) of CAM3 and the observed MAM rainfall which peaks at about 6 mm/day

The very low seasonal variability of runoff in the Congo River in the observed data is uncommon when compared to other river basins. The Amazon River figure 4.5 shows a noticeable seasonality in runoff in contrast to the Congo. However the simulated runoff in both rivers is markedly different from the observed.

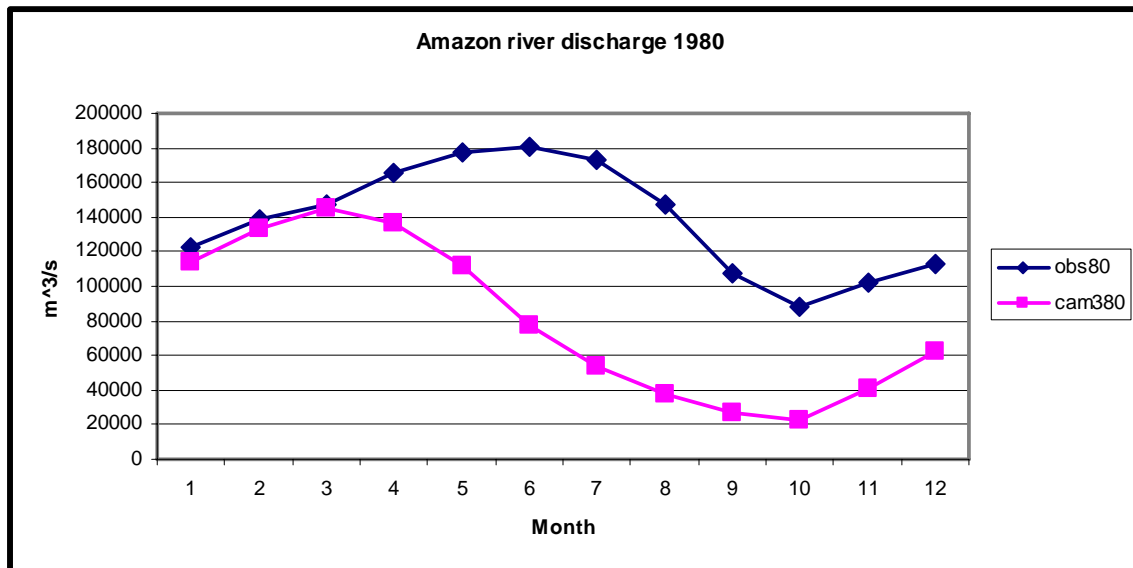


Figure 4.5 Monthly hydrograph for the Amazon River, 1980; observed versus simulated

The NCEP re-analysis data is significantly different from both the observed and simulated rainfall, figure 4.7. Even though the improvement in the Congo runoff simulation following the use of the NCEP re-analysis gives evidence of the effect of simulated rainfall on the runoff production it does not preclude other sources of error in runoff generation such as the runoff parameterization scheme, river routing module, soil moisture and soil texture data.

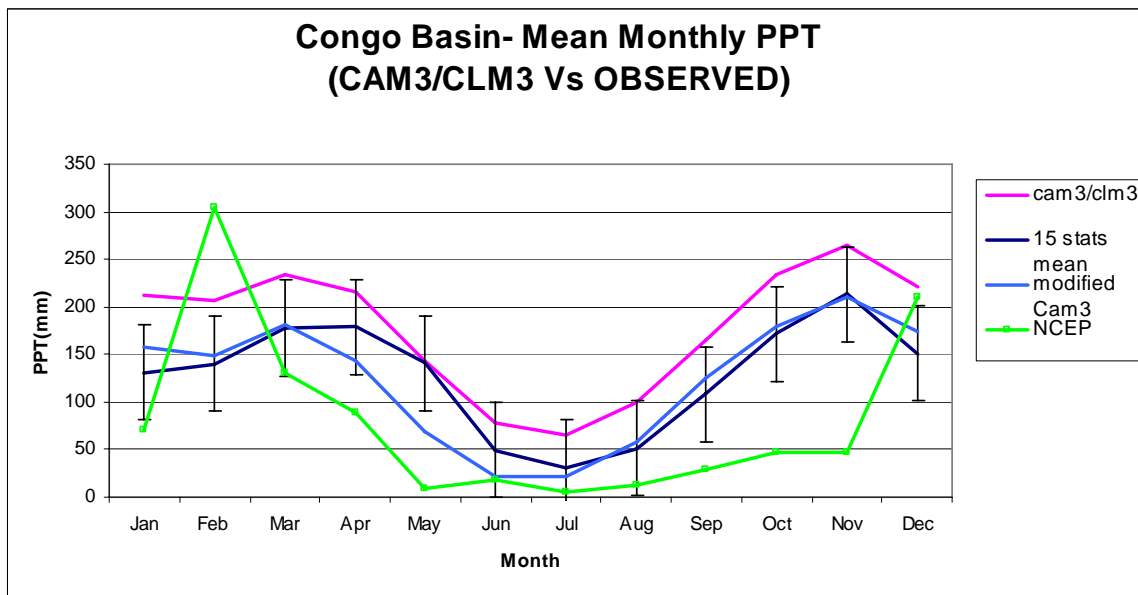


Figure 4.6 Comparison of NCEP-reanalysis rainfall data, observed and CAM3 (model) simulated rainfall.

4.4 Impact of top soil layers and deforestation on runoff simulation

Soil wetness is weighted by the soil thickness of the top three layers in the calculation of surface runoff in the drier portion of the grid, equation 4.7. Variation of the number of soil layers considered as top layers from 3 to 5 showed little impact on runoff generation in comparison to the impact of high deforestation.

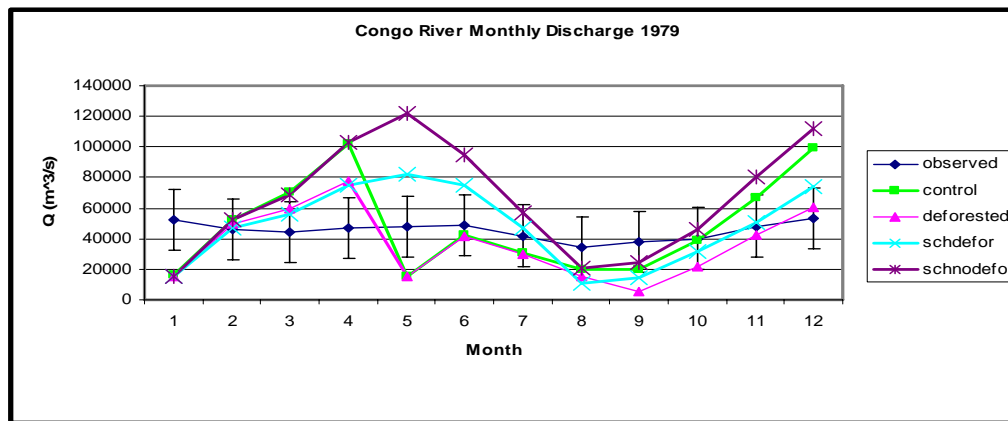


Figure 4.7 Congo River Runoff after various changes in soil hydraulic properties -1979

‘Schdefor’ refers to changes in soil parameters after deforestation while ‘schnodefor’ refers to changes in soil parameter but no deforestation. The first year (1979) run (figure 4.7) is unstable as the model soil moisture is yet to reach equilibrium with the surface and subsurface water fluxes. This period is therefore not considered further in the analysis. The following year’s (1980) runoff results indicate the model is not as sensitive to changes in top soil layer thickness/wetness in comparison to change in rainfall forcing

resulting from deforestation. The runoff is reduced by about 30% after high deforestation but the results for soil layer changes are mixed and insignificant.

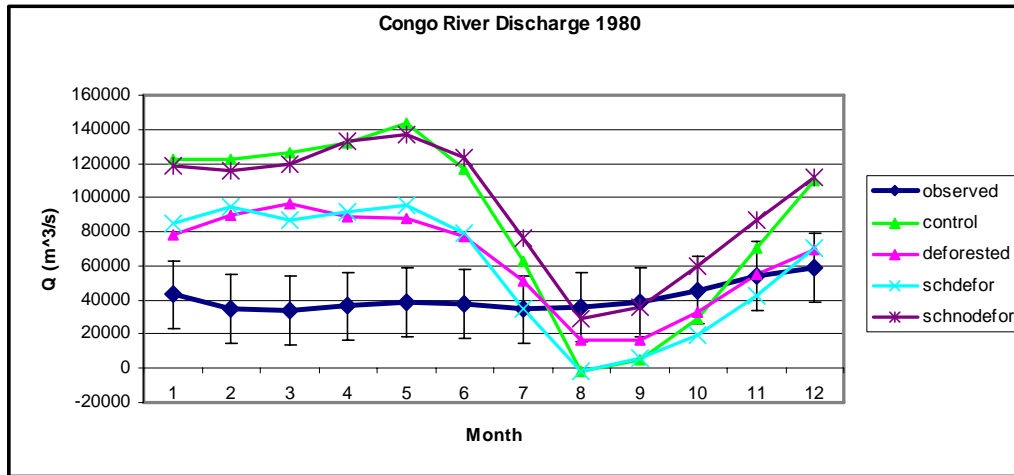


Figure 4.8 Congo River Runoff after various changes in soil hydraulic properties -1980

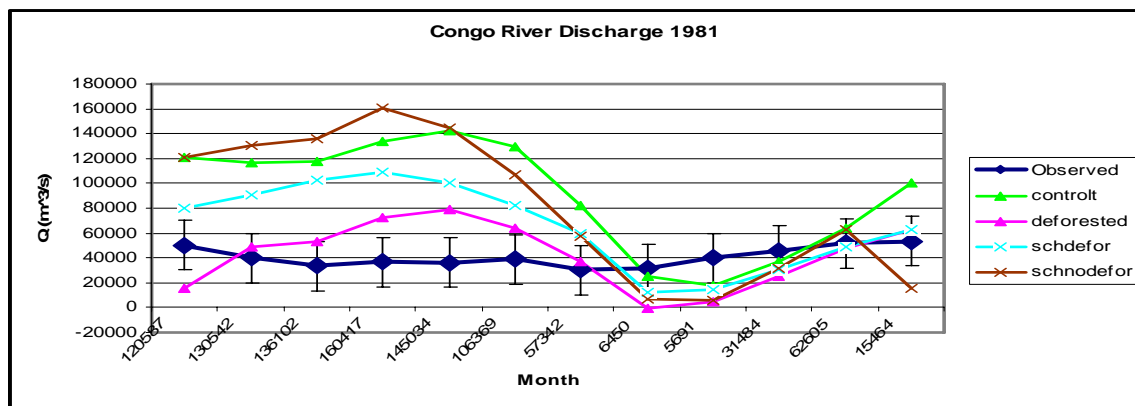


Figure 4.9 Congo River Runoff after various changes in soil hydraulic properties –1981

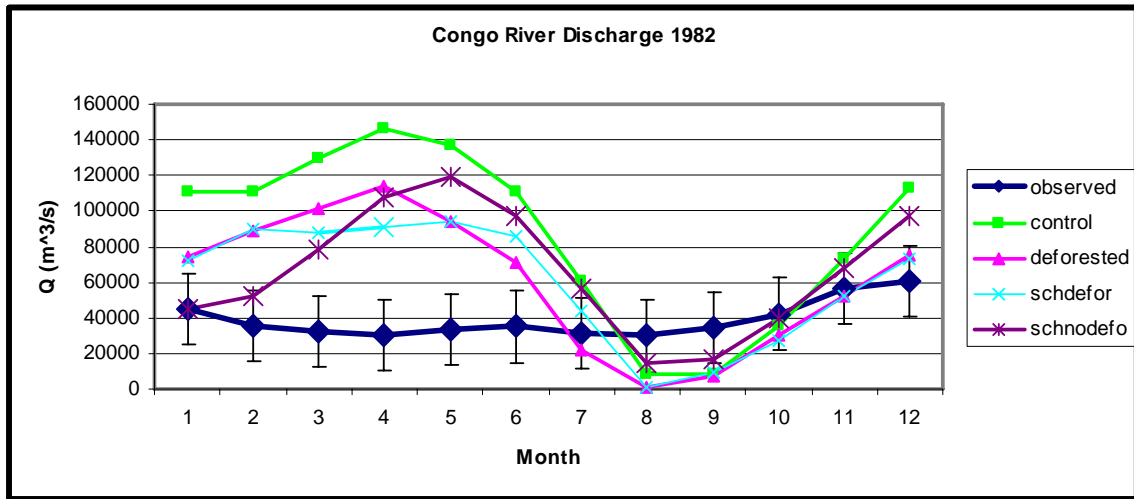


Figure 4.10 Congo River Runoff after various changes in soil hydraulic properties –1982

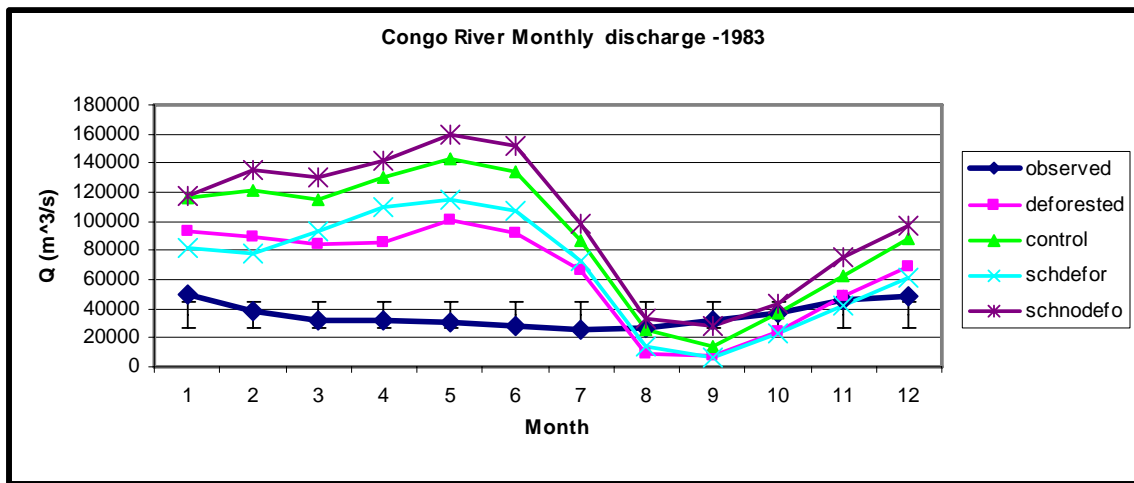


Figure 4.11 Congo River Runoff after various changes in soil hydraulic properties -1983

4.5 Impact of saturated hydraulic conductivity ‘KD’ on Runoff simulation

Proper estimation of both $1b$ and KD , in equations 4.11 and 4.12, can only be achieved via high-resolution topography data which is not yet available in most GCMs including CCSM3. Figure 4.12 shows (1979-1983) the simulated Congo River runoff when the value of KD was altered from the original value of 0.04mm/s to higher and lower (one to two orders) magnitudes. The rationale for this adjustment is that the exponential decay of the soil saturated hydraulic conductivity tends to shut down the drainage and the diffusion processes in the lower layer and hence contributing to reduced base flow and increased surface runoff. Such a formulation contributes to high variability of runoff in correlation with rainfall rather than the more stable situation where base flow plays a more significant role.

Currently runoff is computed as the sum of surface and subsurface flow. The surface and subsurface runoff are computed as given in equations 4.7 and 4.8 respectively. This formulation results in the overestimation of total runoff as shown in the control runs of figures 4.7 through to figure 4.11.

Changes in the tuning parameter KD yielded significant changes in the quantity of runoff during the rainy period of MAM but did not alter the shape of the runoff hydrograph. The water balance between precipitation, evapotranspiration and runoff could no longer hold when KD and $1b$ of equations 4.11 and 4.12 were altered simultaneously.

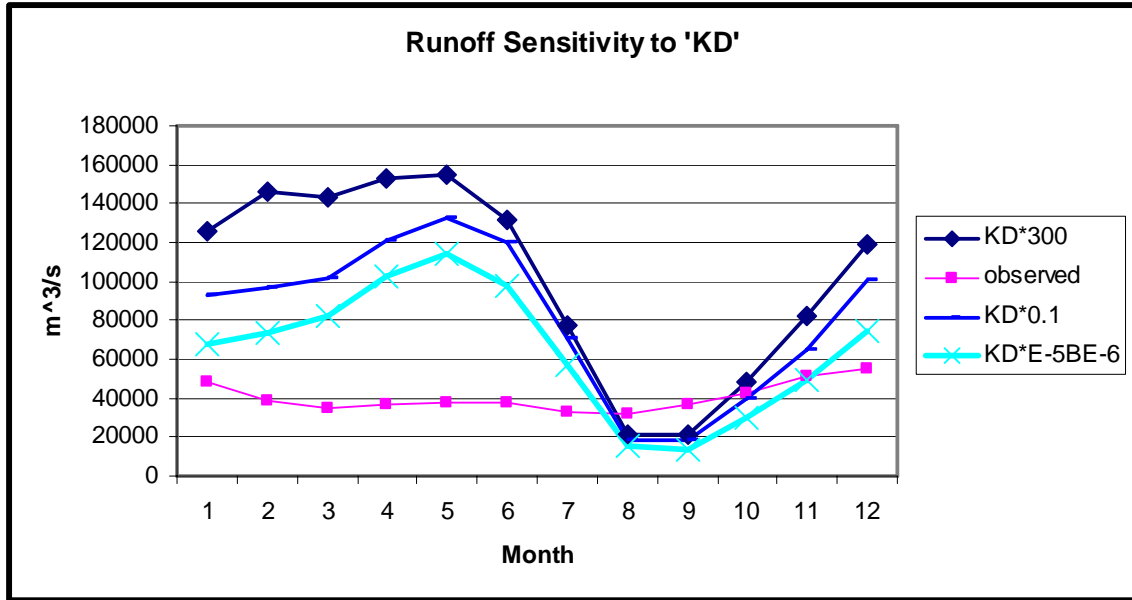


Figure 4.12 Impact of saturated hydraulic conductivity on Congo River runoff.

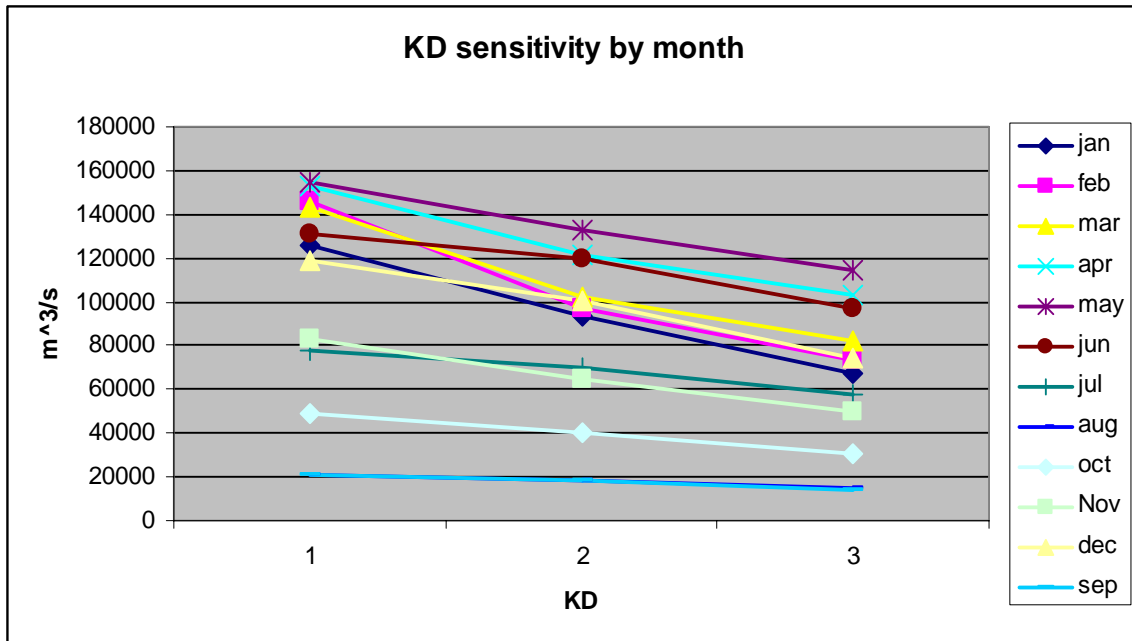


Figure 4.13 'KD' sensitivity on a monthly basis

4.6 Improved runoff simulation scheme

Uncertainties in several variables including rainfall input, runoff parameterization, coupling between surface and atmospheric energy fluxes, quality of observed data makes fine tuning the runoff scheme almost an intractable problem. However, runoff simulation using the NCEP-reanalysis rainfall data points to rainfall input as the single most important variable in the effort to correctly simulate runoff. The original formulation of runoff in CLM3 did not consider the loss in the recharge rate at the soil surface due to loss from ground evaporation.

In this study the rainfall input from CAM3 was iteratively reduced in the formulation of the surface runoff while at the same time reducing the contribution from the dry portion of the basin to the subsurface runoff. The reduction in the recharge (net rainfall) rate was obtained by subtracting ground evaporation, G_e , from the initial input, G_w (equation 4.19 below). This combination had the optimal influence in bringing the simulated runoff closer to the observed values, figure 4.14. The runoff generation equation was therefore reduced to

$$R_s = (1-f_{sat})R_{s,1new} + (f_{sat})R_{s,2new} \quad (4.16)$$

$$R_b = (1-f_{sat}) R_{b,1} + (f_{sat})R_{b,2} \quad (4.17)$$

where $R_{s,1new} = W_s * 4 * G_w * 0.1$ (4.18)

$$R_{s,2new} = G_w - G_e \quad (4.19)$$

$$R_{b,1new} = K_D * 0.1 * W_b(2B+3) \quad (4.20)$$

$$R_{b,2} = 1b \exp(-zw) \quad (4.21)$$

The improved simulation, however, was obtained at the expense of mass balance of water in the various stages of precipitation, evaporation and soil moisture. The loss of water in this case can only be accounted for as deep groundwater (aquifer) recharge.

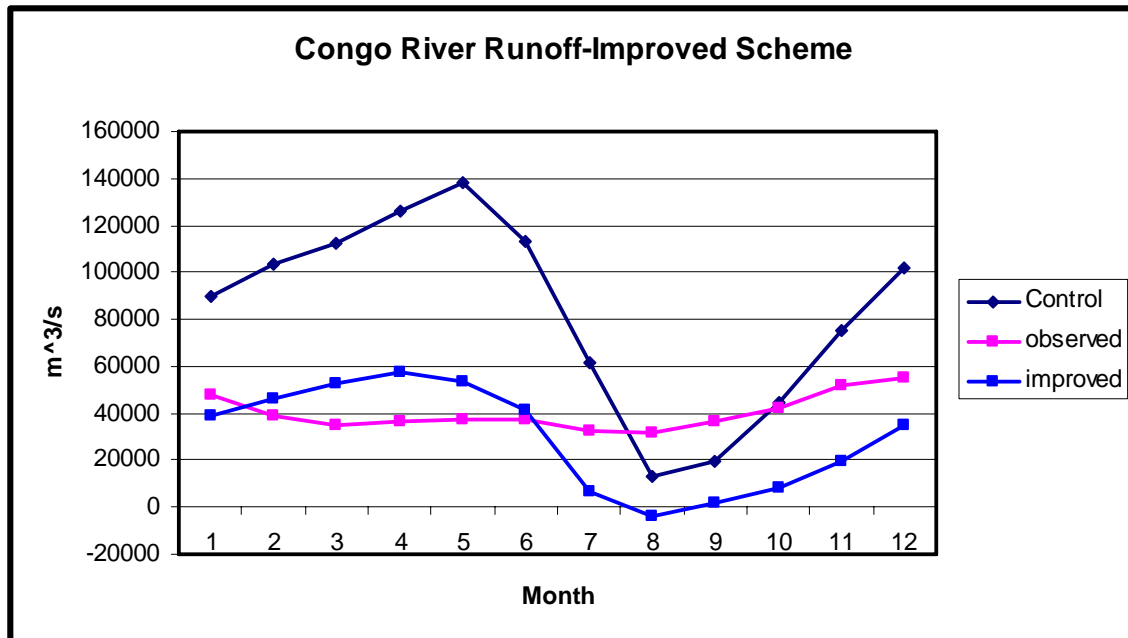


Figure 4.14 Improved runoff simulation based on the new scheme.

CHAPTER 5

ATMOSPHERIC COMPONENT OF THE HYDROLOGICAL CYCLE

5.1 Water Vapor Transport

The major processes that define the hydrological cycle at the land surface (especially in the tropical forests) are precipitation, interception, runoff, evaporation and infiltration.

Figure 5.1 shows evapotranspiration as a percentage of the total rainfall over the Congo basin for the period 1979-1988, while figure 5.2 depicts a comparison of precipitation and canopy evapotranspiration.. Mean monthly evapotranspiration values during the rainy season MAM and OND lie between 15%-20% of the total precipitation. This result is not in close agreement with the studies over the Amazon basin which indicated that about 50% of precipitation over the Amazon region is occasioned by recycled water vapor within the area (Salati et al 1979). The locally recycled water vapor can not therefore account for the high rainfall values in the MAM and OND periods (figure 2.1). The global circulation pattern is the only feasible explanation for the influx of moisture over the Congo basin in these seasons. Further discussions on moisture transport and the dynamical monsoon theory in chapter 6 explain some of the circulation characteristics that support this hypothesis

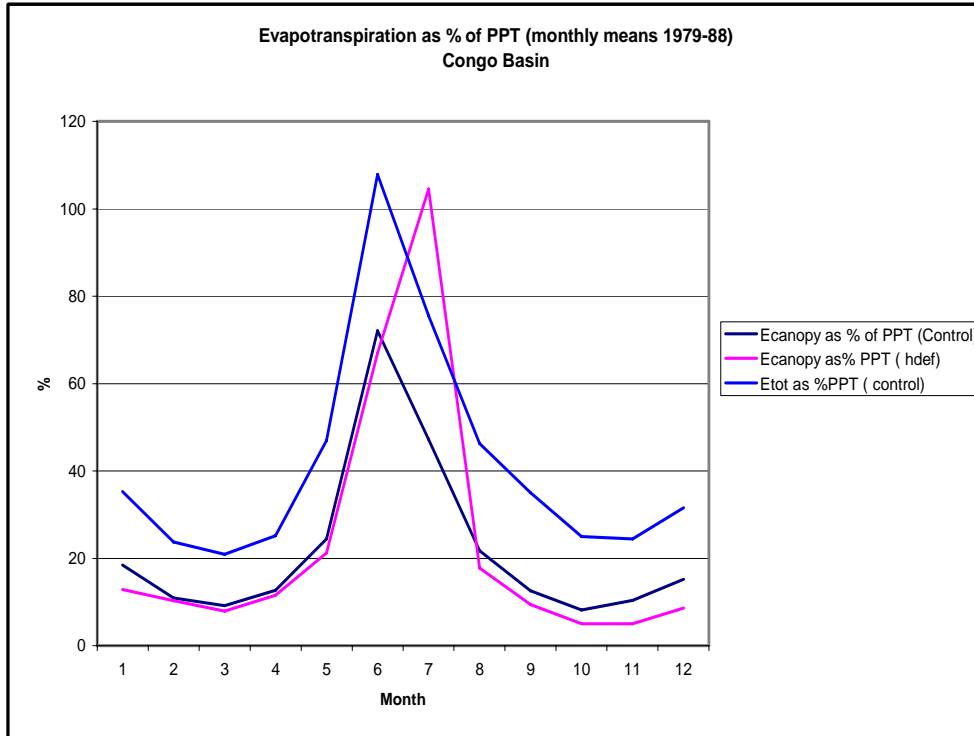


Figure 5.1 Evapotranspiration (from forest canopy) and total evaporation (forest canopy plus ground evaporation) shown as a percentage of total precipitation in both control and modified CAM2 simulations

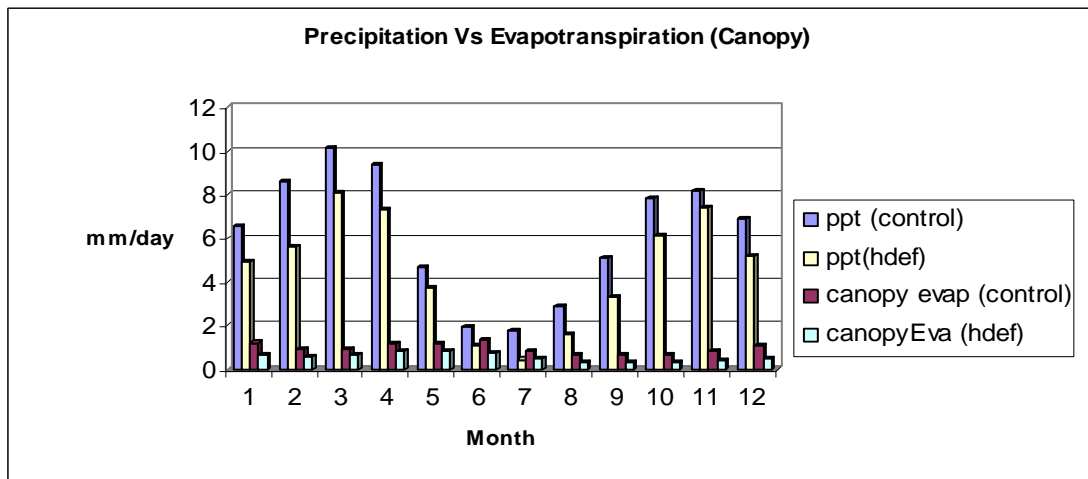


Figure 5.2 Comparison of Precipitation and Canopy evapotranspiration

5.2 Zonal and Meridional Wind patterns over the Congo Basin

A contour plot of the zonal transport of water vapor (Figure 5.3 and Figure 5.4) indicates an eastward transfer of water vapor (from the Atlantic-probably from the cold Benguela currents) during the drier months of JJA and a westward transfer (at reduced magnitudes) from the Indian Ocean during the wetter OND season.

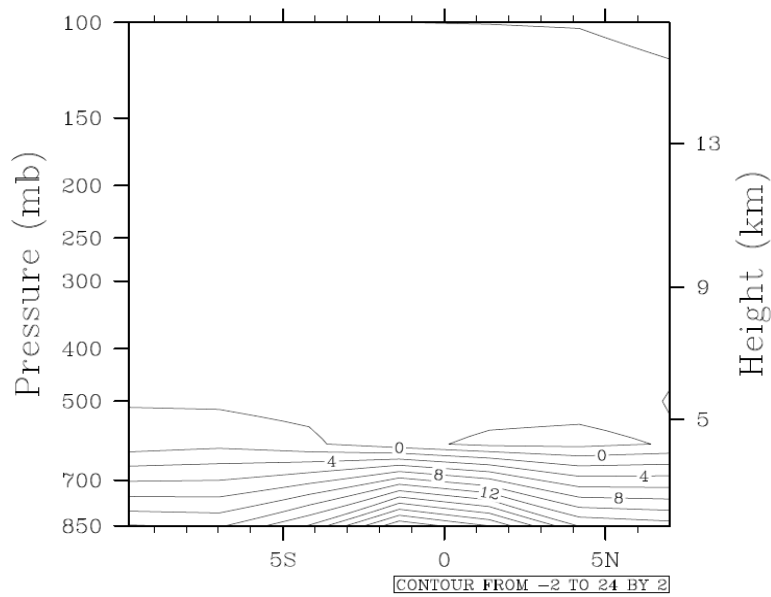


Figure 5.3 Zonal water vapor transport JJA (unit m/sg/kg)

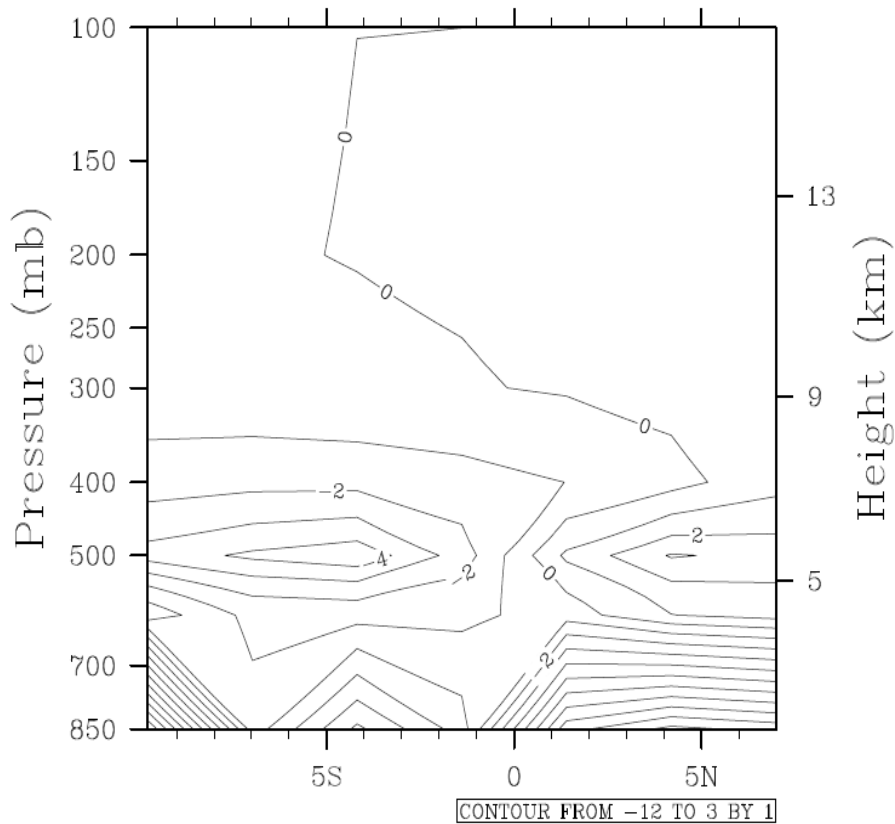


Figure 5.4 Zonal water vapor transport OND ((unit m/sg/kg))

A contour plot of the meridional transport of water vapor (Figure 5.5) indicates a southward transfer of water vapor (from the oceans) during the drier months of JJA and a reversal of the flow (at reduced magnitudes) during the wetter OND season. This is divergence and convergence of water vapor during the dry and wet seasons respectively indicative of the monsoon type of circulation over the Central Equatorial region.

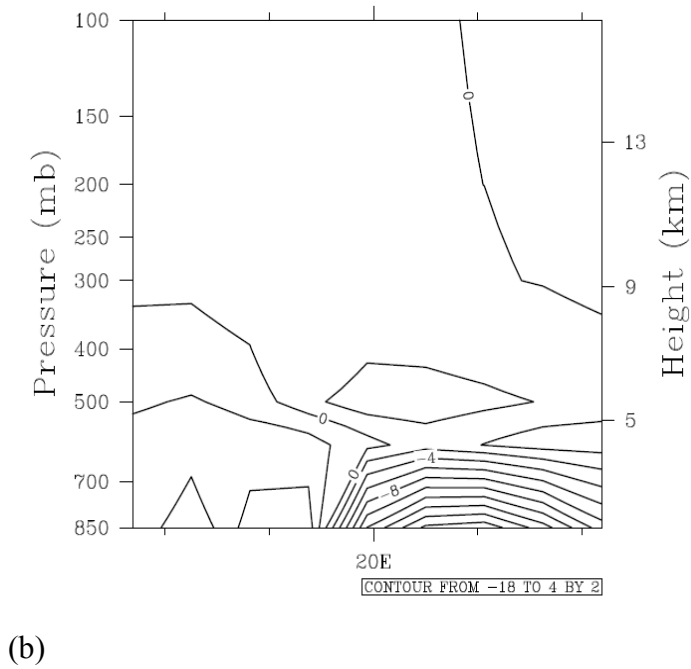
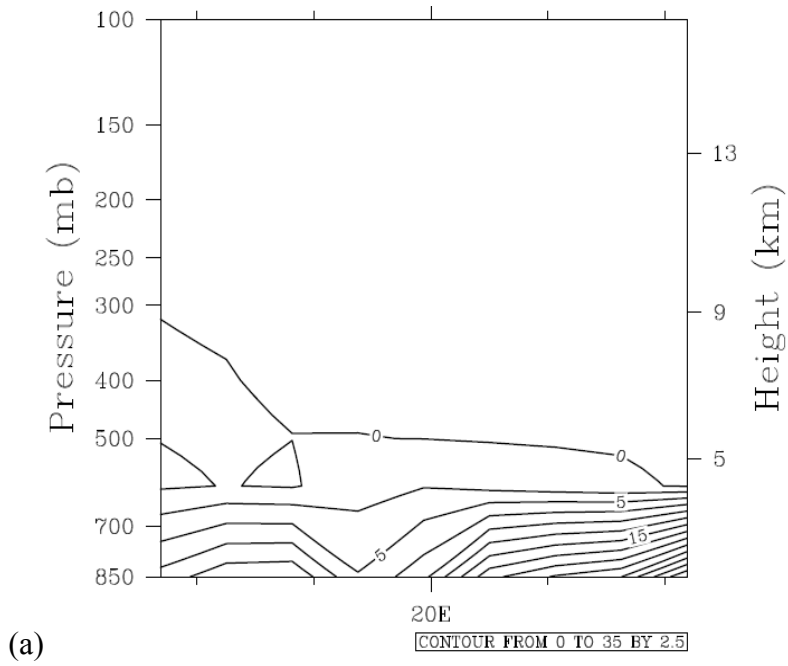


Figure 5.5 Meridional water vapor transport for (a) OND and (b) JJA

The divergence field of water vapor in the atmosphere is dependant on the mean difference between evaporation and precipitation. In OND, over the Congo basin, mean evapotranspiration is less than mean precipitation, ($E_{\text{mean}} - P_{\text{mean}}$ is negative), and the region therefore acts as a sink for water vapor while the situation is reversed in the JJA period. These relatively high values of water vapor transport in the lower levels, peaking at 850mb, are indicative of the low level branches of the Hadley cells which give the largest contribution to the total meridional flux of water vapor (Peixoto and Oort,1992) .

The amount of water vapor contained in a unit column of air (i.e. precipitable water), W , is given by

$$W (\lambda, \phi, t) = \int_0^{p_0} q \frac{dp}{g} \quad (5.1)$$

where q is the specific humidity, λ is the longitude, ϕ is the latitude and t is time.

The aerial runoff Q is then calculated as

$$Q(\lambda, \phi, t) = \int_0^{p_0} qv \, dp/g = Q_{\lambda} i + Q_{\phi} j \quad (5.2)$$

The zonal and meridional components of Q are then given by

$$Q_{\lambda} = \int_0^{p_0} qu \frac{dp}{g} = \langle qu \rangle p_0 / g \quad (5.3)$$

$$Q_{\phi} = \int_0^{p_0} qv \frac{dp}{g} = \langle qv \rangle p_0 / g \quad (5.4)$$

The continuity equation can be written as

$$\text{div}V + \frac{\partial w}{\partial p} = 0 \quad (5.5)$$

And the water balance equation for water vapor is

$$\frac{dq}{dt} = s(q) + D \quad (5.6)$$

Where $s(q)$ indicates the sources or sinks of water vapor and D is the molecular and turbulent eddy diffusion of water vapor. The term $s(q)$ can be represented by the difference between the rate of evaporation plus sublimation and the rate of condensation per unit mass

Combining equations 5.5 and 5.6 we get

$$\frac{\partial q}{\partial t} + \text{div}qV + \frac{\partial(qw)}{\partial p} = s(q) + D \quad (5.7)$$

A balance equation for the condensed phase of water vapor can be given similarly as

$$\frac{\partial q_c}{\partial t} + \text{div}q_cV + \frac{\partial q_c w_c}{\partial p} = -(e - c) \quad (5.8)$$

Where e is the rate of evaporation and c is the rate of condensation.

For the total water content, a balance equation is then given by

$$\frac{\partial q}{\partial t} + \text{div}qV + \frac{\partial(qv)}{\partial p} + \frac{\partial q_c}{\partial t} + \text{div}q_cV + \frac{\partial q_c w_c}{\partial p} = D \quad (5.9)$$

Integrating this equation with respect to pressure from the surface to the top of the atmosphere we get the balance equation for total water substance in the atmosphere as

$$\frac{\partial W}{\partial t} + \text{div}Q + \frac{\partial W_c}{\partial t} + \text{div}Q_c + P = E \quad (5.10)$$

Where W_c is the amount of condensed water in a unit column of air and Q_c is the horizontal transport vector of condensed water. Often

$$\frac{\partial W_c}{\partial t} \ll \frac{\partial W}{\partial t} \text{ and } Q_c \ll Q \text{ so that both the time rate of change of the liquid and}$$

solid water in the clouds and their horizontal transports can be neglected. The general water balance equation can hence be reduced to

$$\frac{\partial \bar{W}}{\partial t} + \text{div}\bar{Q} = \bar{E} - \bar{P} \quad (5.11)$$

Equation 5.11 indicates that the excess of evaporation over precipitation at the earth's surface is balanced by the local rate of change of water vapor storage $\frac{\partial W}{\partial t}$ and by the inflow or outflow of water vapor $\text{div}Q$.

When averaged over a region e.g. a drainage basin we get

$$\left\{ \frac{\partial \bar{W}}{\partial t} \right\} + \{ \text{div}Q \} = \{ \bar{E} - \bar{P} \} \quad (5.12)$$

Equation 5.12 defines the atmospheric branch of the hydrological cycle, which is often not well represented in the hydrological models. The rate of change of precipitable water

$\frac{\partial W}{\partial t}$ is usually very small (except in storms and even then only for a short time) in comparison to the other terms. Hence over a long period, divergence of water vapor is found where evaporation exceeds precipitation and convergence of water vapor is found where precipitation exceeds evaporation

5.3 Monsoon type of circulation over the Congo Basin

One of the key elements in the definition of monsoon circulation is the seasonal change in wind direction in correlation to the cessation or onset of the rainfall period over a region. The surface wind direction during the monsoon onset is from the sea to the land bringing in moisture while the upper wind tends to flow in the opposite direction in conformity with the moisture convergence/divergence theory. In figures 5.5- figure 5.7 seasonal precipitation maps were overlain with the horizontal wind field at approximately 950mb (surface) level to identify areas of high correlations between moisture convergence and rainfall. As aforementioned the acronyms MAM, JJA, OND refer to calendar months i.e. MAM for March-May, etc. It can be seen that convergence in wind direction over the Congo in the MAM and OND season is consistent with the high rainfall values received during these seasons. The JJA season wind direction (land breeze) is equally in phase with the reduced rainfall amounts noted in this season.

_multiply_PRECC_86400000_0

Mean 2.5389

Max 13.8763

Min 0.0151312

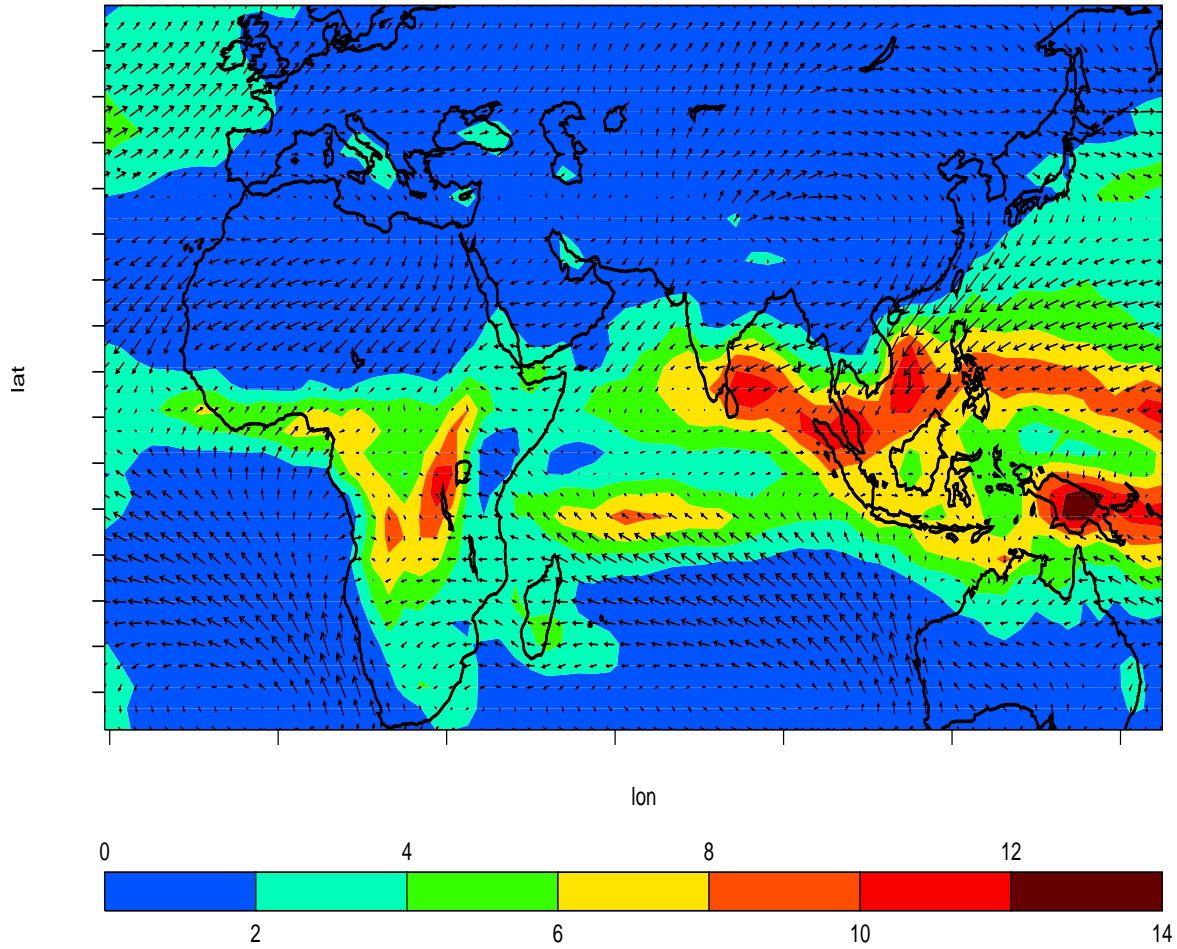


Figure 5.6 Rainfall in mm/day for the MAM period overlain with surface winds

_multiply_PRECC_86400000_0

Mean 2.94427

Max 23.8144

Min 6.30525E-7

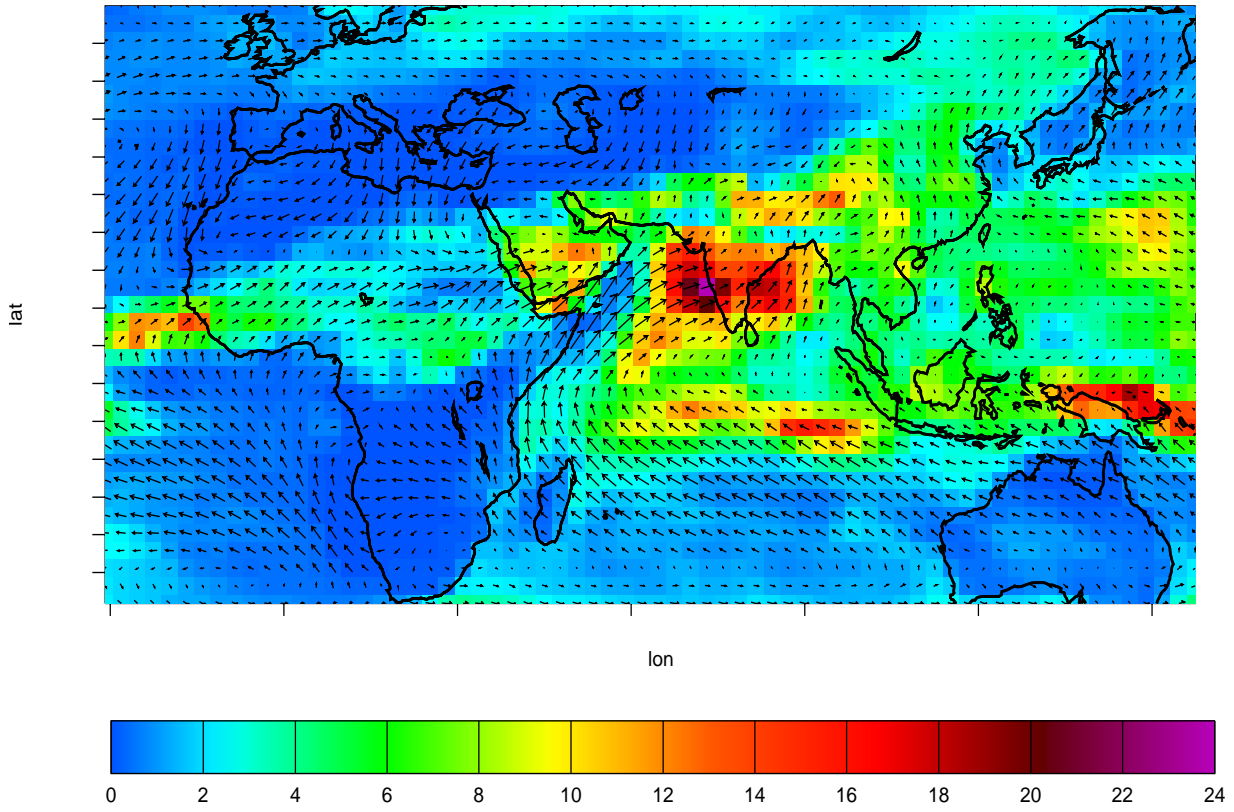


Figure 5.7 Rainfall in mm/day for the JJA period overlain with surface winds

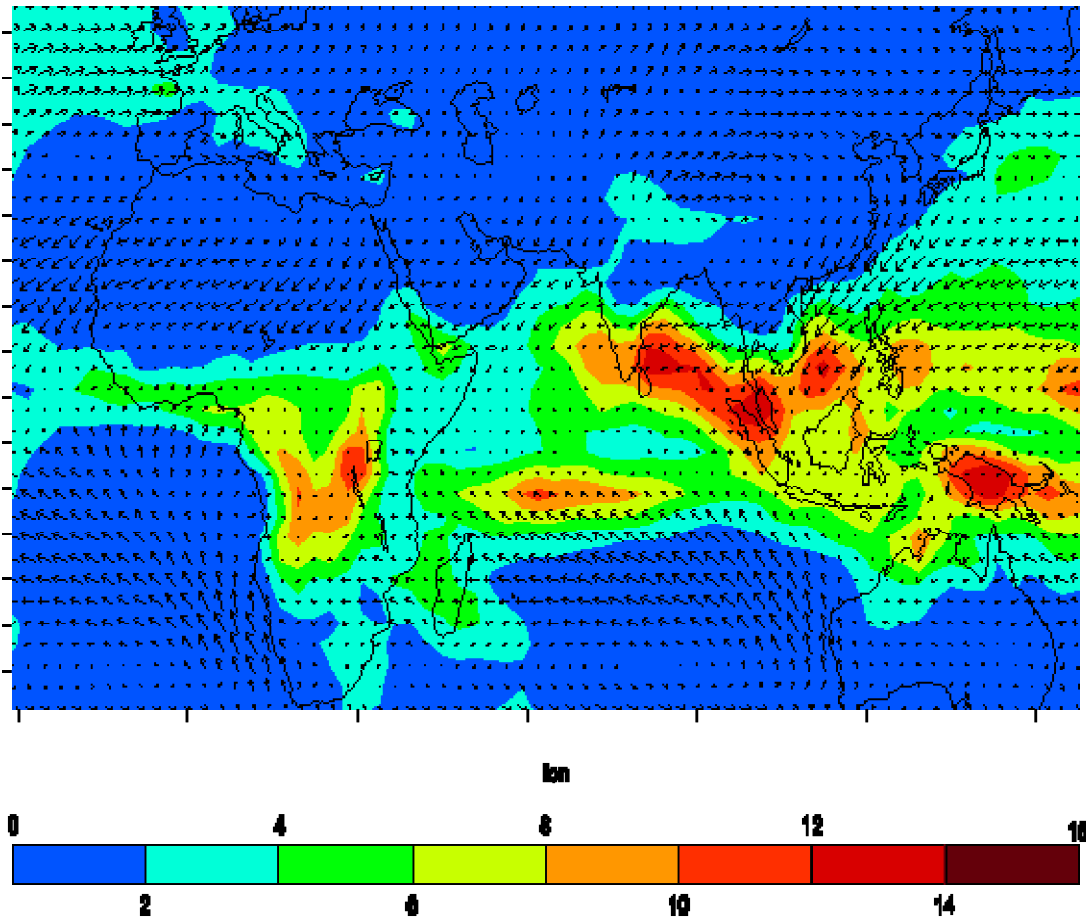


Figure 5.8 Rainfall in mm/day for the OND period overlain with surface winds

The influx of moisture (convergence) over the Congo basin in MAM and OND are the maritime inflows from the Indian and Atlantic oceans as can be see from figure 5.5 and figure 5.7. Arguably this phenomenon can be explained as monsoonal because of its periodicity and change of wind direction associated with its onset (Slingo, 2003). On the other hand it can be explained as the equatorial convergence of water vapor associated with the ITCZ (Webster and Fasullo, 2003).

As mentioned in the last paragraph of section 5.1, the atmospheric branch of the hydrological cycle is often not sufficiently addressed in the standard hydrological models used in river runoff simulation. While the terrestrial branch of the hydrological cycle consists of the inflow (mostly precipitation), outflow (runoff) and storage (lakes and groundwater) the atmospheric branch of the cycle refers to the atmospheric transport of water, usually in the vapor phase. The two branches seamlessly join together at the interface between the earth surface and the atmosphere, figure 5.9.

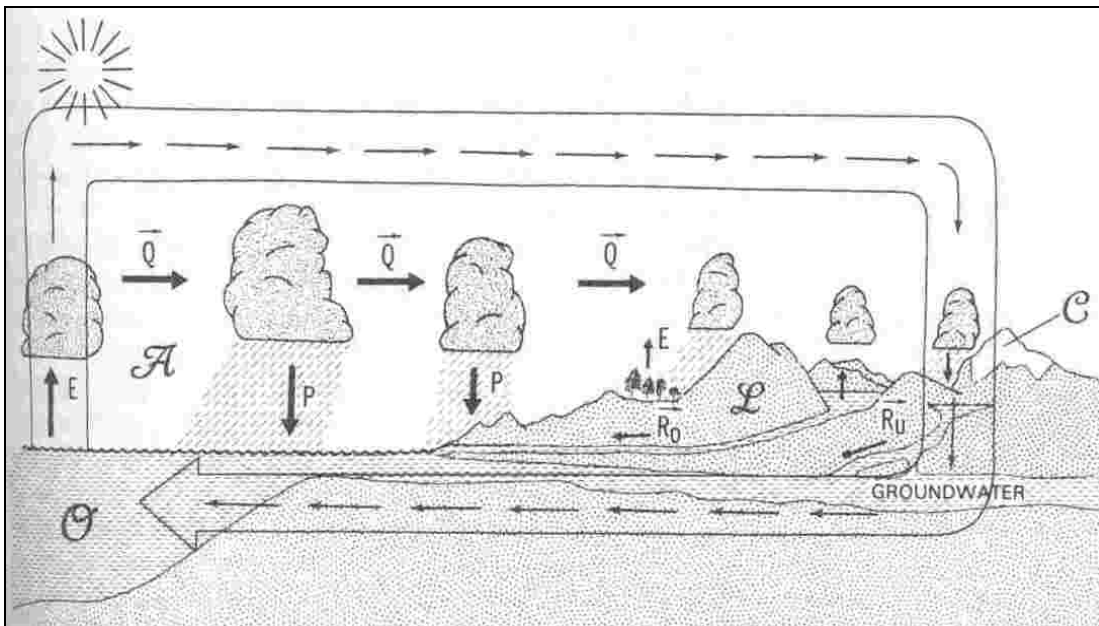


Figure 5.9 The hydrological cycle depicting the continuity provided by the terrestrial and atmospheric branches, (Peixoto and Oort Physics of Climate)

CHAPTER 6

DYNAMICAL THEORY OF MONSOONAL CIRCULATION IN THE TROPICS

6.1 Dynamical Theory

The dynamical theories of thermally direct, zonally symmetrical circulations in the tropical atmosphere has been studied by various researchers including Held and Hou (1980), Lindzen and Hou (1988), Plumb and Hou (1992), and Emmanuel et al (1994). A summary of their findings is that below a certain threshold value of thermal forcing the atmosphere maintains a steady state of thermal equilibrium with no meridional flow. Beyond this threshold value of thermal forcing the equilibrium breaks down and a meridional circulation is initiated. The subtropical thermal forcing can be distinctively described for dry and moist atmospheres. Plumb and Hou (1992) described it for a dry atmosphere by specifying the distribution of equilibrium temperature. For a moist atmosphere (Eltahir and Ngong, 1996) a quasi-equilibrium balance between moist convection and large scale radiative forcing and hence a uniform vertical distribution of saturation entropy is assumed. The moist atmosphere assumption is even more appropriate for the Congo Basin relative to the Sahel region (the location of Eltahir and Ngong's experiment) and is therefore used in this study. Depending on the distribution of entropy, either of two possible regimes may dominate the dynamics of tropical atmosphere: a radiative-convective equilibrium regime or an angular momentum conserving regime (Plumb and Hou 1992).

The thermal wind can be expressed by (for a zonally symmetric atmosphere)

$$\frac{\partial u}{\partial p} = \frac{1}{f} \frac{\partial \alpha}{\partial y}, \quad (1)$$

where u is zonal wind and p is pressure, f is the coriolis parameter, α is specific volume and y is the meridional distance. Using Maxwell's theory we have

$$\left(\frac{\partial \alpha}{\partial y} \right) = \left(\frac{\partial \alpha}{\partial s} \right)_p \frac{\partial s^*}{\partial y} = \left(\frac{\partial T}{\partial p} \right)_{s^*} \frac{\partial s^*}{\partial y} \quad (2) \text{ where } s^* \text{ is saturation entropy and is given by } s^*$$

$= C_p \ln(\theta_{e^*})$. C_p is the specific heat capacity at constant pressure and θ_{e^*} is the equivalent potential temperature of air saturated at the same pressure and temperature. Integrating eqn. (1) from the surface ($u=0$) to the tropopause under the assumption of a moist adiabatic lapse rate we have

$$u_t = -\frac{1}{f} (T_o - T_t) \frac{\partial s_b}{\partial y}, \quad (3)$$

where u_t and T_t are wind and temperature at the tropopause, T_o is the surface temperature and s_b ($\sim s^*$) is the boundary layer entropy.

The absolute vorticity at the tropopause is given by

$$\eta_t = f - \left(\frac{\partial u_t}{\partial y} \right) \quad (4)$$

$$\rightarrow \eta_t = f + \frac{\partial}{\partial y} \left(\frac{1}{f} (T_o - T_t) \frac{\partial s_b}{\partial y} \right) \quad (5)$$

Equation (5) indicates the relationship between absolute vorticity at the tropopause and the meridional distribution of boundary layer entropy. The distribution of entropy will thus dictate which of the two possible regimes will dominate the tropical atmosphere. Either a radiative –convective equilibrium regime or an angular momentum conserving regime (Plumb and Hou, 1992) will prevail depending on the sign of the absolute vorticity in relation to the coriolis parameter. A radiative-convective equilibrium regime should prevail if the absolute vorticity at the tropopause has the same sign as the coriolis parameter f . This condition implies

$$1 + \frac{1}{f^2} \frac{\partial}{\partial y} \left((T_0 - T_t) \frac{\partial S_b}{\partial y} \right) - \frac{\beta}{f^3} (T_0 - T_t) \frac{\partial S_b}{\partial y} > 0 \quad (6)$$

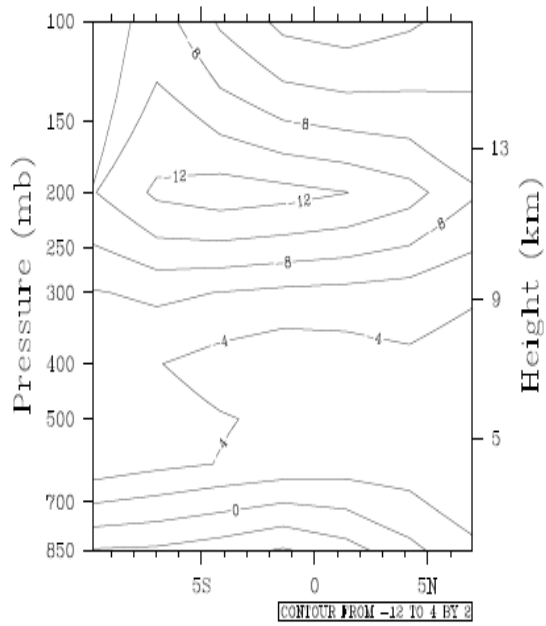
where β is $\partial f / \partial y$. This derivation assumes a geostrophic wind approximation (not very appropriate for near equatorial regions. Under the assumption of a gradient wind balance a similar set of equations can be derived i.e.

$$\left(\frac{\partial}{\partial \varphi} \left[\frac{\cos^3 \varphi}{\sin \varphi} (T_0 - T_t) \frac{\partial S_b}{\partial \varphi} \right] \right) + 4\Omega^2 a^2 \cos^3 \varphi \sin \varphi > 0, \quad (7)$$

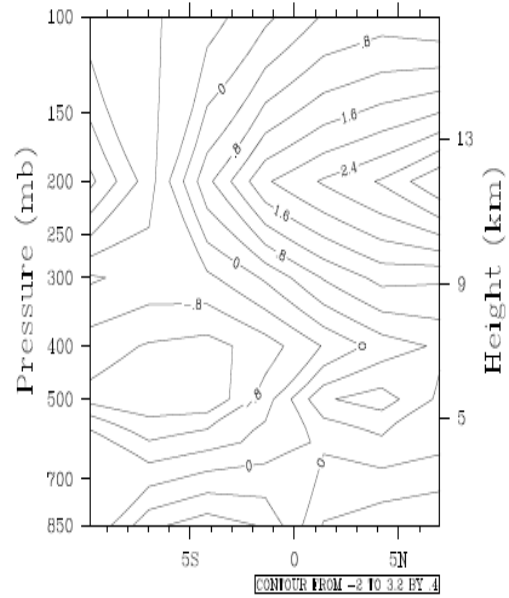
where φ is latitude and Ω is the angular velocity of the earth. When the absolute vorticity gets close to zero or when condition (6) or (7) is violated then the angular momentum conserving regime is predominant and a meridional (monsoon) circulation is initiated. Equation (6) indicates that the gradient and the second derivative of the meridional distribution of boundary-layer entropy control the threshold levels which trigger the monsoonal circulation. A zero absolute vorticity in the upper troposphere is therefore

indicative of the presence of monsoon circulation. If this theory holds then the monsoon type of circulation over the Congo Basin should be sensitive to natural or anthropogenic perturbations (e.g. deforestation) that may impact the meridional gradient of boundary layer entropy.

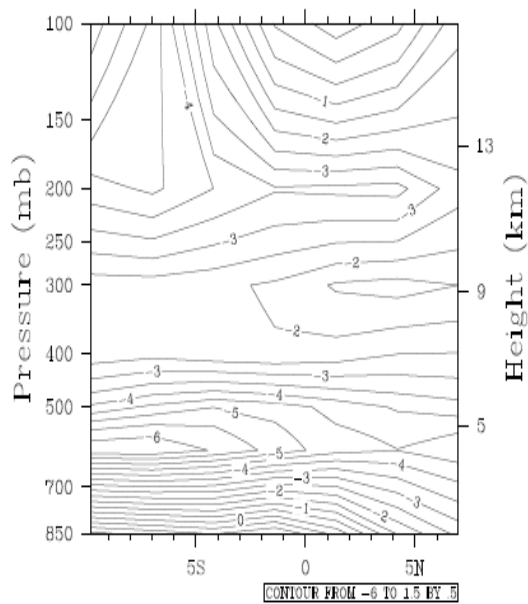
A comparison of the OND zonal and meridional wind velocities for the relatively wetter 1980 and drier 1981 is shown in Figure 6.1 below. The zonal wind at the upper levels (about 200mb) is seen to be stronger for the wetter year (1980) than for the drier year (1981). The differences in meridional wind velocities between the two years are harder to detect but a keen observation reveals that the wind velocity contours are slightly more packed in the case of the wetter year



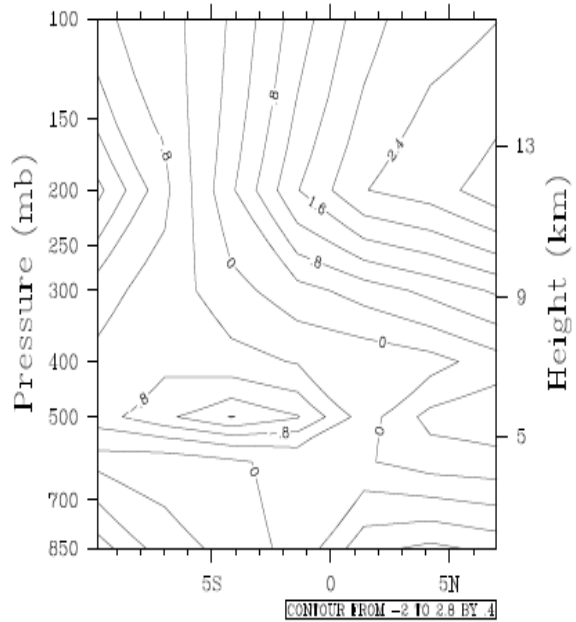
(a)



(b)



(c)



(d)

Figure 6.1 Average wind velocity (m/s) for OND at the 20°E meridional cross section (a) zonal velocity for 1980, (b) meridional velocity for 1980, (c) zonal velocity for 1981 and (d) meridional velocity for 1981

6.2 Factors that Influence the Boundary Layer Entropy

Several factors and phenomena over land, ocean and the atmosphere can have some influence on the meridional gradient of boundary layer entropy. For coastal locations like the Congo Basin, the entropy fluxes from both the ocean and land surfaces can play very significant roles in modifying the boundary layer entropy via various physical processes like convective cloud formation, radiative cooling, variability in sea surface temperature (SST) and land cover changes. Eltahir and Gong (1996) proposed a land-atmosphere-ocean interaction as seen in figure 6.2 which graphically sums the concept of the theory using the arguments from the dynamic theory discussed in section 6.1. Barring dramatic changes in the other factors that influence the meridional gradient of boundary layer entropy, the interplay between the influences of SST and land cover changes on precipitation is well summarized in figure 6.2.

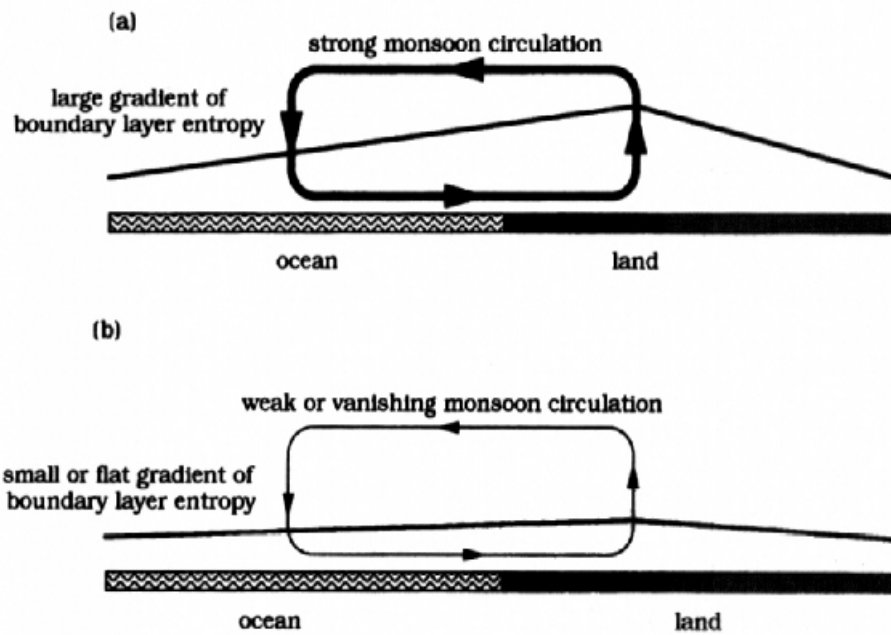


Figure 6.2 Schematic of the proposed land –atmosphere –ocean interaction over West Africa (Eltahir and Gong-1996)

6.3 Correlation of precipitation with meridional wind

A cross-spectral analysis applied to precipitation and meridional wind speed reveals better correlation between the two variables in the deforested case in comparison to the control case. The difference is more evident in the upper levels, approximately 200mb, as shown in the time series plot for the two variables in figure 6.3 and figure 6.4.

Figure 6.5 and figure 6.6 show the cross-spectra of precipitation and meridional wind speed together with the cross wavelet for the deforested and control case respectively.

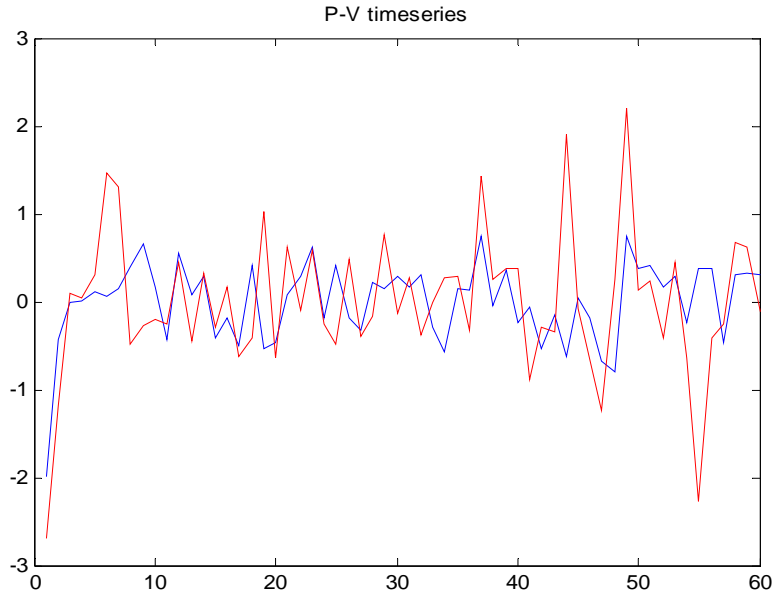


Figure 6.3 Monthly time series of precipitation versus meridional wind (200 mb-level) – high deforestation case—after removing the seasonal cycle.

In these time series graphs (above and below) the red line represents meridional wind while the blue line represents precipitation.

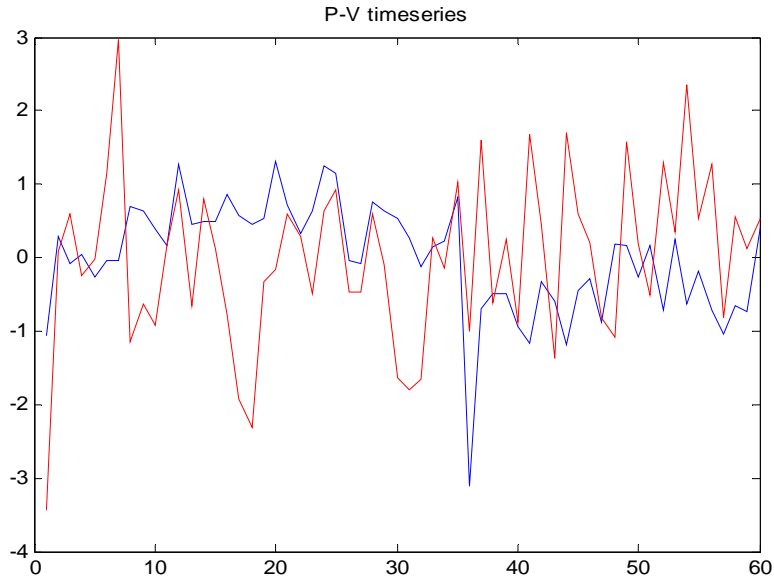


Figure 6.4 Monthly time series of precipitation versus meridional wind (200 mb level) – control case–after removing the seasonal cycle.

The correlation coefficient between precipitation and meridional wind is stronger in the deforestation case at the seasonal cycle and weakens as the frequency increases, figure 6.5. Though the correlation improves again at much higher frequencies (near monthly cycles), the noise level increases too and it's more difficult to identify the physical meaning of the phenomena.

A similar picture is depicted in the control case but at weaker correlations in comparison to the deforested case. There is a wider scatter of the high correlation points and there are more breaks of the correlation contours for the various frequencies.

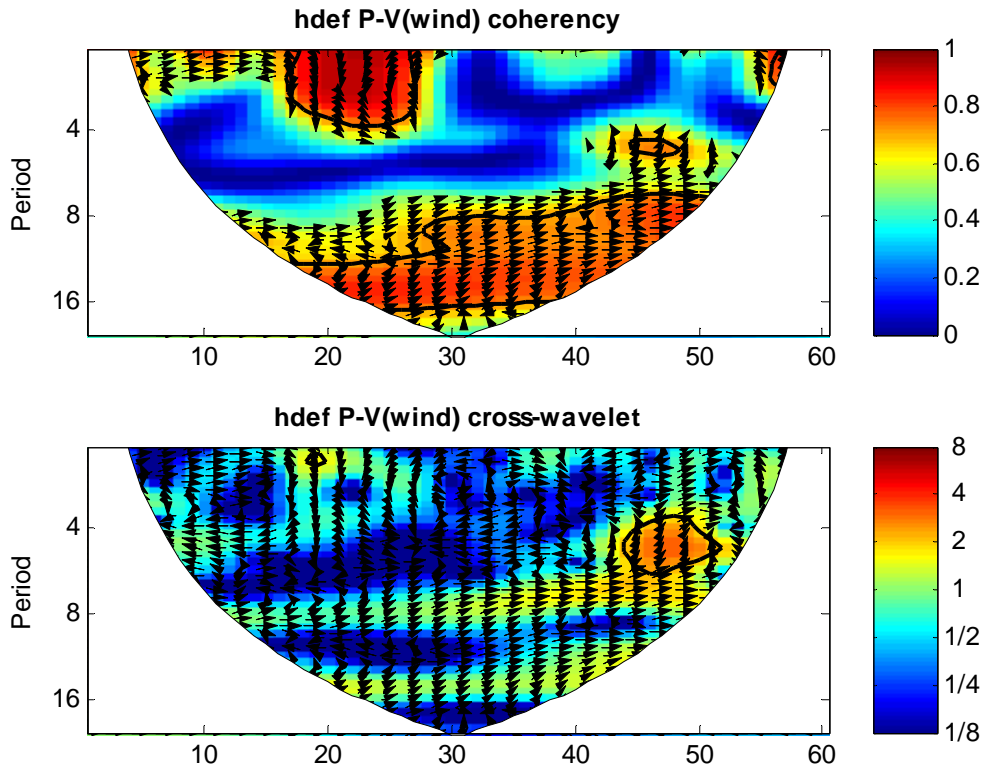


Figure 6.5 Coherency and cross-wavelet between precipitation and meridional wind (200 mb level) –high deforestation case

The differences brought forth in the cross-spectral analysis of the correlation between meridional wind speed and precipitation for the control and high deforestation cases give credence to the possibility of boundary layer fluxes (including boundary layer entropy) influencing the strength of the monsoon as discussed in the ‘dynamical theory of monsoonal circulation in the tropics’ in section one of this chapter. The correlation between the two variables for the control case is weaker and patchy over the frequency spectrum, from monthly to inter-annual cycles, figure 6.6. Though the cross-wavelet analysis in figure 6.7 and figure 6.8 seems to confirm the above relationships between meridional wind speed and precipitation, the noise level makes them harder to interpret.

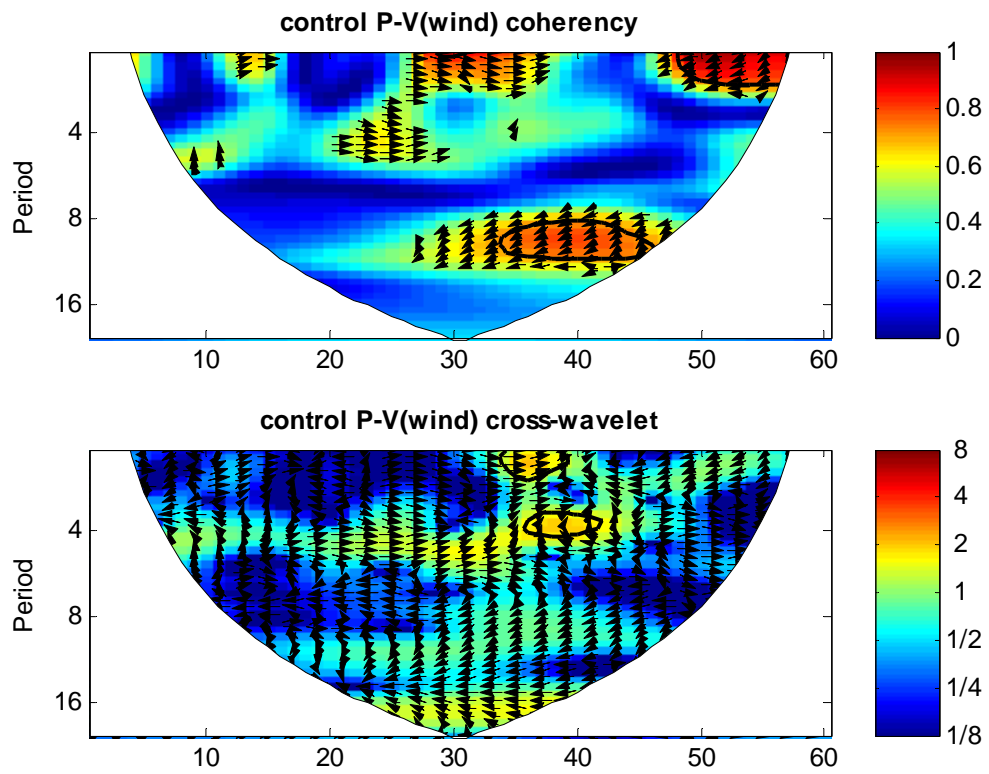


Figure 6.6 Coherency and cross-wavelet between precipitation and meridional wind (200 mb level) soil liquid –control case

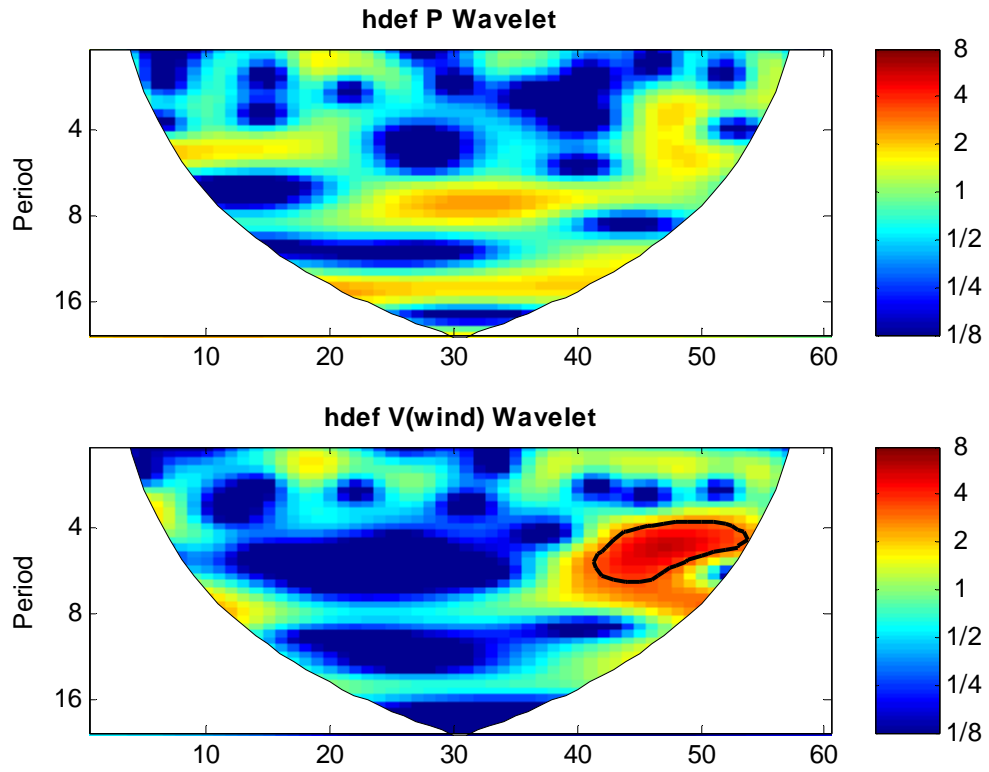


Figure 6.7 Relative strength of the amplitudes of precipitation and meridional wind wavelets at various frequencies (periods)- high deforestation

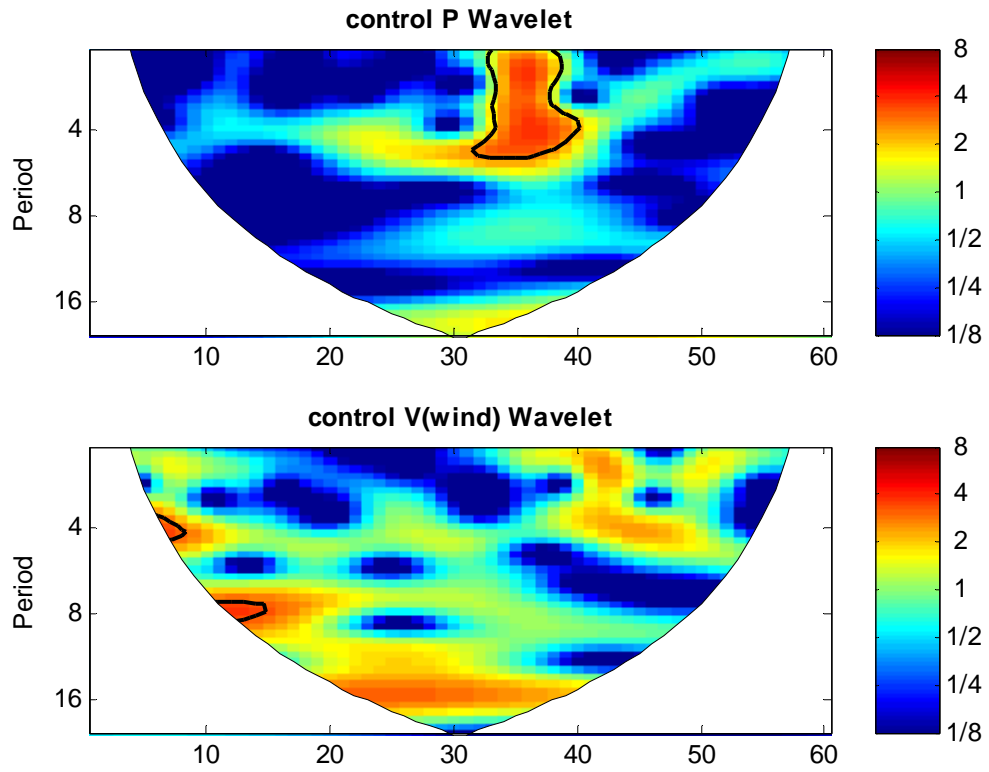


Figure 6.8 Relative strengths of the amplitudes of precipitation and meridional wind wavelets at various frequencies (periods)- control case

6.4 Discussion

The dynamical theory of zonally symmetrical and thermally direct circulations which suggests that a meridional monsoon circulation develops over tropical regions when the absolute vorticity near the tropopause reaches a threshold value has been tested here for the Congo basin. The results though not in direct conflict with the theory, are not strong enough to confirm it.

In their studies of the Sahel region (West Africa), Eltahir and Gong concluded that the theory and observations suggested that the dynamics of the monsoons are regulated by the meridional gradient of boundary layer entropy. Their comparisons of zonal and meridional wind for the wettest and driest years for the 1958 to 1967 showed marked differences, with the wetter year clearly exhibiting stronger winds.

This study (dissertation) lacked the benefit of observational data and even though the model simulation could be used as a surrogate, a critical testing of this hypothesis is not feasible without the use of a dynamic vegetation model. However such a model will in turn bring in several uncertainties.

CHAPTER 7

SUMMARY AND CONCLUSIONS

7.1 Comments on effects of perturbing vegetation cover

This study has shown that long term perturbations of the existing vegetation cover in the Congo Basin could cause changes in hydroclimatic parameters like rainfall, evapotranspiration, runoff and other parameters like temperature, sensible and latent heat flux.

Recent advances in land surface modeling schemes, e.g. CLM3 used in this study, have made these sub-models useful tools in the investigation of hydroclimatic effects of minimal perturbations of vegetation in a hydrological basin like the Congo.

The influence of vegetation change on rainfall is rather mixed with decrease in rainfall following high deforestation (experiment 1) and a slight increase in precipitation after low deforestation. Using the current data quality and quantity these changes are not statistically significant, however there are indications that these changes can lead to some feedback mechanism in the earth system loop. The spatial patterns of rainfall following the deforestation experiments varied with the rainfall sub seasons of MAM and OND.

Changes in evapotranspiration followed a similar pattern, temporally, in comparison to those of precipitation. The proportion of evapotranspiration to precipitation during the rainy periods of MAM and OND is low and supports the hypothesis that locally recycled water vapor can not therefore account for the high rainfall values in these periods. The global circulation pattern is therefore duly considered as a feasible explanation for the influx of moisture over the Congo basin in these seasons.

Simulated channel runoff for the Congo River is still much higher (by more than a factor of 2 to 3 during the rainy seasons) than observations. Neglecting the limitations on the quality of runoff simulation imposed by the model resolution, the other notable factors influencing the runoff quantities are overestimation of rainfall by the model, parameterization of the hydrological processes, especially in the soil, exclusion of possible water losses to some ground water aquifers at deeper levels than considered in the model and possible weaknesses in the routing scheme employed in the river transfer module. The improved scheme suggested in this study is simplistic in view of the issues mentioned above but goes a long way in highlighting the need for more data oriented and field based methods in finding a more robust solution

Statistical analysis of the relationships between precipitation and the wind patterns (zonal and meridional) before and after deforestation indicates higher coherency in the latter case. This result lends credence to Eltahir and Ngong's theory on the dynamics of wet and dry years in West Africa.

Quantitative proof of the dynamical theory of monsoon circulation over the Congo basin would require observational data that can facilitate estimation of the boundary layer entropy e.g., humidity and temperature at various pressure levels.

7.2 CONCLUSIONS

This study has addressed the hypothesis that long term perturbations of vegetation over the Congo basin has significant influence on the hydroclimatic variables over the basin and hence in the intensity of the hydrological cycle.

The study has also identified several issues, in the biosphere-atmosphere interaction over the Congo basin, that are pertinent to the improvement of land-atmosphere models in particular and to the earth system models in general.

Even though these findings are the result of the application of a single model and are specifically based on the structure and the design of the coupling between the community climate model (cam3) and the community land model (clm3) they can be generalized to aide in other modeling efforts, especially in the tropical regions

The verdict on the hypothesis is:-

- (i) The results of cam3/clm3 model experiments indicate spatial and temporal changes in precipitation, evapotranspiration and runoff values in the Congo Basin following deforestation.
- (ii) Even though precipitation tends to decrease with deforestation the decrease is not linear with regard to the removal of individual forest type but is dependent on the aggregate characteristics of the mosaic of the residue plant functional types in the basin.
- (iii) The vegetation index over the Congo basin influences the correlation between precipitation and the meridional wind flow at different pressure levels.

Issues that are pertinent to the improvement of land-surface modeling in the tropics are

- (i) Runoff parameterization based on observed soil hydraulic properties and higher resolution topography data would improve runoff simulation for major rivers like the Congo
- (ii) More observations of land and atmospheric data e.g. soil moisture, humidity, temperature etc at various pressure levels to ground truth some modeling efforts and results

APPENDIX A

IGBP LAND COVER TYPES

Table A.1 IGBP Land Cover Types Definition

Natural Vegetation		
1	Evergreen Needle leaf Forest	Land dominated by woody vegetation with a percent cover > 60%; Height exceeding 2 meters; Almost all trees remain green all year. Canopy is never without green foliage.
2	Evergreen Broadleaf Forests	Lands dominated by woody vegetation with a percent cover > 60%; Height exceeding 2 meters; Almost all trees and shrubs remain green year round. Canopy is never without green foliage.
3	Deciduous Needle-leaf Forests	Land dominated by woody vegetation with percent cover > 60%; Height exceeding 2 meters; Consists of seasonal needle-leaf tree communities with an annual cycle of leaf-on and leaf-off periods.
4	Deciduous Broadleaf Forests	Land dominated by woody vegetation with percent cover > 60%; Height exceeding 2 meters; Consists of broadleaf tree communities with an annual cycle of leaf-on and leaf-off periods.
5	Mixed Forests	Land dominated by woody vegetation with percent cover > 60%; Height exceeding 2 meters; Consists of broadleaf tree communities with an annual cycle of leaf-on and leaf-off periods.

Table A.1 (continued)

6	Closed Shrub-lands	Land with shrub canopy cover > 60%; With woody vegetation less than 2 meters tall; The shrub foliage can be either evergreen or deciduous.
7	Open Shrub-lands	Land with shrub canopy cover between 10 – 60%; With woody vegetation less than 2 meters tall; The shrub foliage can be either evergreen or deciduous.
8	Woody Savannas	Land with forest canopy cover between 30 – 60%; Forest cover height exceeds 2 meters; With herbaceous and other understory systems.
9	Savannas	Land with forest canopy cover between 10 – 30%; Forest cover height exceeds 2 meters; With herbaceous and other understory systems.
10	Grasslands	Tree and shrub cover is less than 10%; With herbaceous types of cover.
11	Permanent Wetlands	Land with a permanent mixture of water and herbaceous or woody vegetation; the vegetation can be present in either salt, brackish, or fresh water.
Developed and Mosaic Lands		
12	Croplands	Lands covered with temporary crops followed by harvest and bare soil period (e.g., single and multiple cropping systems). Note that perennial woody crops will be classified as the appropriate forest or shrub land cover type

Table A.1 (continued)

13	Urban and Built-Up Lands	Land covered by buildings and other man-made structures.
14	Cropland / Natural Vegetation Mosaics	Lands with a mosaic of croplands, forests, shrub-land, and grasslands in which no one component comprises more than 60% of the landscape.
Non-Vegetation Lands		
15	Snow and Ice	Lands under snow/ice cover throughout the years.
16	Barren	Lands with exposed soil, sand, rocks, or snow and never has more than vegetated cover during any time of the year.
17	Water Bodies	Oceans, seas, lakes, reservoir, and rivers. Can be either fresh or salt-water bodies

Table A.2 Plant function type optical properties

Plant Functional Type	χ_L	α_{vis}^{leaf}	α_{nir}^{leaf}	α_{vis}^{stem}	α_{nir}^{stem}	τ_{vis}^{leaf}	τ_{nir}^{leaf}	τ_{vis}^{stem}	τ_{nir}^{stem}
NET Temperate	0.01	0.07	0.35	0.16	0.39	0.05	0.10	0.001	0.001
NET Boreal	0.01	0.07	0.35	0.16	0.39	0.05	0.10	0.001	0.001
NDT Boreal	0.01	0.07	0.35	0.16	0.39	0.05	0.10	0.001	0.001
BET Tropical	0.10	0.10	0.45	0.16	0.39	0.05	0.25	0.001	0.001
BET temperate	0.10	0.10	0.45	0.16	0.39	0.05	0.25	0.001	0.001
BDT tropical	0.01	0.10	0.45	0.16	0.39	0.05	0.25	0.001	0.001
BDT temperate	0.25	0.10	0.45	0.16	0.39	0.05	0.25	0.001	0.001
BDT boreal	0.25	0.10	0.45	0.16	0.39	0.05	0.25	0.001	0.001
BES temperate	0.01	0.07	0.35	0.16	0.39	0.05	0.10	0.001	0.001
BDS temperate	0.25	0.10	0.45	0.16	0.39	0.05	0.25	0.001	0.001
BDS boreal	0.25	0.10	0.45	0.16	0.39	0.05	0.25	0.001	0.001
C ₃ arctic grass	-0.30	0.11	0.58	0.36	0.58	0.07	0.25	0.220	0.380
C ₃ grass	-0.30	0.11	0.58	0.36	0.58	0.07	0.25	0.220	0.380
C ₄ grass	-0.30	0.11	0.58	0.36	0.58	0.07	0.25	0.220	0.380
Crop1	-0.30	0.11	0.58	0.36	0.58	0.07	0.25	0.220	0.380
Crop2	-0.30	0.11	0.58	0.36	0.58	0.07	0.25	0.220	0.380

Table A.3 Plant functional type root distribution parameters

Plant Functional Type	Root Distribution	
	r_a	r_b
NET Temperate	7.0	2.0
NET Boreal	7.0	2.0
NDT Boreal	7.0	2.0
BET Tropical	7.0	1.0
BET temperate	7.0	1.0
BDT tropical	6.0	2.0
BDT temperate	6.0	2.0
BDT boreal	6.0	2.0
BES temperate	7.0	1.5
BDS temperate	7.0	1.5
BDS boreal	7.0	1.5
C ₃ grass arctic	11.0	2.0
C ₃ grass	11.0	2.0
C ₄ grass	11.0	2.0
Crop1	6.0	3.0
Crop2	6.0	3.0

Table A.4 Plant functional type photosynthetic parameters

Plant functional type	$V_{\max 25}$	α	m
NET Temperate	51	0.06	6
NET Boreal	43	0.06	6
NDT Boreal	43	0.06	6
BET Tropical	75	0.06	9
BET temperate	69	0.06	9
BDT tropical	40	0.06	9
BDT temperate	51	0.06	9
BDT boreal	51	0.06	9
BES temperate	17	0.06	9
BDS temperate	17	0.06	9
BDS boreal	33	0.06	9
C ₃ arctic grass	43	0.06	9
C ₃ grass	43	0.06	9
C ₄ grass	24	0.04	5
Crop1	50	0.06	9
Crop2	50	0.06	9

$V_{\max 25}$, $\mu\text{mol m}^{-2} \text{s}^{-1}$. α , $\mu\text{mol CO}_2$ per $\mu\text{mol photons}$

A.5 Water balance for the Congo Basin (1979-1983)

	Rainfall	Total Evaporation		Runcalc	RunObse	RunModel
	P (mm/day)	E (mm/day)	P-E (mm/day)	(P-E)*Area	m ³ /s	m ³ /s
Jan	4.611392	3.99	0.62	21519.79	48144.80	86513.00
Feb	5.940411	4.13	1.81	62827.81	39028.60	96711.00
Mar	6.503167	4.12	2.38	82717.67	35233.00	104977.33
Apr	5.773436	4.02	1.75	60884.93	36556.00	122418.33
May	3.872537	3.26	0.61	21215.94	37367.00	100090.67
Jun	2.142448	2.37	-0.23	-8043.13	37703.40	96088.67
Jul	1.633598	1.95	-0.31	-10857.95	32625.60	58485.33
Aug	2.602772	2.11	0.50	17225.56	31519.80	14245.33
Sep	4.337423	2.94	1.39	48388.23	36659.80	14136.33
Oct	5.940107	3.68	2.26	78420.56	42202.60	35167.67
Nov	7.093112	3.81	3.28	113897.95	51461.40	67050.00
Dec	4.838945	3.83	1.01	34949.10	55034.40	103573.33
Total				43595.54	40294.70	74954.75

APPENDIX B

PAIRED_SAMPLE STUDENTS-‘t’ DISTRIBUTION

B.1 Tests for differences between control run and experimental cases.

In some cases an observation in the first sample may be related to or correlated with an observation in the second sample. In such case we have what is often called a paired or repeated measures design. A Paired-sample t-test does not have the assumption that the variances of the two populations are equal nor does it have the assumption that the two populations have normal distributions. It does, however, assume that the deviations are distributed normally.

The paired-sample student’s t (distribution) statistical test was performed to determine if the controlled and modified runs had any difference at the 95% significant levels. The null hypothesis in the case of precipitation was that ‘changing vegetation from **control condition** to the corresponding **experimental case** did not alter the mean monthly rainfall values of the Congo Basin’. In other words the difference between the controlled and modified runs is not significantly different from zero.

The differences between the monthly mean rainfall values i.e the 5 year monthly mean (1979-1983) for **Control** and **Experiments** were calculated using the rainfall values averaged over the 5 year period. The degrees of freedom over the 60 months period is 118 i.e. (2n-2). For a 95 % confidence level, the student’s t distribution requires 2.5% in each tail and therefore a test for t less than (-1.97.) or greater than (+1.972) is performed. If the criterion is met then the null hypothesis is rejected and it can be concluded that deforestation is responsible for the change in precipitation at the 95% confidence level.

The statistics t in this paired sample analysis is given by

$$t = \frac{|\bar{x}_1 - \bar{x}_2|}{\sqrt{A/B}}$$

Where,

$$A = (n_1 + n_2) + n_1 n_2,$$

and

$$B = [(n_1 - 1)s_1^2 + (n_2 - 1)s_2^2] + [n_1 + n_2 - 2]$$

\bar{x} is the sample mean and s is the standard deviation. The variables x_i represent the differences between the annual mean rainfall values for the **forested** and the **grassland** type vegetation i.e. the controlled and the high deforestation (experiment 1) model runs. As can be seen from the results in Appendix B the t value for the mean monthly precipitation in the Congo basin is less than 1.97 and so the null hypothesis can not be rejected. It can therefore be asserted with a 95% confidence level that deforestation of the Congo basin would not alter the mean monthly rainfall values.

Table B.1: Monthly precipitation for Congo Basin, 1979-1983 (mm/day)
Control case and High Deforestation (experiment 1)

Month	PPT-cont	PPT-hdef	PFTcont-PFThdef
79-Dec	3.549854	3.073606	0.476248
80-Dec	5.054733	5.138329	-0.083596
81-Dec	5.750053	5.464416	0.285637
82-Dec	3.91652	5.809451	-1.892931
83-Dec	4.785801	5.804989	-1.019188
79-Nov	6.231501	4.974015	1.257486
80-Nov	6.442832	5.6938	0.749032
81-Nov	5.896362	5.22993	0.666432
82-Nov	5.454196	5.357906	0.09629
83-Nov	5.677163	5.787924	-0.110761
79-Oct	6.42568	5.897985	0.527695
80-Oct	6.98841	5.494348	1.494062
81-Oct	6.415299	5.585614	0.829685
82-Oct	6.016798	6.265582	-0.248784
83-Oct	6.669648	6.316416	0.353232
79-Sep	5.8246	5.530192	0.294408
80-Sep	6.627597	5.334905	1.292692
81-Sep	6.528754	5.735069	0.793685
82-Sep	4.831487	5.279219	-0.447732
83-Sep	5.05474	5.688799	-0.634059
79-Aug	3.600657	3.514656	0.086001
80-Aug	4.438614	2.905229	1.533385
81-Aug	4.498918	3.560425	0.938493
82-Aug	2.701985	3.348333	-0.646348
83-Aug	4.122511	3.704204	0.418307
79-Jul	2.110526	2.027358	0.083168
80-Jul	2.595943	2.366086	0.229857
81-Jul	2.680394	2.253985	0.426409
82-Jul	1.824989	1.424279	0.40071
83-Jul	1.500386	1.716436	-0.21605
79-Jun	1.595151	1.628778	-0.033627
80-Jun	2.163621	0.950632	1.212989
81-Jun	1.907408	1.64223	0.265178
82-Jun	1.042209	1.333778	-0.291569
83-Jun	1.459603	1.852228	-0.392625
79-May	3.308749	2.73124	0.577509
80-May	3.908096	1.873522	2.034574
81-May	2.480826	2.63519	-0.154364
82-May	1.421229	1.718027	-0.296798
83-May	1.894963	2.70662	-0.811657
79-Apr	4.983376	4.795028	0.188348
80-Apr	5.04592	4.220858	0.825062
81-Apr	4.473847	3.844444	0.629403

Table B.1 (continued)

82-Apr	3.898447	4.180587	-0.28214
83-Apr	3.285527	3.668532	-0.383005
79-Mar	6.332173	5.744278	0.587895
80-Mar	6.260902	5.878464	0.382438
81-Mar	6.161588	5.005411	1.156177
82-Mar	5.662103	5.39544	0.266663
83-Mar	5.28377	5.883058	-0.599288
79-Feb	7.261634	5.535319	1.726315
80-Feb	7.721837	6.581322	1.140515
81-Feb	7.920043	6.107476	1.812567
82_feb	6.206263	5.288535	0.917728
83-Feb	6.355781	6.283669	0.072112
79-Jan	6.107402	5.662485	0.444917
80-Jan	6.095126	4.935369	1.159757
81-Jan	1.719261	5.239354	-3.520093
82-Jan	5.026718	4.322376	0.704342
83-Jan	5.246221	5.414448	-0.168227
average	4.60744575	4.322369733	0.285076017
Std	1.864642477	1.63464066	

$$t = 0.285 / (0.0333 * 3.072) ** 0.5 = 0.16$$

Table B.2 Atmospheric input to land model

¹ Reference height	z_{atm}	m
Zonal wind at z_{atm}	u_{atm}	m s^{-1}
Meridional wind at z_{atm}	v_{atm}	m s^{-1}
Potential temperature	$\overline{\theta}_{atm}$	K
Specific humidity at z_{atm}	q_{atm}	kg kg^{-1}
Pressure at z_{atm}	P_{atm}	Pa
Temperature at z_{atm}	T_{atm}	K
Incident longwave radiation	$L_{atm} \downarrow$	W m^{-2}
² Liquid precipitation	q_{rain}	mm s^{-1}
² Solid precipitation	q_{sno}	mm s^{-1}
Incident direct beam visible solar radiation	$S_{atm} \downarrow_{vis}^{\mu}$	W m^{-2}
Incident direct beam near-infrared solar radiation	$S_{atm} \downarrow_{nir}^{\mu}$	W m^{-2}
Incident diffuse visible solar radiation	$S_{atm} \downarrow_{vis}$	W m^{-2}
Incident diffuse near-infrared solar radiation	$S_{atm} \downarrow_{nir}$	W m^{-2}

¹The reference heights for temperature, wind, and specific humidity ($z_{atm,h}$, $z_{atm,m}$, $z_{atm,w}$) are required. These are set equal to z_{atm} .

²The atmosphere provides convective and large-scale liquid and solid precipitation, which are added to yield total liquid precipitation q_{rain} and solid precipitation q_{sno} .

Table B.3 Land model output to atmospheric model

¹ Latent heat flux	$\lambda_{vap}E_v + \lambda E_g$	W m^{-2}
Sensible heat flux	$H_v + H_g$	W m^{-2}
Water vapor flux	$E_v + E_g$	mm s^{-1}
Zonal momentum flux	τ_x	$\text{kg m}^{-1} \text{s}^{-2}$
Meridional momentum flux	τ_y	$\text{kg m}^{-1} \text{s}^{-2}$
Emitted longwave radiation	$L \uparrow$	W m^{-2}
Direct beam visible albedo	$I \uparrow_{vis}^{\mu}$	-
Direct beam near-infrared albedo	$I \uparrow_{nir}^{\mu}$	-
Diffuse visible albedo	$I \uparrow_{vis}$	-
Diffuse near-infrared albedo	$I \uparrow_{nir}$	-
Absorbed solar radiation	\bar{S}	W m^{-2}
Radiative temperature	T_{rad}	K
Temperature at 2 meter height	T_{2m}	K
Specific humidity at 2 meter height	q_{2m}	kg kg^{-1}
Snow water equivalent	W_{sno}	m

Table B.4 Model and empirical saturated hydraulic conductivity values

	Ks(z) = Koexp(-fz) (mm/hr)	Ks(z)= 0.0070556*10^{-0.884+0.0153(%sand)} (mm/hr)
0	18.57	18.57
0.5	6.83	17.74
1	2.5	16.77
1.5	0.92	16.31
2	0.34	15.69
2.5	0.12	15.97
3	0.05	15.8

$f = 2 \text{ m}^{-1}$

$k_0 = 0.0070556 * 10^{-0.884 + 0.0153\% \text{ sand}} \text{ (mms}^{-1}\text{)}$

REFERENCES

- Berger, A. L., Long-term variations of daily insolation and quaternary climatic changes, *J. Atmos. Sci.*, 35, 2362–2367, 1978.
- Bonan, G.B., Oleson, K.W., Vertenstein, M., Levis, S., Zeng, X., Dai, Y., Dickinson, R.E., and Yang, Z.-L. 2002a. The land surface climatology of the Community Land Model coupled to the NCAR Community Climate Model. *J. Climate* 15: 3123-3149.
- Bonan, G.B., Levis, S., Kergoat, L., and Oleson, K.W. 2002b. Landscapes as patches of plant functional types: An integrating concept for climate and ecosystem models. *Global Biogeochem. Cycles* 16: 5.1-5.23.
- Charney, J.G., 1975: Dynamics of deserts and drought in Sahel. *Quart. J. Royal Meteor.*
- Dickinson, R.E., Henderson-Sellers, A., Kennedy, P. J. and Wilson, M.F., 1986: Biosphere-Atmosphere transfer scheme (BATS) for the NCAR Community Climate Model. National Center for Atmospheric Research, Boulder, CO. Tech
- Eltahir, E.A.B., Gong, C. (1996): Dynamics of Wet and Dry Years in West Africa. *Journal of Climate*, 9(5): 1030-1042
- Findell, Kirsten L., Thomas R. Knutson (2005): Weak Simulated Responses to Complete Tropical Deforestation. *Journal of Climate* (submitted)
- Gates, W. L., et al., An overview of the results of the atmospheric model intercomparison project (AMIP I), *Bull. Am. Meteorol. Soc.*, 81, 29– 55, 1999.
- Hack, J. J., J. T. Kiehl, and J. W. Hurrell, The hydrologic and thermodynamic characteristics of the NCAR CCM3, *J. Clim.*, 11, 1179 – 1206, 1998.
- Henderson-Sellers, A., and V. Gornitz, 1984: Possible climatic impacts of land cover

- transformations, with particular emphasis on tropical deforestation, *Clim. Change*, 6, 231-258.
- Irizarry-Ortiz, Wang, Eltahir E.A.B., (2003): Role of the biosphere in the mid-Holocene Climate of West Africa. Note/TN-275+STR, *JOURNAL OF GEOPHYSICAL RESEARCH*, VOL. 108, NO. D2, 4042, doi: 10.1029/2001JD000989
- Kinter, J. L., Shukla, J., Marx, L. and E. K. Schneider, E.K., 1988: A simulation of the winter and summer circulations with the NMC global spectral model, *J. atmos. Sci.*, 45, 2486-2522,
- Lal, R. 1995: Soil resources for plantation forestry and their Characteristics. In : Management of Soil, Nutrients, and water in Tropical Plantation Forests, E.K.S Nambiar & A.G Brown (Eds.), ACIAR, Canberra, and CIFOR, Bogor (in press).
- Lanly, J.P., Singh, K.D. and Janz, K. 1991: FAO's 1990 reassessment of tropical forest cover. *Nature & Resources*, 27, 21-26. *Soc*, 101, 193-202.
- Lean, J., and D.A. Warrilow, 1989: Simulation of the regional climatic impact of Amazon deforestation, *Nature*, 342, 411-413.
- Maynard, K., Royer, J.-F., (2004): Effects of realistic land-cover change on greenhouse-warmed African climate, *Climate Dynamics*(2004) 22:343-358
- NCAR/TN-461+STR NCAR TECHNICAL NOTE May 2004: Technical description of the Community Land Model (CLM)
- Nobre, C. A., P. J. Sellers, and J. Shukla, 1991: Amazonian deforestation and regional climate change, *J. Clim.*, 4, 957-988.
- Nicholson, E. S., Kim, J., (1997): The Relationship of the El Nino-Southern Oscillation to African Rainfall, *International Journal of Climatology*, Vol. 17, 117-135 (1997)
- Osborne, T.M., Lawrence, D.M., Slingo, J.M., Challinor, A.J., Wheeler, T.R., (2004): Influence of vegetation on the local climate and hydrology in the tropics: sensitivity to soil parameters. *Climate Dynamics* (2004) 23: 45-61
- Pan, F., Erickson, D. J., Branstetter, M., King, A.W., Oglesby, R.J., Wolinsky, M. and Sale, M.J.: The effect of soil conductivity on the hydrological cycle and surface

- energy budget in the CCSM2: The impact of the implementation of a TOPMODEL approach in global GCM. June 2005 (to be submitted to Journal of Geophysical Research-Atmospheres)
- Peixoto, J., Oort, H.A., 1992; Physics of Climate, pg 290/291
- Ramanathan, V., and P. Downey, A nonisothermal emissivity and absorptivity formulation for water vapor, J. Geophys. Res., 91, 8649–8666, 1986.
- Rasch, P. J., and J. E. Kristjansson; A comparison of the CCM3 model climate using diagnosed and predicted condensate parameterizations, J. Climate, 11, 1587—1614, 1998.
- Sato, N., P. Sellers, D. Randall, E. Schneider, J. Shukla, J. Kinter, Y-T Hou, and E. Albertazzi 1989: Effects of implementing the simple biosphere model in general circulation model, J. atmos. Sci., 46, 2757-2782.
- Sela, J.G. 1980: Spectral modeling at the N.M.C., Mon. Weather Rev., 108, 1279-1292.
- Shukla, J., Nobre, C. Sellers, P. 1990: Amazon Deforestation and Climate Change, Science, Vol. 247. March 16. pp 1322-1325
- Slingo, J. M., The development and verification of a cloud prediction scheme for the ECMWF model, Q. J. R. Meteorol. Soc., 113, 899–927, 1987.
- Slingo, J., 2003: ENSO-Monsoon Interaction. Monsoon Overview. Encyclopedia of Atmospheric Sciences. pp.1365 – **1370**.
- Sudd, Y., Walker, K., Kim, J.H., Liston G., Sellers, P., Lau, K.M., (1996): Biogeophysical effects of a tropical deforestation scenario: A GCM simulation study. J. Climate, 9. 3225-3247.
- Sundqvist, H., Parameterization of condensation and associated clouds in models for Weather prediction and general circulation simulation, in Physically-based

- Modeling and Simulation of Climate and Climate Change, Vol. 1, edited by M. E. Schlesinger, 433–461, Kluwer Academic, 1988.
- Vig, J. N., Kraft, M.E., 2003: Environmental Policy, New Directions for the 21st Century
- Wu, W., Dickinson, R.E., 2004: Time Scales of Layered Soil Moisture Memory in the Context of Land-Atmosphere Interaction. *Journal of Climate*, Vol. 17, pp 2572-2764.
- Webster, P.J., Fasullo, J., 2003: Monsoon: Dynamical Theory. *Encyclopedia of Atmospheric Sciences*. Eds. J. Holton and J.A. Curry. Academic Press, 1370-1385
- Zeng, N., Dickinson, R., Zeng, X., (1996) Climatic impacts of Amazon deforestation a mechanistic model study. *J. Clim* 9: 859-883
- Zhang, G. J., and N. A. McFarlane, Sensitivity of climate simulations to the parameterization of cumulus convection in the Canadian Climate Centre general circulation model, *Atmosphere-Ocean*, 33, 407–446, 1995.
- Zhang H, McGuffie, K., Henderson-Sellers, A. (1996): Impacts of tropical deforestation. Part II: the role of large scale dynamics *J Clim* 10: 2498-2521
- Zhang, M., W. Lin, C. S. Bretherton, J. J. Hack, and P. J. Rasch, (2003): A modified formulation of fractional stratiform condensation rate in the NCAR community atmospheric model CAM2, *J. Geophys. Res.*, 108 (D1), 2003.
- Zeng, X., Eltahir E (1998): The role of vegetation in the dynamics of West African monsoons. *J. clim.* 11:2078-2096
- Zeng, X. (2001): Global vegetation root distribution for land modeling. *J. Hydrometeor.* 2:525-530.

Willis Otieno Shem was born in Kisumu, Kenya in September 1958. He received his primary education at Karanda Primary school, his secondary education at the Rift Valley Technical School and then proceeded to Mombasa Polytechnic for his East African Advanced Certificate of Education. He obtained his Bsc (meteorology, major) at the University of Nairobi in 1983. He then worked in the Ministry of Water Resources Management for ten years before proceeding for his M.Eng.(Water Resources Technology) from Vrije Universiteit Brussels (VUB), Belgium.

He began his graduate studies at the Georgia Institute of Technology in 2001 under the advisement of Professor Robert Dickinson. He received his Ms in Earth and Atmospheric Sciences in 2003 and proceeded for his PhD. research work on the topic 'Biosphere-Atmosphere Interaction in the Congo Basin and its Influence in the Regional Hydrological Cycle'. Shem has made several oral and poster presentations in professional meetings including the American Meteorological society conferences. He has two children, Esther and Victor